Hybrid Wakefield Acceleration

A Source of Stable and High-Density Electron Beams

F. Moritz Foerster

München 2024

Hybrid Wakefield Acceleration

A Source of Stable and High-Density Electron Beams

F. Moritz Foerster

Dissertation
der Fakultät für Physik
der Ludwig-Maximilians-Universität
München

vorgelegt von
F. Moritz Foerster
aus Frankenberg (Eder)

München, den 16.07.2024

Erstgutachter: Prof. Dr. Stefan Karsch
Zweitgutachter: Prof. Dr. Ulrich Schramm
Tag der mündlichen Prüfung: 17.10.2024

Zusammenfassung

Teilchenbeschleuniger haben entscheidend zum besseren Verständnis der Physik beigetragen und zahlreiche technologische Entwicklungen mit Anwendungen in Wissenschaft, Medizin und Industrie ermöglicht. Allerdings bieten konventionelle Beschleuniger, wie die weit verbreiteten Hochfrequenzbeschleuniger, auf Grund von Vakuumdurchschlägen nur begrenzte Beschleunigungsgradienten und sind somit groß und daher teuer. Plasmabasierte Beschleuniger, als möglicher zukünftiger Ersatz, bieten etwa 1000-mal höhere Beschleunigungsgradienten und eine entsprechend kompaktere Bauform. In den letzten Jahrzehnten wurden dabei enorme Fortschritte, wie die Beschleunigung um mehrere Gigaelektronenvolt und von Ladungen im Nanocoulomb-Bereich, erzielt. Insbesondere die teilchenstrahlgetriebene Wakefield-Beschleunigung (PWFA) gilt als Alternative für konventionelle Beschleuniger, da bereits hoher Energiegewinn in einer einzelnen Beschleunigerstufe und eine hohe Qualität der Elektronenpakete demonstriert werden konnten. Außerdem ist die Wakefield-Erzeugung bei PWFA unabhängig von der Energie des relativistischen Treibers und damit intrinsisch sehr stabil. Allerdings nutzten bisherige Experimente konventionelle Beschleuniger zur Treiberstrahlerzeugung und sind selten, da sie hohe Treiberströme (kilo-Ampere) erfordern. Demgegenüber wurden zuletzt viele Experimente zur lasergetriebenen Wakefield-Beschleunigung (LWFA) in Universitätslaboren durchgeführt. Typische von Kurzpulslasern angetriebene LWFAs sind kompakte Maschinen und erzeugen ultrakurze (wenige fs), ladungsreiche (bis zu nC) Elektronenstrahlen mit hohem Strom (einige 10 kA). LWFAs weisen jedoch häufig nur eine begrenzte Stabilität und Kontrolle der Strahlqualität auf, da diese stark von Fluktuationen des Lasertreibers abhängen.

Diese Arbeit behandelt einen hybriden Ansatz (L-PWFA), der die beiden komplementären Plasmabeschleunigertypen kombiniert. Ein LWFA liefert den Treiber für einen nachfolgenden PWFA. Im PWFA werden sogenannte Witness-Pulse intern injiziert und beschleunigt. Die Injektion erfolgt an einem optisch erzeugten Dichteshock. Dieser neue Ansatz entkoppelt die Eigenschaften des Injektors und des Beschleunigers (des Gastargets), was eine unabhängige Kontrolle der verschiedenen Schockparameter ermöglicht und zur höheren Stabilität der Witness-Pulse beiträgt.

Der hybride L-PWFA erreicht eine ähnliche Energiestabilität wie der antreibende LWFA selbst und wie von einem Hochfrequenzbeschleuniger getriebene PWFAs. Simulationen zeigen eine zusätzliche Energiestabilisierung durch einen Effekt namens Beam Loading, sodass bei korrekt eingestellter injizierter Ladung, die Witnessenergie wesentlich stabiler sein kann als die des Treibers. Die PWFA liefert hohe Beschleunigungsgradienten von über 150 GeV/m, eine effektive Abbremsung des Treibers und eine hohe Energieübertragungseffizienz auf den Witness von 10%. Die Energiebandbreite und Divergenz der Witness-Pulse aus der hybriden L-PWFA sind kleiner, und die räumlich-spektrale Teilchendichte daher höher als die der LWFA-generierten Elektronen, die als Treiber dienen, was einen Nettomehrwert für Anwendungen bedeutet.

Somit verbindet der hybride Ansatz die Stabilität und Strahldichte von PWFA mit der hohen Verfügbarkeit der Treiberstrahlen aus LWFA. Dabei sind die gezeigte Stabilität und Ladungsdichte Grundvoraussetzungen für die Erzeugung brillanter Röntgenstrahlung, und für neue Anwendungen, die auf solchen Quellen basieren.

Abstract

Particle accelerators have significantly advanced our understanding of fundamental physics and have enabled far-reaching technological developments in science, medicine, and industry. However, conventional accelerators, such as the widely used radio frequency accelerators, offer limited acceleration gradients due to vacuum breakdown and are generally large and expensive. Plasma-based accelerators, as their possible future replacement, promise about 1000 times higher acceleration gradients and, consequently, a smaller footprint.

Enormous progress in plasma-based acceleration has been made in recent decades, including the acceleration of nanocoulombs of charge and energy gains of several gigaelectronvolts. In particular, particle beam-driven plasma wakefield acceleration (PWFA) is considered a promising successor to conventional accelerators, as high energy gain in a single stage and high quality of the electron bunches have been demonstrated. Furthermore, the wakefield excitation in PWFA is intrinsically very stable towards fluctuations of the driver, as it does not depend on the energy of the relativistic drive beam. So far, these experiments still need large-scale radio frequency machines to generate the driver and are very rare, as PWFA requires multi-kiloampere drive bunches. In contrast, many laser wakefield acceleration (LWFA) experiments have been carried out in university-scale labs worldwide in recent years. Typical LWFAs driven by short-pulse lasers are compact machines and produce ultra-short (few fs), high charge (up to nC), and therefore high-current (10s of kA) electron bunches. Yet, LWFA experiments often suffer from limited stability and control of beam quality due to their sensitive dependence on fluctuations of the laser driver.

This work presents a hybrid approach (L-PWFA) combining the two complementary plasma accelerators. An LWFA delivers the drive beam for a subsequent PWFA a few millimeters downstream. In the PWFA stage, so-called witness bunches are internally injected and accelerated. The injection happens in the down ramp of an optically-generated density shock. This new approach decouples the properties of the injector and the accelerator (the gas target), allowing independent control over the different shock parameters and contributing to higher stability of the witness beam energy.

In this experimental setup, the hybrid L-PWFA achieves similar energy stability to the driving LWFA alone and to recently reported radio frequency accelerator-driven PWFAs. Supporting simulations show additional energy stabilization through an effect called beam loading so that when the injected charge is set correctly, the witness energy can be much more stable than the driver energy. The PWFA delivers high acceleration gradients in excess of 150 GeV/m, effective driver deceleration, and a high energy transfer efficiency to the witness of 10%. In the experiment, the energy spread and divergence of the witness beams from the hybrid L-PWFA are smaller, and therefore, the spatio-spectral particle density is higher than that of the original LWFA-generated electrons serving as a driver, thus achieving a net added value for applications.

In conclusion, the hybrid approach combines the promise of stability and beam density of PWFA and the high availability of LWFA-generated drive beams. The presented stability and charge density of the electron bunches are prerequisites for generating brilliant X-rays, and push forward novel applications based on such sources.

Contents

List of Figures

List of Tables

List of Abbreviations and Symbols

This list defines abbreviations and symbols that are used in the body of the document. Further, context-specific abbreviations are defined in the respective sections.

ϵ_0	Vacuum permittivity	8.854×10^{-12} As/Vm
ω_p	Plasma frequency	$\sqrt{\frac{n_e e^2}{\epsilon_0 m_e}}$ [rad/s]
σ_θ	RMS beam divergence	
σ_r	RMS beam radius	
e	Elementary charge. (Note that in this work the negative sign of the electron charge is omitted from visual representations for readability.)	1.602×10^{-19} C
k_b	Boltzmann constant	1.381×10^{-23} J/K
m_e	Electron rest mass	9.109×10^{-31} kg
n_e	Electron plasma density	
c	Speed of light in a vacuum	2.998×10^{8} m/s
ASE	Amplified Spontaneous Emission	
ATLAS	Advanced Titanium Sapphire Laser System	
BSI	Barrier Suppression Ionization	
CAD	Computer-Aided Design	
CALA	Center for Advanced Laser Application	
CPA	Chirped Pulse Amplification	
CTR	Coherent Transition Radiation	
DM	Deformable Mirror	
ETTF	Electron and Thomson Test Facility	
FBPIC	Fourier-Bessel Particle-In-Cell	
FEL	Free Electron Laser	
FROG	Frequency-Resolved Optical Gating	
FWHM	Full Width at Half Maximum	
HDR	High Dynamic Range	

L-PWFA	Hybrid LWFA-PWFA
LWFA	Laser Wakefield Acceleration
Nd:YAG	Neodymium-doped Yttrium Aluminum Garnet
PIC	Particle-In-Cell
PWFA	(Particle-driven) Plasma Wakefield Acceleration
RF	Radio Frequency
RMS	Root Mean Square
SD	Standard Deviation
SRSI	Self-Referenced Spectral Interference
STC	Spatio-Temporal Coupling
Ti:Sa	Titanium-Sapphire

I Introduction

TAKE-HOME MESSAGE

This dissertation presents experimental and simulation results on developing a particle-driven plasma wakefield accelerator. The high-current electron bunches from a laser wakefield accelerator act as its energy source. This work elaborates on the advantages of plasma-based accelerators that go beyond their compactness. In particular, improvements in beam quality regarding stability and beam density are presented. Through these advances, this work significantly contributes to the expansive field of development and application of plasma-based particle accelerators.

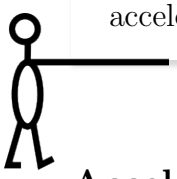

Accelerators in a nutshell

Figure I.1: ***A simple particle accelerator: A capacitor pulled by a race car.*** *Electrons acquire kinetic energy by falling along the electric field lines in a capacitor. Their final energy is proportional to the field amplitude and the spacing of the plates. If the capacitor co-moves at the velocity of the electrons, the possible energy gain is limited only by the energy the car supplies to the system. Drawing inspired by [1, 2].*

The idea of any particle accelerator is to expose a bunch of charged particles to a directed (longitudinal) field. Particles gain energy while "falling" along the field lines of the electric field. The final particle energy depends on the length of the interaction and the field strength during the interaction. A simple implementation of such an accelerator would be a capacitor pulled by a race car (see Figure I.1). When at rest, the final electron energy is proportional to the field amplitude inside the capacitor and the spacing of the plates. If the race car (driver), and thus the capacitor (the field), co-moves at the phase velocity of the electrons, the possible energy gain is limited only by the energy the car can deliver to the system, i.e. when it runs out of fuel. The consequences of this analogy will be discussed in more detail later. Over the last century, many types of accelerators have been developed and successfully constructed.

Why should we develop new accelerator concepts?

Particle accelerators are pivotal in advancing particle physics, enabling studies into the fundamental properties of matter through ever-increasing particle energies. They

also enable the generation of high-brilliance radiation like synchrotron light and free electron lasers, significantly impacting physics, chemistry, biology, and beyond. In medicine, accelerators are vital for producing medical isotopes, hadron therapy, and X-ray imaging, and have an immediately recognizable societal impact. Industrially, they are crucial in the semiconductor sector for tasks such as ion implantation, surface modifications, and non-destructive material testing.

Irrespective of their wide-ranging applications and success in fostering scientific advancements – including earning Nobel Prizes [3] – the construction, and operation of high-energy, high-quality accelerators are costly due to their complexity and size, leading to their limited availability. This scarcity underscores the importance of exploring innovative accelerator concepts.

A short history of accelerators

The concept of particle acceleration is not new, as natural astrophysical accelerators have been generating particle energies of up to 10^{20} eV [4] for billions of years. However, human-made accelerators only emerged in the late 19th century, marked notably by the invention of Braun's cathode ray tube in 1897, which coincided with the discovery of electrons by J.J. Thomson.

Early accelerators were electrostatic, where the final energy equaled the maximum generated voltage. The first major step was the introduction of alternating field accelerators, in which the same voltage drop is generated by an alternating field and can be used several times using appropriate beam guidance systems. Key advancements include the cyclotron in the 1930s [5], which accelerates charged particles along a spiral trajectory using a constant magnetic field to bend their path and a correctly phased alternating electric field between two electrodes to boost the electron energy with each pass. Around the same time, the Betatron took a different approach, applying a changing magnetic field to accelerate electrons on a circular orbit through electromagnetic induction, similar to a transformer [6, 7]. In the 1940s and 50s, the Synchrotron was designed to handle the relativistic mass increase of particles [8]. It utilized variable-frequency alternating electric fields and adjustable magnetic fields to keep the accelerating particles on a circular orbit. This technology allowed much higher energy levels and laid the foundation for large-scale accelerators for high-energy physics and synchrotron light sources for diverse applications. Linear accelerators (LINACs) advanced the field by enabling high-energy acceleration of light particles (electrons and positrons) along a straight path, avoiding excessive energy losses via synchrotron radiation. In LINACs, a traveling radio-frequency wave is applied within a metallic waveguide structure, with the frequency and cavity dimensions tailored to keep particle bunches in the accelerating phase of the traveling field.

Due to their immense scale and cost, existing facilities, like the 27 km circumference Large Hadron Collider or multi-kilometer electron LINACs, are already close to what is feasible to build. Plans for building machines such as the International Linear Collider (ILC) or the Compact Linear Collider (CLIC) tend to be postponed [9], underlining the limitations of current technologies and highlighting the need for innovative approaches that could lead to more compact and cost-effective solutions.

Plasma-based acceleration

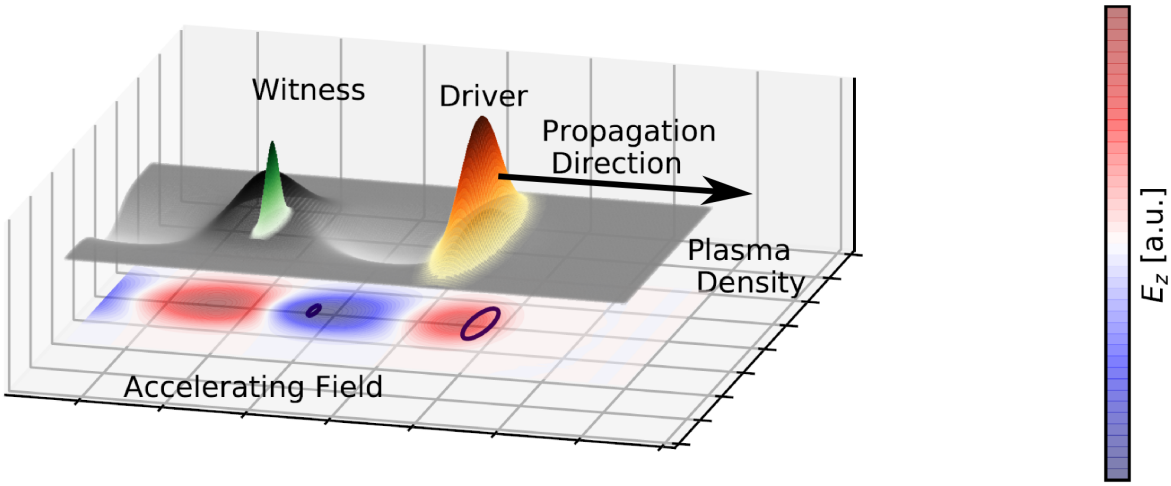

Figure I.2: ***Schematic drawing of a wakefield accelerator.*** *A driver (shown here in brown, previously represented by the race car) perturbs an initially homogeneous plasma (gray-sale). The electron density is reduced in the region just after the driver. On the timescale of the wake excitation, the ions stay stationary. The resulting charge separation fields set up a plasma wave trailing the driver (previously represented by the plate capacitor). A bunch of witness electrons (green) positioned at the right phase behind the driver gains energy. The longitudinal component of the wakefield is plotted on the lower face of the 3D plot.*

Plasma-based accelerators can overcome some of the limitations of conventional accelerators. In plasma-based accelerators, the accelerating structure is a wakefield, i.e., a plasma density perturbation (plotted in gray-scale in Figure I.2). This structure can not break down through ionization as plasma is already an ionized state of matter. Therefore, much larger accelerating fields can be supported and the overall length of the accelerator shrinks accordingly. At plasma densities around $1 \times 10^{18}\,\mathrm{cm}^{-3}$ gradients of about $100\,\mathrm{GV/m}$ are obtained, about three to four orders of magnitude higher than in rf-accelerators.

Intense laser pulses and high-current charged particle beams can drive strong wakefields in high-density plasmas. These drivers (plotted in brown in Figure I.2) perturb the plasma density distribution by their ponderomotive or Coulomb force, respectively. After the perturbation, the displaced electrons are attracted back by the static ions' electric field and oscillate around their initial position. As the driver propagates through the plasma close to the speed of light, the driver sets up a co-moving charge separation field, called the wakefield. In the correct phase behind the driver, the wakefield accelerates electrons in a forward direction. As a relativistic electron travels near the speed of light, it can stay in phase with the wakefield over an extended period and gain substantial energy.

While the first wakefield experiments used particle drivers at national accelerator labs, laser-driven wakefields have dominated the field over the last two decades. Today, sufficiently strong drive lasers are widely available, even in university-scale labs, due to the progress in laser technology over the last decades.

Laser Wakefield Acceleration (LWFA)

The idea for LWFA dates back to the seminal paper by Tajima and Dawson in 1979 when no suitable drive lasers were available [10]. A key development in LWFA was the invention of Chirped Pulse Amplification (CPA) in 1985 [11]. One of the first breakthroughs using such lasers was the electron acceleration in the self-modulated wakefield regime in the 90s [12]. In this regime, the laser pulse is longer than the plasma wavelength and is modulated during the interaction with the plasma via the Raman forward-scattering instability. With the ongoing development of Titan:Sapphire (Ti:Sa) laser systems, high-power lasers with short pulse length became available. At plasma densities on the order of $10^{18}\,\mathrm{cm}^{-3}$, the pulse length of modern Ti:Sa short pulse lasers ($\sim 30\,\mathrm{fs}$) is smaller than the plasma wavelength. This development enabled a transition to the bubble or blowout regime [13–17]. As Ti:Sa lasers became available in many university-scale labs, the number of reported experiments increased tremendously.

For the last 20 years, the optimization of LWFA-generated electron beams has continued. The beams produced have become progressively more energetic, with lower energy spread and higher reproducibility. Introducing different mechanisms for controlled injection was crucial for optimizing beam parameters [18–24]. The common characteristics of beams from LWFA are Femtosecond pulse duration [25, 26] and Micrometer source size [27, 28]. With increasing laser power, some of the experiments produced bunch charges of more than one Nanocoulomb [29], leading to multi 10 kA peak currents. On the energy frontier, guiding of the laser pulses was used to reach ever-higher electron energies of up to 8 GeV [30].

Particle-driven Plasma Wakefield Acceleration (PWFA)

Even before the first LWFA experiments, particle beam-driven plasma accelerators were demonstrated. Tracing back to an idea proposed by Chen et al. in 1985, one relativistic and high-current electron bunch sets up a plasma wave, while a second one at the appropriate phase behind the driver absorbs the energy from the wakefield [31]. The first successful PWFA experiments, reported at Argonne in the 1980s [32], used linac-generated drive beams several millimeters long with low currents ($\sim 100\,\mathrm{A}$) and plasma densities around $10^{13}\,\mathrm{cm}^{-3}$, yielding acceleration gradients of $\sim 1\,\mathrm{MV/m}$. Experiments followed using the 50 fs-long, 42 GeV electron beam from SLAC as a driver for PWFA. At a plasma density of $2.7\times10^{17}\,\mathrm{cm}^{-3}$ and a measured acceleration gradient of 52 GV/m, they doubled the energy of some electrons in the tail of the drive beam [33]. The Facility for Advanced Accelerator Experimental Tests (FACET and FACET-II) was recently created at SLAC to investigate different aspects of electron and positron beam-driven wakefields [34, 35]. Similar research has also been carried out at DESY in Hamburg in the framework of Flash Forward [36]. Recently, the AWAKE project successfully accelerated electrons using a long but highly energetic proton beam as a driver [37]. Since the 200 ps (6 cm) long drive beam is much longer than the plasma wavelength ($\sim 1\,\mathrm{mm}$ at $n_e \sim 1\times10^{15}\,\mathrm{cm}^{-3}$), this experiment relies on self-modulation of the driver, similar to the early LWFA experiments with ps-long lasers.

Limitations of plasma-based accelerators

Plasma-based accelerators can be much more compact than their conventional counterparts and, therefore, potentially cheaper. However, the provision of the drivers is the main cost point. For LWFA, the costs arise from installing and operating high-power laser systems. These lasers have limited efficiency so far, and the future success of LWFA will depend on their further development. For PWFA even larger facilities were needed for past experiments, as they used drive beams from conventional accelerators with the disadvantages discussed above.

Additional drawbacks of plasma-based accelerators are their limited stability and beam quality. Stability problems arise because a new accelerator is created on every shot. Its properties sensitively depend on the drive beam properties. In the case of a laser driver, shot-to-shot fluctuations of state-of-the-art lasers in terms of energy, spectrum, pulse length, and spatial wavefront already have huge effects on the generated electron beams [38].

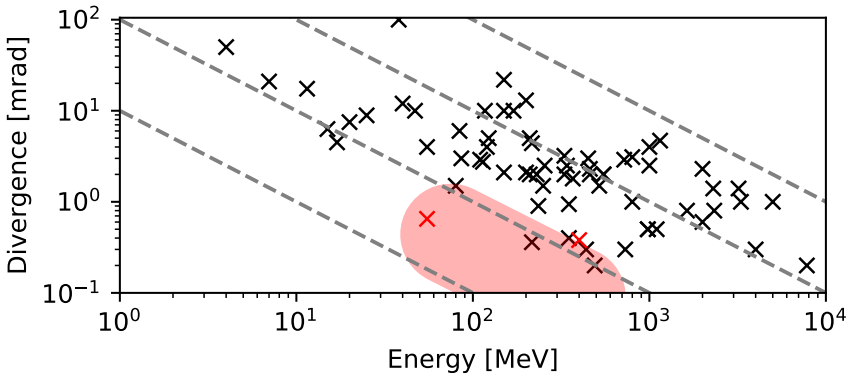

Figure I.3: ***Divergence of electron beams from plasma accelerators.*** *The plot relates the divergence and energy reported from a large number of LWFA experiments (black crosses) and PWFA experiments with internal injection (red crosses). The data clusters around lines of constant transverse momentum (gray dashed). This work aims to explore the red-shaded part of the parameter space.*

The beam quality of an accelerator is ultimately limited by the injection of the electron bunch into the accelerating structure. Figure I.3 shows the measured divergence reported for a large number of LWFA experiments. These experiments are grouped around lines with constant transverse momentum (the beam divergence naturally decreases with increasing energy, since it is given by the ratio of transverse and longitudinal momentum). This accumulation indicates that in the presence of a relativistic laser driver, there is a lower limit for the transverse momentum and, therefore, an upper limit for the achievable beam quality. This work aims to explore the red-shaded parameter space in Figure I.3 by internally injecting high-quality electron bunches into a PWFA driven by an LWFA.

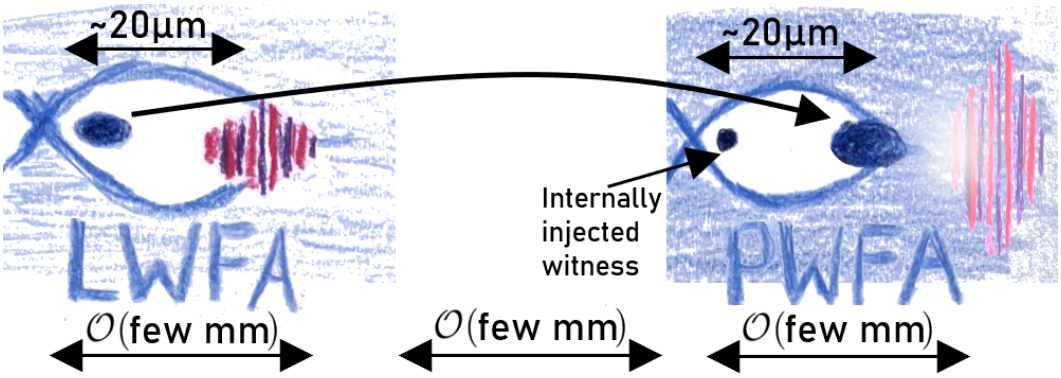

Figure I.4: ***Schematic of a hybrid L-PWFA.*** *An LWFA stage produces the high-current electron bunch that serves as the driver for a subsequent PWFA stage. A witness bunch is internally injected and accelerated in the PWFA stage.*

Hybrid: Combining LWFA and PWFA

Combining an LWFA and a PWFA can tackle some of the individual problems of the two classes of accelerators. LWFAs are widely available these days. LWFA-generated beams from 100TW-class lasers can have sufficiently high currents to drive strong wakefields themselves. Figure I.4 schematically shows a typical hybrid LWFA-PWFA (L-PWFA) experiment: After generating a high-charge electron bunch in the LWFA stage, the spent drive laser and the electrons transverse a vacuum gap of a few mm. The laser further diffracts and will only be able to drive a weak density perturbation in the subsequent PWFA. The strong wakefield is excited by the LWFA-generated electron bunch due to its much smaller divergence. Subsequently, a witness bunch is injected using a suitable method and be accelerated in the wake of the drive bunch. In contrast to the previously mentioned PWFA experiments with conventional accelerators, a hybrid L-PWFA can work at much higher plasma densities far in excess of $1 \times 10^{18}\,\mathrm{cm}^{-3}$, as the LWFA-generated electron bunches are typically much shorter (fs) and denser than their conventionally accelerated counterparts.

State of the art in Hybrid acceleration

The concept of a hybrid L-PWFA arose from observing that in LWFA experiments, electron bunches can drive the wakefield when the laser becomes too weak due to diffraction or depletion. Corde et al. [39] and Heigoldt et al. [25] measured this gradual transition independently using distinct diagnostics. To better control the transition, separate LWFA and PWFA stages can be created using two targets. In early double jet experiments, Chou et al. demonstrated collective deceleration of LWFA-generated electrons in a subsequent plasma target [40]. They identified the similarity of this process with PWFAs driven by conventional accelerators. Based on the scaling laws of plasma wakefield generation with plasma wavelength, they proposed using hybrid L-PWFA as a miniature model of much rarer, large-scale PWFAs.

More systematic studies of high charge beams from LWFA followed over the next years [29, 41]. High charge bunches from LWFA, as described in Götzfried et al.,

modify the acceleration in LWFA via beam loading and are, in the absence of the laser, able to drive strong wakefields themselves. These particle beam-driven wakefields were first directly observed and described by Gilljohann et al. [42]. At the same time, the acceleration of witness electrons in the wake of an LWFA-generated driver was studied. Kurz et al. described the generation of a driver/witness pair in LWFA and the subsequent energy transfer from the driver to the witness in a PWFA stage [43]. Couperus et al. first reported on internal injection at a down ramp in the PWFA stage [44]. In their study, the witness beam was injected at a wire-generated density perturbation in a supersonic gas flow. The final energy of the witness beams could be adjusted utilizing the injection position and the plasma density in the PWFA.

The experimental work on hybrid L-PWFA was supplemented by theoretical studies. Based on simulations, Hidding et al. [45], and Martinez de la Ossa et al. [46, 47] suggested different new injection schemes, promising unprecedentedly low emittance electron bunches. Furthermore, the idea of PWFA as an afterburner for increasing the electron energy beyond the level achievable in pure LWFA was developed [48].

A Hybrid Collaboration of several international research groups working on wakefield acceleration was launched in 2017 to advance the research field of hybrid L-PWFA. Experiments are carried out in the laboratories of three partners; at the Center for Advanced Laser Applications (CALA), Garching; the Helmholtz Zentrum Dresden Rossendorf (HZDR); and at Laboratoire d'Optique Appliquée (LOA), Paris. Theoretical input is provided by groups from the University of Strathclyde and the Deutsches Elektronen Synchrotron (DESY) in Hamburg. A recent review paper describes the development of the field of hybrid acceleration in detail [49].

The present work builds on the collection of all these previous experiments and theoretical considerations. It is the first experimental work concentrating on the quality parameters of the witness beam. In this context, quality may concern the witness beams' energy stability or spectral and spatial density. The experimental and simulation findings obtained in the scope of this thesis answer some critical questions in the field of plasma-based particle acceleration.

Research goals

1. Implementation of a PWFA-stage driven by LWFA-generated high-charge electron bunches.

2. Implementation of an optically-generated down ramp for stable and reliable internal injection in the PWFA stage.

3. Characterization of electron beam and target parameters through existing diagnostics.

4. Identifying relevant parameters for the energy stability of internally injected witness beams from PWFA experimentally and in PIC simulations.

5. Optimization of the PWFA stage for high quality, i.e., low energy-spread, low divergence, and high-density witness beams.

Structure of this thesis

Chapter 1 introduces the theoretical concepts necessary to understand the experimental results presented in this thesis. After a concise revision of ionization mechanisms and basic plasma physics, the generation of wakefields is explained. The theory chapter concludes with a summary of different injection mechanisms.

Chapter 2 introduces the experimental infrastructure at the Center for Advanced Laser Applications in Garching, which was used to obtain the results presented in this work. It follows a short revision of previous experiments and particularly describes the LWFA experiments to generate the drive beam. The chapter concludes with a summary of the different experimental conditions under which data was taken.

Chapter 3 first reports a set of experiments to show controlled internal injection at a hydrodynamic density down ramp in the PWFA. The witness energy is controlled by adjusting the PWFA's injection position and plasma density. A high degree of energy transfer from the drive beam to the witness beam is confirmed, and values are compared to previous publications on PWFA experiments. An optically generated density down ramp is introduced as an alternative injection scheme. The plasma density perturbation is generated using an auxiliary laser beam. The density distribution is characterized, and witness beams are injected for different delays between the injector laser and wakefield driver. This injection scheme generates more stable witness beams than the previously used hydrodynamic down ramps.

Chapter 4 concentrates on the stability of the witness energy. The witness beams in this experiment have energy stability comparable to pure LWFA and PWFAs driven by conventional accelerators. The witness stability is compared to parameter scans in PIC simulations and theoretical predictions. The simulations reveal a stabilizing effect of beam loading by the witness beam on its energy gain. From this observation, conclusions for future experiments are drawn.

Chapter 5 presents a third set of experiments. They focus on the quality of the generated witness beams. These beams can have lower divergence and higher spectral charge density than the drive beams from LWFA. The witness beams' emittance is estimated based on measured bunch properties and simulations.

Chapter 6 starts with a summary of the central results of this thesis and an outlook on follow-up experiments. In particular, ways to obtain higher witness energies are discussed. The conclusions are based on theoretical considerations and some preliminary PIC simulations modeling future experiments. A discussion of potential applications of beams from a hybrid experiment concludes this thesis.

1 Theory and terminology

1.1 Ionization mechanisms

Ionization, the electron transfer from a bound state to the energy continuum, can be powered by photons. Light gases like Hydrogen and Helium have binding energies of tens of eV, making single photon processes at typical laser wavelengths ($\sim 1\,\mathrm{eV}$) impractical. As laser intensity increases, multi-photon processes become more effective. At even higher intensities, perturbative models for describing the ionization process become unsuitable. In these high-intensity scenarios, ionization can be understood by examining the interaction between the laser electric field and the atomic binding fields.

The lasers used for laser wakefield acceleration must be very intense, achieving in-focus electric fields that surpass the atomic field strength responsible for binding electrons to their parent ion. Therefore, the binding potential is deformed strongly enough to produce essentially free electrons. This ionization mechanism is called barrier suppression ionization (BSI). Wakefield acceleration experiments typically use Low-Z gasses. These gasses are fully ionized already early in the rising edge of the drive laser pulse. The actual wakefield formation then happens in a fully ionized plasma.

The Table in Fig. 1.1 summarizes the necessary laser field strength for BSI in Hydrogen and Helium.

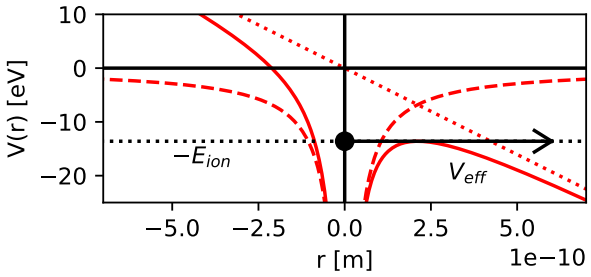

Ion	$E_{ion}[eV]$	I_{BSI} $[W/cm^{-2}]$
H^+	13.61	1.4×10^{14}
He^+	24.59	1.4×10^{15}
He^{2+}	54.42	8.8×10^{15}

Figure 1.1: ***Barrier suppression ionization.*** *Left: Schematic of BSI in a Hydrogen atom. A strong laser field with an intensity of* $1.4 \times 10^{14}\,\mathrm{W/cm^2}$ *(red dotted) distorts the atomic binding field (red dashed). The binding potential is suppressed in the superposition of both fields (solid red). This means that above this threshold external field, the bound electron can directly escape from the parent ion without tunneling. Right: Threshold intensities for barrier suppression ionization in some Ions. Table reproduced from [50].*

1.2 Basic plasma physics

Plasma definition

Plasma is often described as a quasi-neutral gas of charged particles with collective behavior. In this definition, collective behavior refers to long-range Coulomb interaction between the charged constituents. In plasma, the Coulomb interaction dominates over binary collisions, which dominate in neutral gasses. The long-range interaction of

the charged particles also causes quasi-neutrality. The charges naturally arrange in a way that minimizes their charge separation fields. Averaged over a sufficiently large volume, defined by the Debye length $\lambda_D = \left(\frac{\epsilon_0 k_b T}{n_e e^2}\right)^{1/2}$, the plasma therefore appears neutral. In this definition, $k_b T$ is the thermal energy of the plasma, n_e its density, ϵ_0 the vacuum permittivity, and e the electron charge. Note that the Debye length must be shorter than the dimension of the investigated interaction volume and that a sphere with radius λ_D must contain a sufficiently large number of electrons to be treated as a statistical ensemble. These conditions are fulfilled for all realistic parameters within the scope of this work.

Plasma oscillations

Consider an infinitely large, cold, and quasi-neutral plasma of density n_e in its equilibrium state. As a reaction to an externally applied force, a slab of electrons is displaced by a distance δ relative to the quasistatic ion background. This situation resembles a plate capacitor with a surface charge $\sigma = e n_e \delta$, with opposite signs on both plates. An electric charge separation field

$$E = \frac{e n_e \delta}{\epsilon_0} \tag{1.1}$$

builds up between both species, pulling back the electrons according to

$$m_e \frac{d^2\delta}{dt^2} = -eE = -\frac{e^2 n_e \delta}{\epsilon_0}. \tag{1.2}$$

This differential equation describes a harmonic oscillator. The electrons oscillate at the plasma frequency

$$\omega_p = \sqrt{\frac{n_e e^2}{\epsilon_0 m_e}} \tag{1.3}$$

around their initial position. ω_p, therefore, mainly depends on the local plasma electron density (and, for high light fields, on the electron's relativistic mass), which has profound implications for the propagation of light in plasma, as we will see in the next section.

Plane waves in vacuum

Before we analyze the light propagation in a plasma, the propagation of light in a vacuum is briefly recapitulated. A linearly polarized light field of frequency ω, and wave number k propagating along the z-axis shall be described by the plane wave solution to the homogenous (no free charges and currents) Maxwell's equations [51, 52]:

$$\vec{E}(z,t) = \vec{e}_x E_0 \sin(\omega t - kz) \tag{1.4}$$

$$\vec{B}(z,t) = \vec{e}_y B_0 \sin(\omega t - kz), \tag{1.5}$$

where $\vec{e}$ are unit vectors along the Cartesian coordinates. Maxwell's equations predict purely transverse electromagnetic waves with the propagation axis, E- and B-field forming an orthogonal system $\vec{B} = \frac{k}{\omega}\left(\vec{e}_z \times \vec{E}\right)$. This relationship implies that the amplitudes of electric and magnetic fields are related as follows:

$$B_0 = k/\omega \; E_0 = 1/c \; E_0. \tag{1.6}$$

Consequently, the effect of the B-field of an electromagnetic wave is c times smaller than that of the E-field.

Light waves in plasma

If an electromagnetic wave propagates in plasma, it interacts with the charged plasma constituents. Therefore, the dynamics of the plasma and the light propagation are coupled. This coupling gives rise to a much larger number of wave effects than commonly known from the vacuum propagation of an electromagnetic wave. In the following, the "ordinary" transverse electromagnetic wave is introduced in more detail, as it describes the propagation of a laser through plasma. The plasma will be treated as a fluid; by this assumption, a continuity equation for the number of particles applies. Together with the Lorentz force as the driving term in the equation of motion and the Maxwell equations for the propagation of the light field, a dispersion relation can be found [52, 53].

$$\omega^2 = \omega_p^2 + c^2 k^2$$

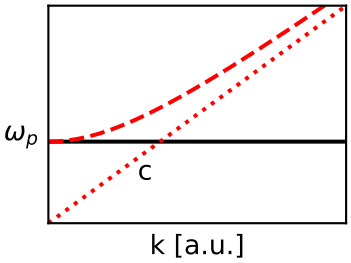

Figure 1.2: Dispersion relation of an e-m wave in a plasma. No traveling wave solutions exist for laser frequencies $\omega < \omega_p$.

From this dispersion relation, the group velocity of the laser in the plasma is derived as

$$v_g = d\omega/dk = \frac{2c^2 k}{2\omega} = \frac{2c^2\sqrt{\frac{\omega^2-\omega_p^2}{c^2}}}{2\omega} = c\sqrt{1-\omega_p^2/\omega^2} \tag{1.7}$$

We can identify the plasma refractive index as:

$$\eta = \sqrt{1-\omega_p^2/\omega^2} \tag{1.8}$$

The plasma refractive index is always smaller than one, and the phase velocity $v_p = c/\eta$ becomes super-luminal. However, this does not imply unphysical behavior, as the group velocity remains sub-luminal at $v_g = c\eta$.

High frequency ($\omega >> \omega_p$) light waves can propagate through the plasma at a group velocity close to one. For $\omega = \omega_p$, the plasma refractive index is zero. This

means the dispersion relation ceases to allow any traveling wave. The refractive index becomes a complex number for even smaller light frequencies ($\omega < \omega_p$). The incoming electromagnetic wave decays exponentially into the plasma and is reflected. The plasma density corresponding to the case $\omega = \omega_p$ is called the critical density. For laser light at 800 nm the critical density is $1.74 \times 10^{21}\,\mathrm{cm}^{-3}$. All densities discussed in the context of wakefield acceleration in this work are on the order of $10^{18}\,\mathrm{cm}^{-3}$; therefore, the laser can propagate in these plasmas. They are approximately 1000x underdense, implying a laser group velocity of $\sim 0.9995c$.

Electrons under the influence of strong electromagnetic waves

In preparation for describing the interaction of an intense laser field with a plasma, the interaction with a single free electron is analyzed. The Lorentz force couples electromagnetic fields (laser) with the motion of charged particles.

$$\frac{d}{dt}\left(\gamma m_0 \vec{v}\right) = -e\left(\vec{E} + \vec{v} \times \vec{B}\right), \tag{1.9}$$

with the Lorentz factor:

$$\gamma = \frac{1}{\sqrt{1 - \frac{v^2}{c^2}}} \tag{1.10}$$

At low intensities, the E-field (Eq. 1.4) determines the electron motion. The electrons will quiver around their initial position with an instantaneous velocity of

$$\vec{v} = -\frac{e}{m_e}\int \vec{E}dt = \frac{eE_0}{m_e}\vec{e}_x \int \sin(\omega t - kz)dt = \frac{eE_0}{m_e\omega}\vec{e}_x \cos(\omega t - kz) + const. \tag{1.11}$$

With increasing field strength, the maximum quiver velocity will eventually approach the speed of light within a half optical cycle. In this case, the relative strengths of the light's E and B fields are similar (see Eq. 1.6), and a relativistic treatment becomes necessary. The relativistic treatment includes the relativistic mass increase of the electron (γ in Eq. 1.9) and the inclusion of the v x B term. Based on this finding, the electric field is commonly normalized to the field necessary for a maximum quiver velocity of c (classical treatment). Consequently, the definition of the normalized vector potential is [54]

$$v_{\mathrm{quiver}} = \frac{eE_0}{m_e\omega} \stackrel{!}{=} c \implies a_0 := \frac{eE_0}{m_e\omega c}. \tag{1.12}$$

For the Ti:Sa laser wavelength of 800 nm, a field strength of $a_0 = 1$ corresponds to an intensity of $2.1 \times 10^{18}\,\mathrm{W/cm^2}$.

Electrons exposed to a relativistic plane wave ($a_0 > 1$) follow the laser's electric field and transversely oscillate at ω_l along the laser's polarization direction. In addition, when the electron approaches the speed of light, the v x B term of the Lorentz force results in an oscillation at $2\omega_l$ along the propagation direction of the laser. The combination of both oscillations leads to the well-known figure - 8 motion [54]. In the lab frame, the electrons undergo an additional drift along the propagation direction of

the light field. However, when the light field has passed, the electron is at rest again, and no net energy transfer has happened.

The situation becomes more interesting if the light field is transversely confined, i.e., working in the laser's focal region. In this arrangement, electrons feel a force due to the variation of the so-called ponderomotive potential. In the non-relativistic case ($a_0 << 1$), the ponderomotive potential is defined as the cycle-averaged kinetic energy of an electron exposed to the laser field. Plugging in Equation 1.11, one finds:

$$\langle E_{kin} \rangle = \frac{1}{2} m_e \langle v_e \rangle^2 = \frac{m_e}{2} \left(\frac{eE_0}{m_e \omega} \right)^2 \frac{1}{T} \int_0^T \cos^2(\omega t - kz) dt = \frac{m_e}{4} \left(\frac{eE_0}{m_e \omega} \right)^2 = \frac{m_e c^2}{4} a_0^2 \tag{1.13}$$

As in a laser focus a_0 is transversely varying, electrons feel a net force along the gradient of the ponderomotive potential

$$F_{pond} \propto \nabla a_0^2. \tag{1.14}$$

In the relativistic case ($a_0 > 1$), the expression for the ponderomotive force is more difficult to obtain. However, similar effects appear. The electrons escape from regions of the highest intensity and minimize their cycle-averaged kinetic energy. Intuitively, electrons are accelerated away from the intensity peak by the strong fields they see in focus. Half an optical period later, the field reattracts the displaced electrons. However, the electrons see a reduced field as they are now further away from the intensity peak. For this reason, the electron movement is effectively an oscillation superimposed by a drift down the gradient of the laser intensity.

Unfortunately, the electrons are not efficiently accelerated in the forward direction by that mechanism. On the timescale given by the electron plasma frequency, the ion background is quasi-static due to the ions' much larger inertia. Therefore, the displacement of the electrons creates strong charge separation fields, hindering the majority of ponderomotively accelerated electrons from leaving the interaction region. Instead, after the drive beam passes, the displaced electrons start oscillating around their resting position at the plasma frequency ω_p.

This process converts the field energy of the rapidly oscillating transverse laser field into a longitudinal field structure that is quasi-static in the reference frame of the driver and moves at almost the speed of light in the laboratory frame. We call this structure wakefield. It resembles in concept (not in detail) the wake a boat moving across water leaves on the surface.

1.3 Wakefield acceleration

A laser pulse or a bunch of charged particles disturbs an initially homogeneous plasma as it passes through it, creating strong charge separation fields. The subsequent sections discuss the specifics of generating these wakefields and the methods for utilizing them to accelerate electrons.

1.3.1 Wakefield generation

The typical size of the wakefields is determined by the plasma frequency ω_p. The plasma densities in the context of this work are on the order of $n_e = 10^{18}\,\mathrm{cm}^{-3}$; therefore, the corresponding plasma wavelength $\lambda_p = 2\pi c/\omega_p$ is on the order of a few 10s of Micrometers. This work concentrates on a regime where the wakefield is driven resonantly. For resonant excitation, the intense laser pulse or electron bunch acting as a driver must be shorter than half the plasma wavelength. In the same way, the driver must be transversely less extended than the transverse size of the wakefield.

Next, we introduce the mathematical treatment of a one-dimensional wake, which can be solved analytically.

1D description

A particularly handy, because easy to solve, description of a linear or nonlinear 1D plasma wave can be obtained under the quasistatic approximation. This approximation assumes that the wakefield driver evolution is negligible over one period of the plasma oscillation. Sprangle et al. proposed the following differential equation for the wakefield potential [55–57]:

$$\frac{\partial^2\phi}{\partial\zeta^2} = -\frac{k_p^2}{2} + k_p^2\frac{1+a^2}{2(1+\phi)^2} + k_p^2\frac{n_b}{n_0}, \tag{1.15}$$

which for a given laser amplitude $a(\zeta)$ and electron beam density $n_b(\zeta)$ allows to calculate the wakefield potential $\phi(\zeta)$ and from that, the wake's electric field $E_z(\zeta) = -E_0\partial\phi/\partial\zeta$ as a function of the comoving variable $\zeta = z - ct$. In this equation, $k_p = 2\pi/\lambda_p$ is the plasma wave number, n_0 is the background plasma density, and E_0 is the cold wave breaking limit that will be introduced in a moment. The derivation of this 1D differential equation for the wake potential is detailed in textbooks and review articles [50, 56, 58]. Sprangle et al. also give the differential equation for the slowly varying driver, which is omitted here for simplicity.

For both driver types, the normalized strength parameter in Equation 1.15 determines the linear or nonlinear regime of wakefield generation.

$$\text{Norm. Strength Parameter} \begin{cases} \frac{n_b}{n_0} \\ a_0 \end{cases} \quad \begin{cases} < 1 & \text{linear} \\ \approx 1 & \text{quasilinear} \\ > 1 & \text{nonlinear (in 3D: blowout regime)} \end{cases} \tag{1.16}$$

Figure 1.3 shows solutions of Equation 1.15. The case of a laser driver of varying amplitude, no electron bunch, and a plasma density of $1 \times 10^{18}\,\mathrm{cm}^{-3}$ was considered. In the linear case ($a_0 = 0.5$), the plasma density modulation (blue) and, therefore, the E_z field (black) oscillate sinusoidally as a function of the position behind the driver.

With increasing a_0, the shape and amplitude of the plasma density distribution changes, indicating a transition in the nonlinear regime. As exemplified in Figure 1.3(b), the nonlinear regime is characterized by a spiked density distribution and an elongation of the plasma wavelength. E_z drops almost linearly between subsequent spikes in the

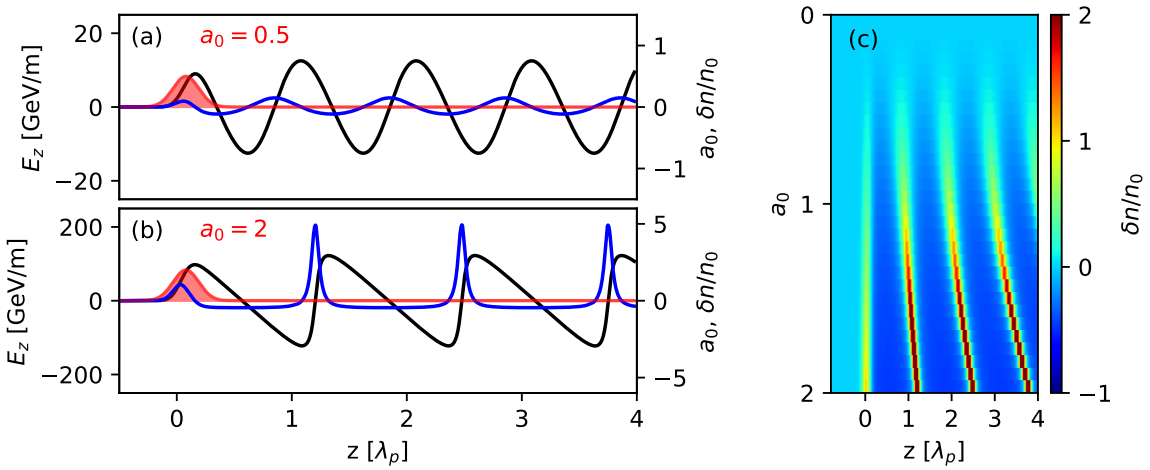

Figure 1.3: ***Solution of 1D wakefield equation for a plasma density of $1 \times 10^{18}\,\mathrm{cm}^{-3}$ and different laser driver strengths.*** *(a) Linear wakefield excited by a laser pulse with a_0=0.5 (red). The plasma density modulation (blue) and the E_z field (black) oscillate sinusoidally. (b) Nonlinear wakefield excited by a laser pulse with a_0=2. The plasma density distribution is sharply spiked, with an almost linear drop of E_z between subsequent spikes. Note that E_z is about 10x higher than in the linear case (a). (c) Plasma density distribution for varying a_0. The elongation and spiking of the nonlinear wakefield for $a_0 > 1$ are evident.*

nonlinear case ($a_0 = 2$). The amplitude of E_z increases with increasing driver strength. Values around 100 GV/m obtained for $a_0 = 2$ are similar to the cold wave breaking limit.

The wave breaking limit describes the highest field strength that can be achieved in a plasma wave before the fastest electrons overtake the wave, and thus, the electric field starts collapsing. This is conceptually similar to a water wave approaching the shore, eventually breaking at the point of its highest amplitude. A mathematical expression for the cold wave breaking limit can be obtained assuming a linear wake [59]:

$$E_{z,\max} = \frac{m_e \omega_p c}{e} \implies E_{z,\max}\,[\mathrm{V/m}] = 96\sqrt{n_0[\mathrm{cm}^{-3}]}. \tag{1.17}$$

Note the similarity to the definition of the normalized vector potential (Equation 1.2: $a_0 = 1 \implies E_0 = \frac{m_e \omega c}{e}$). The laser's electric field is normalized to the field strength at which an electron's quiver velocity (in non-relativistic treatment) approaches the speed of light. Analogously, the wake's electric field is normalized to the field strength at which the maximum velocity of an electron in the wake approaches c and, therefore, surpasses the wake's phase velocity. The wave breaking field in Equation 1.17 was derived under the assumption of a cold, non-relativistic plasma. The expression changes when including relativistic ($E_{z,\max} \uparrow$) and thermal effects ($E_{z,\max} \downarrow$) [60].

The 1D wakefield exemplifies nicely the transition into the nonlinear regime and allows us to estimate realistic values for the on-axis accelerating electric field. However, by definition, it fails to predict the transverse properties of the wakefields and, therefore, aspects of the transverse beam transport.

3D wakefield description

The excitations of wakefields in the 3D case can be intuitively understood when considering the driver as a snow plough. The plough will expel electrons in its way. Thus, a region with reduced electron density will be created after the driver. Since the ions hardly move on the time scale of the laser pulse duration, there will be a strong space charge force attracting electrons back and setting up a plasma oscillation. In contrast to the previously discussed 1D case, the displacement and oscillation of the plasma electrons in the 3D case take place in both the longitudinal and transverse directions. As a result, the wakefield is composed of longitudinal (accelerating or decelerating) and transverse (focusing or defocusing) electric fields.

As in the 1D case, there are different regimes of wake excitation. In the linear case (a_0 or $\frac{n_b}{n_0} < 1$), the plasma density undergoes sinusoidal oscillations. With increasing driver strength, the plasma response becomes more complex. In the highly nonlinear case (a_0 or $\frac{n_b}{n_0} >> 1$), the driver can expel all electrons from its way, leaving a volume void of electrons surrounded by a thin sheath containing the expelled electrons. This regime is referred to as the blowout or bubble regime.

While a 3D description of the linear wakefield generation can still be solved analytically, the nonlinear case is mathematically challenging, and no analytical solution exists. Usually, Particle-in-Cell (PIC) simulations are used for quantitative analysis of 3D nonlinear wakefields. Today, many PIC codes are available, and based on these codes, numerous articles have been published discussing wakefield acceleration in different regimes.

Based on the findings from PIC simulations in the nonlinear regime, different analytical models were derived to predict the shape of the plasma bubbles in the blowout regime. The theoretical works by Lu [61, 62] and Pukhov [13, 63, 64] are best known: They allow us to derive scaling laws for the wakefields. However, these theories are only valid in specific limited parameter ranges and usually require further fitting parameters from PIC simulations.

1.3.2 Comparison of laser and electron driver

High-intensity laser pulses and high-current particle beams can excite strong wakefields. Although the wakefields are similar for both drivers, there are distinct differences in the excitation phase. The following section discusses the advantages and disadvantages of both accelerator schemes, and introduces the hybrid L-PWFA scheme that strives to combine both types of wakefield accelerators most advantageously.

Plasma generation

A high-intensity laser, as used for LWFA, is very efficient in ionizing the gas target via BSI. This results in the formation of a wakefield in a fully ionized plasma, as hydrogen is ionized early in the rising edge of the drive laser pulse.

In PWFA, the high-current electron drive beam has the ability to ionize a narrow plasma column through its space charge field. However, the transverse extent of the

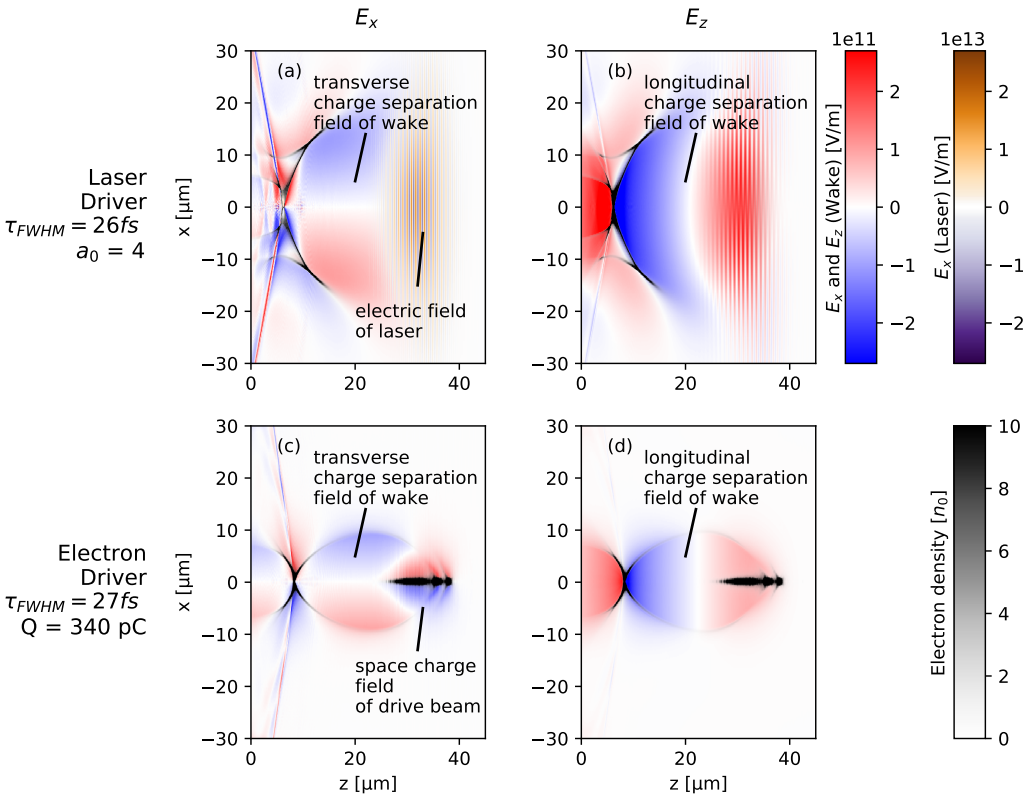

Figure 1.4: ***Comparison of wakefields driven by an intense laser or a high-current electron beam.*** *The plots show PIC simulations of the wakes' transverse and longitudinal electric fields for laser and electron-driven wakefields at a plasma density of* $2 \times 10^{18}\,\mathrm{cm}^{-3}$*. The transverse size of the wakefield is slightly larger in the LWFA case due to the wider driver. However, LWFA and PWFA provide similar high accelerating and focusing fields on the order of* $200\,\mathrm{GV/m}$*. Note, that in the electron-driven case (c+d), the transversely oriented Coulomb field of the driver has similar strength as the charge separation field it sets up. In contrast, the oscillating laser field (a), plotted on its own color scale, is two orders of magnitude stronger.*

ionization volume is usually smaller than the transverse extent of the wakefield [42, 43, 65], resulting in smaller wakefield amplitudes in a beam-self-ionized case (see Section 3.3 and 5.2.1). To counteract this, the target usually needs to be pre-ionized with an auxiliary laser beam or via a discharge.

Field strength

The LWFA and PWFA considered in this work operate at similar densities, providing equally small and high-gradient accelerating structures. Figure 1.4 shows the transverse and longitudinal electric fields for laser and electron beam-driven wakefields in the blowout regime.

As seen before, in LWFA, the ponderomotive force of the laser sets up the plasma wave. The wakefield excitation is proportional to the gradient of the laser intensity.

Table 1.1: Comparison of laser and electron driver.

Driver	**LWFA** relativistic laser pulse	**PWFA** high-current electron bunch
Availability	High (university labs)	Low (national labs)
Stability promise	Problematic, high susceptibility to driver fluctuations	Good (this work)
Ionization	Excellent (BSI)	Can be problematic (pre-ionizer needed)
Divergence	Problematic (laser diffraction, guiding necessary)	External focusing can be necessary depending on experiment
Dephasing	Problematic (low plasma density necessary)	Usually negligible
Depletion	Usually similarly severe as dephasing for typical LWFA parameters	Usually limiting factor

In contrast, the unipolar and transverse space charge field of a relativistic particle driver is more efficient in pushing away electrons, as it interacts directly via Coulomb interaction with plasma electrons. Consequently, seemingly weaker particle bunches with transverse fields $\sim 100\,\mathrm{GV/m}$ can excite wakefields of the same strength as laser drivers with peak electric fields $\sim 10\,\mathrm{TV/m}$. The transverse and longitudinal fields in these plasma waves are similar to the Coulomb field of the electron driver.

Acceleration limits: Divergence, dephasing, and depletion

Three main limiting factors exist for the achievable energy in a plasma accelerator: Driver divergence, dephasing, and depletion. The significance of these three effects is different for both driver types. Table 1.1 summarizes the main differences between both driver types.

Divergence

Divergence generally limits the acceleration length both for laser and electron drivers. However, the relevant length scales differ. For a laser pulse, diffraction limits the distance over which the beam can stay tightly focused. This distance is characterized by the Raleigh length $z_r = \pi w_0^2/\lambda_0$ and scales quadratically with the focus size. Unfortunately, the focus size is not a free parameter as it needs to be chosen small enough to meet the resonance conditions and to achieve high enough intensity. As an example, for a focus diameter of $w_0 = 30\,\mu\mathrm{m}$ and a laser wavelength of $\lambda_0 = 0.8\,\mu\mathrm{m}$, the Raleigh length is $3.5\,\mathrm{mm}$.

For an electron beam, the space charge forces of the beam itself make it diverge. The beams' beta function $\beta = \sigma_r^2\gamma/\epsilon_n$ is conceptually similar to the laser's Raleigh length. Beta scales not only with the transverse size σ_r of the beam but also with its relativistic gamma factor γ and the normalized emittance ϵ_n. For realistic beam parameters of $\sigma_r = 5\,\mu\mathrm{m}$, $\epsilon_n = 1\,\mu\mathrm{m}$, and $\gamma = 500$, the electron beam can stay focused

for about 13 mm. Furthermore, the electron beam will converge and stay focused as soon as it sees the wakefield it creates [66] (see Section 1.3.5).

Relativistic self-focusing of the laser drivers and guiding in preformed plasma channels makes the difference between both driver types less severe. However, diverging drivers are generally a more difficult problem to control in LWFA than in PWFA.

Dephasing

Dephasing arises from the difference in the group velocity of a laser and an electron bunch. The laser's group velocity in a plasma ($v_g = c\sqrt{1-\omega_p^2/\omega^2}$, Eq. 1.7) is always smaller than c. A relativistic electron bunch, on the other hand, travels at a velocity of $c\sqrt{1-1/\gamma^2}$, which is very close to c for highly relativistic electron beams. Therefore, for highly relativistic electron bunches, specifically for $\gamma >> \omega/\omega_p$, the electrons will eventually outrun the laser and slip into a decelerating phase of the wakefield. The dephasing length L_d can be defined as the distance after which the electron bunch advanced by half a plasma wavelength relative to the drive laser:

$$L_d = \frac{\lambda_p}{2}\frac{c}{(c-v_g)} = \frac{\lambda_p}{2\left(1-\sqrt{1-\omega_p^2/\omega^2}\right)} \simeq \frac{\omega^2}{\omega_p^2}\lambda_p \tag{1.18}$$

For densities on the order of a few $10^{18}\mathrm{cm}^{-3}$ and a 800 nm laser, the dephasing length is on the order of several mm. In the nonlinear regime ($a_0 \geq 1$), the expression for L_d needs to be modified to account for the increase in plasma wavelength, but yields similar results [62].

In contrast, in a PWFA, both the driver and the witness are relativistic electron beams and dephasing is usually not a problem. For large values of γ the phase slippage gets practically negligible. For example a 20 GeV and a 40 GeV electron bunch will slip by only 0.2 µm during a propagation of 1 m. This consequence of special relativity is also why at SLAC, multi-10 GeV energy gain was achieved in a single stage [33]. In conclusion, similarly to driver divergence, dephasing is generally a more considerable concern in LWFA than in PWFA.

Depletion

Depletion is a direct consequence of energy conservation, as the laser or electron driver spends its energy on exciting the wakefield.

Analyzing the head erosion of the drive laser, the pump depletion length L_{pd} in a nonlinear LWFA is approximately [62]:

$$L_{pd} = \frac{\omega^2}{\omega_p^2} c\tau, \tag{1.19}$$

where τ is the pulse length of the drive laser. For plasma densities in the order of a few $10^{18}\mathrm{cm}^{-3}$ and a 800 nm laser with a pulse length $\tau \simeq 30$ fs, the pump depletion length is similar to the dephasing length in the order of a few mm.

In PWFA with plasma densities in the order of a few $10^{18}\mathrm{cm}^{-3}$, the decelerating fields are on the order of few 100 MeV/mm. Consequently, at driver energies of few 100 MeV, the interaction length is limited to few mm. Usually, different parts of the drive bunch decelerate at different rates. Therefore, the energy spread of the driver will typically increase. At some point, the electrons at the position of the strongest decelerating field will become non-relativistic. Consequently, they fall back and stop contributing to the wakefield formation. In the worst case, they are recaptured in the accelerating phase of the wakefield and further reduce the fields at the position of the witness bunch. Furthermore, it has a negative impact on the efficiency of the PWFA stage if the acceleration ends before the entire drive beam has been decelerated. In conclusion, depletion is usually the limiting factor for witness acceleration in a PWFA.

Stability limitations of LWFA

In addition to the limitations mentioned above on the achievable energy gain in a plasma accelerator, there are further problems with regard to energy stability, especially in comparison to conventional radiofrequency accelerators. The exact size, shape, material, and all other properties of radiofrequency cavities have been optimized over many decades. They are also very precisely manufactured and additionally controlled with feedback loops. The cavities in LWFA, on the other hand, are not only orders of magnitude smaller, but also a new train of cavities is created on every shot. Its formation depends sensitively on laser and plasma parameters and their variations. For example, Maier et al. find that percent-level variations in laser energy and 100 µm-level shifts in focus position cause correlated energy fluctuations of the order of a few percent [38]. In addition, active control loops for the laser drivers [67] are only being developed gradually and are missing from many experiments so far. Due to these differences, the stability and reproducibility of electron properties, particularly their energy, currently are much better in conventional accelerators.

A hybrid L-PWFA approach can partially help to solve the stability problems of an LWFA stage. Admittedly, the stability of a conventional accelerator is not achieved because hybrid acceleration simply adds another plasma accelerator stage with the limitations discussed previously. However, in PWFA, the mechanism that generates the wakefield is more robust to fluctuations in the driver. This robustness is explained below using an illustrative model, which explains why a hybrid L-PWFA can be more stable than an LWFA alone.

1.3.3 A toy model: Balancing Coulomb forces in an electrostatic bubble

[1] The robustness of a PWFA stage towards fluctuations of the drive beam can be understood from a simplistic analytical model in which the Coulomb force of a relativistic drive bunch balances the space charge force of the ion column it creates. This model can explain the influence of the driver beam properties and its fluctuations on

[1] The following derivation of the mathematical model is copied from the author's publication [68].

the wakefield strength in a PWFA experiment. The electric field of a single, highly relativistic electron is concentrated in a narrow cone with an opening angle $\sim 1/\gamma$ transverse to the direction of propagation. In the limit $\gamma \to \infty$ the electric field in the laboratory frame is given as:

$$\vec{E}_e(r,z) = \frac{e}{2\pi\epsilon_0}\frac{\vec{e_r}}{r}\delta(z-ct), \tag{1.20}$$

where r is the radial coordinate and e the electron charge. In the high-energy limit, the electric field is purely oriented in the transverse direction $\vec{e}_r$. Therefore, the field is confined in z-direction to the position of the generating electron. Furthermore, the Coulomb field described by equation 1.20 does not depend on the electron energy. Let us now consider an electron bunch with a total charge Q as an axially symmetric ensemble of charges on the z-axis, creating a current I. Assuming that the beam is contained within a radius r_0, the field at a transverse distance $r > r_0$ is given by

$$\vec{E}_b(\zeta,r) = -\frac{I(\zeta)}{2\pi\epsilon_0 c}\frac{\vec{e}_r}{r}\,, \tag{1.21}$$

with $I(\zeta)$ the current profile of the beam in the comoving variable $\zeta = z - ct$, ϵ_0 the vacuum permittivity and c the speed of light. Note, that for an elongated bunch of highly relativistic electrons, even without taking the limit $\gamma \to \infty$, the Coulomb field of the bunch is almost purely transverse, and only the slope of the field along z at the head and tail of the electron bunch depends on γ.

For sufficiently narrow and high-current beams ($I > \sim 1\,\mathrm{kA}$), the Coulomb field expels all plasma electrons from its path leaving behind a homogeneous and symmetric ion column. The space charge field of the ion column E_{ion} attracts the plasma electrons back:

$$E_{\mathrm{ion}}(r) = -en_0 r/2\epsilon_0\,. \tag{1.22}$$

After the driver has passed, and thus, in the absence of the driving Coulomb force, the electrons will fall back on the axis and start oscillating radially. Restricting ourselves to short ($\sigma_z \ll \lambda_p/2$) drive bunches an almost spherical ion cavity surrounded by a sheath of displaced plasma electrons is formed. Figure 1.4(c) shows a simulation of the transverse electric fields of an electron beam-driven wakefield in the blowout regime. The opposing fields of the driver and the ion background during the wakefield excitation are evident.

The maximal radial displacement of the sheath is usually referred to as the *blowout radius* r_{bo}. A useful scaling of r_{bo} can be obtained by calculating the radial distance at which the electrostatic force of the ion background (Eq. 1.22) cancels out that of the drive beam (Eq. 1.21). Evaluating Eq. (1.21) at the point of maximum current I_0 we obtain

$$r_{\mathrm{bo}} \simeq \sqrt{I_0/\pi e c n_0} \propto \sqrt{I_0/n_0}\,. \tag{1.23}$$

By balancing electrostatic fields, the model's validity is implicitly restricted to slow plasma electrons in the sheath, for which the electric field determines the Lorentz force. A more careful derivation taking into account the relativistic motion of the

plasma electrons and the magnetic field in the blowout [69] yields $E_{\mathrm{ion}}(r) = -en_0 r/4\epsilon_0$ and $r_{\mathrm{bo}} = \sqrt{2I_0/\pi e c n_0}$. This is the same functional dependence but with modified constants.

In the case of a strong blowout, the rear side of the plasma sheath approximates a half-sphere. Under this assumption, the absolute value of the accelerating field inside the ion cavity increases linearly from the cavity center with a slope [70]

$$\partial_\zeta E_z \simeq en_0/2\epsilon_0 \,. \tag{1.24}$$

Evaluating Eq. 1.24 at a distance r_{bo} from the cavity center yields the maximum accelerating field

$$E_z^{\max} \simeq -en_0 r_{\mathrm{bo}}/2\epsilon_0 \propto -\sqrt{I_0 n_0} \,. \tag{1.25}$$

The final witness energy is given by the accelerating field and the time it is exposed to this field. Equation 1.25 is derived for the maximum longitudinal accelerating field at the very end of the ion bubble. However, the witness will see a smaller field depending on its position relative to the driver.

The scaling from the simplified model (Eq. 1.25) predicts possibly high stability of the witness energy. This is because the accelerating field does not depend on the (relativistic) energy of an elongated driver. Furthermore, the square-root scaling damps the variations of driver charge and plasma density. A further distinct difference to LWFA is that the current of a relativistic drive beam is essentially nonevolving until (parts of) the driver are decelerated to non-relativistic energies. In contrast, the a_0 of a laser driver varies under propagation depending on the details of the laser and plasma density distribution.

The stability argument based on Equation 1.25 is only valid if depletion is not yet reached. In other words, if a long enough target or high enough plasma density is chosen, the witness energy will increase with increasing driver energy because a wake can be driven for longer.

In Chapter 4 (*Stability of staged L-PWFA*), the experimentally achieved stability will be compared to this simplified model. Furthermore, the model is used for basic estimates of the emittance of PWFA-generated electrons.

TAKE-HOME MESSAGE

In PWFA, the wakefield strength does not depend on the energy of the elongated and highly relativistic drive beam (at least as long as it is still highly relativistic, i.e. far from depletion). Furthermore, the influence of fluctuations of the driver charge is damped since the wakefield strength scales with the square root of the driver current.

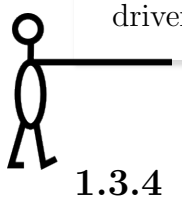

1.3.4 Beam loading

The calculation of the blowout effect is applicable not only for a driver but also for a witness located anywhere within the wakefield. In such a case, the driver and witness fields add with a phase offset and lead to beamloading effects.

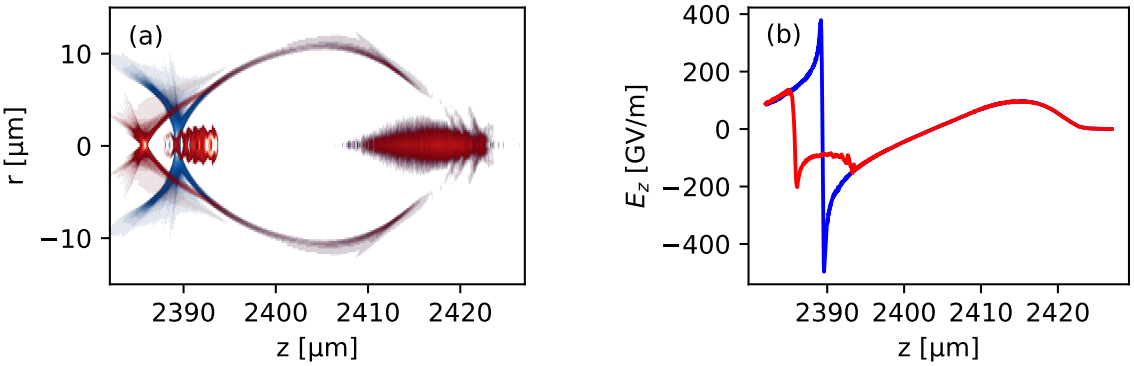

Figure 1.5: ***Beamlaoding in a PWFA.*** *(a) shows the outline of wakefields in the bubble regime. The electron distribution is retrieved from a PIC simulation of PWFA. A case with a witness (red) and no witness (blue) is compared. The red sheath trajectory is bent further outwards at positions behind the witness beam, and the bubble elongated. (b) shows E_z for both cases from panel (a). In the scenario with the witness beam, the field is reduced at positions behind the front of the witness.*

The Coulomb force of the witness beam gives an extra outward push to the sheath electrons of the laser-generated wakefield [71, 72]. As they usually bend towards the axis in the accelerating phase, this extra kick makes the sheath trajectory more "cylinder-like". In the extreme case of an infinitely long cylinder, this leads to zero longitudinal field due to symmetry reasons. In realistic scenarios, the result of beam loading will be a reduction in field strength and, in turn, lower final electron energy.

As seen in Figure 1.5, the bending of the sheath trajectory due to the presence of a witness bunch is also observed in PIC simulations. If adequately tailored, beam loading can be used to flatten the accelerating fields and to produce narrow bandwidth electron bunches [73, 74]. If the witness charge is too high (as in the red case shown in Figure 1.5) the slope of E_z does not flatten but even reverses at longitudinal positions beyond the head of the witness beam. This field distribution leads to energy decreasing towards positions behind the head of the witness. Depending on the strength of the beamloading and the length of the electron bunch, the highest acceleration gradients and highest electron energies can still occur in the tail of the beam. [29].

TAKE-HOME MESSAGE

Beam loading can be described as the ability of the (witness) electron bunch to modify the wakefield structure substantially. In the presence of a high current witness, the effective accelerating fields will be lower than in the unloaded case. Beam loading is crucial in the context of Hybrid L-PWFA as high current electron bunches can beam load an LWFA and drive a PWFA in the absence of a laser.

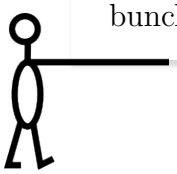

1.3.5 Betatron oscillations

An electron bunch located in the correct phase of a wakefield is exposed to longitudinally accelerating fields and also transversely focusing fields (compare Fig. 1.4). In the case of a full blowout and a homogeneous ion background, the transverse dynamics of the bunch can be modeled as a harmonic oscillation. In the simplified model introduced above, equation 1.22 describes the electrostatic Coulomb force due to the ion background, leading to a differential equation:

$$F = m_e\gamma\, \ddot{r} = eE_{\mathrm{ion}}(r) = -\frac{e^2 n_0}{2\epsilon_0} r \tag{1.26}$$

This differential equation describes a harmonic oscillation at the betatron frequency

$$\omega_\beta = \sqrt{\frac{e^2 n_0}{\epsilon_0 m_e 2\gamma}} = \omega_p/\sqrt{2\gamma}. \tag{1.27}$$

On the one hand, this transverse motion of the electron bunch leads to the emission of X-rays, which were not analyzed in the scope of this thesis. On the other hand, the same force provides the transverse focusing of the electron bunch. This focusing is crucial for recapturing the diverging electron bunch from the LWFA stage in the PWFA stage. Furthermore, an estimate of the witness' emittance based on calculated betatron trajectories will be presented in Section 5.5 (*Emittance and Brightness of the beams*).

The term *betatron oscillation* made it into common use in the context of wakefield acceleration. It originally referred to transverse oscillations around a stable orbit in a circular accelerator – specifically, in a Betatron [6, 7]. Particles that move away a small distance from the stable orbit experience a force pushing them back to the correct radius. The origin of this focusing force is not identical to the ones observed for betatron oscillations in a wakefield accelerator. Nevertheless, the term *betatron oscillation* is now used for all kinds of transverse oscillation of particles in an accelerator.

1.4 Injection

Witness electrons need to be injected both in LWFA and PWFA stages. Most of the mechanisms discussed here apply to both accelerator types. However, this introduction concentrates mainly on the details of internal injection in PWFA, as it is one of the central research questions of this work.

1.4.1 Down ramp injection

If the longitudinal phase velocity of some plasma electrons is higher than the wake's phase velocity, these fast electrons can be trapped and continuously accelerated. The necessary phase velocity $\beta_z = v_z/c$ of plasma electrons located at the end of the first

bubble is [69][2]:

$$\beta_z > \frac{\beta_b}{1 + \frac{\chi}{k_p}\frac{1}{2n}\frac{dn}{dz}}, \tag{1.28}$$

where $\beta_b = v_b/c \approx 1$ is the phase velocity of the drive beam, n the plasma density, $\frac{dn}{dz}$ the gradient in the density down ramp, χ the phase position of a plasma electron in the wake, and $-\frac{\chi}{k_{p,0}} \overset{\text{at } \chi=-2\pi}{=} \lambda_p$ corresponds to the plasma wavelength at the background density (note the negative sign).

In a density down ramp, the plasma wavelength increases in the positive z-direction. As a consequence, the phase velocity at the back of the wakefield is reduced by the rate of this elongation. This reduced phase velocity gives electrons more time to catch up with the wake. To summarize, the inequality 1.28 describes two prerequisites for successful injection: First, a high velocity β_z of plasma electrons, which favors the strong blowout regime for down ramp injection in a PWFA. Secondly, the density down ramp $\frac{dn}{dz}$ must be sufficiently steep for a given wakefield strength. There are different ways of creating these steep density down ramps in plasma targets.

Shock from an obstacle in a supersonic gas flow

Hydrodynamic shock fronts are routinely produced by introducing obstacles in the gas flow of a supersonic jet from a Laval nozzle. Such obstacles are typically either knife edges (e.g., a silicon wafer) or wires. Figure 1.6(a) schematically shows a setup with a knife edge to create the shock and the resulting density distribution [18, 19].

This method is a reliable injection scheme and provides tunability of the electron energy. However, it comes with some disadvantages. The shock generation relies on the supersonic gas flow, limiting this method to Laval-nozzle-type targets. Also, the position of the shock is coupled to the stability of the gas flow. This coupling makes the injection scheme prone to energy jitter. Additionally, the gas flow determines the shock angle, which is generally not perpendicular to the driver axis. Oblique shocks are problematic as the orientation of the shock turns out to be important for the quality of the injected electron bunch [75].

Optically-generated density down ramp

Most experiments in this work rely on an optically-generated down ramp for injection. This scheme uses a laser pulse to structure the plasma density distribution. Figure 1.6(b) schematically shows the setup and the temporal development of the density perturbation.

In the first step, a laser locally ionizes the plasma via optical field ionization (OFI). During the ionization process, the electrons are heated to temperatures of a few eV [76]. The spatially confined heating of the electrons leads to a volume of increased pressure. Subsequently, the electrons will expand in the surrounding neutral gas, pulling the ions with them. As a result, an outward propagating shock wave at the ions speed of

[2]The version of Eq. 1.28 presented here uses non-normalized units and therefore differs from the cited reference.

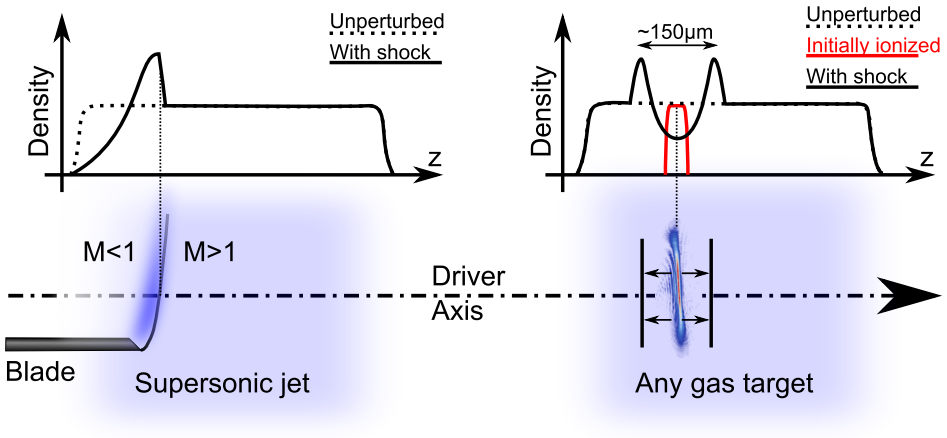

Figure 1.6: ***Schematic of obstacle-generated and optically-generated shock front.*** *(a) An obstacle sticking in a supersonic gas flow creates a shock. (b) In the optically-generated down ramp scheme, a laser pulse is focused transversely into a gas target. Over time the initially ionized region expands, and an outward-moving shock is formed.*

sound $c_s = \sqrt{Zk_bT_e/m_i}$ will develop [77]. For a temperature of the plasma electrons of $T_e = 20\,000\,\mathrm{K} \hat{\approx} 2\,\mathrm{eV}$ the speed of sound is

$$c_s = \sqrt{1.4 \times 10^{-23}\,\mathrm{J/K} \times 20\,000\,\mathrm{K}/1.7 \times 10^{-27}\,\mathrm{kg}} = 13\,\mu\mathrm{m/ns}. \tag{1.29}$$

The shock front provides a rather steep density gradient, which can be used to trigger injection. The same physical mechanism of plasma machining is used in the creation of hydrodynamic optically-field ionized (HOFI) guiding channels[76, 78–81]. Instead of shooting through the optically-generated pipe, the density perturbation is created transversely and the outer wall of the shock structure is used as a down ramp.

This optically-triggered injection scheme was previously used in LWFA experiments [20, 21, 82] but was not implemented in PWFA. Most of the previous works used round foci of the injector laser. This geometry makes the setup quite sensitive to pointing jitter. Using a few 10 mJ of laser energy for the injector beam, the focus can be made astigmatic to increase the stability, while keeping the intensity level high enough for field ionization. Our specific experimental implementation for internal injection in the PWFA is discussed in the methods chapter, Section 2.3.4

2 Framework of this Thesis and Experimental Setup

2.1 PIC simulations

Particle-in-cell (PIC) simulations are an important tool for understanding the structure of wakefields. They are always used when no analytical solution of the wakefield equations (see Section 1.3.1) can be found. This is particularly the case when a three-dimensional description is required and the drivers are strong enough for the solution to deviate from a simple sinusoidal variation of the plasma density.

PIC codes simulate the interaction of charged particles and electromagnetic fields in a self-consistent way. This means that in the PIC cycle, the particle dynamics and the electromagnetic fields of the particles are retrieved from each other and updated alternately in an iterative manner. For simulating plasma dynamics, an ensemble of macroparticles represents the plasma charges. These macroparticles can move freely in the simulation box. However, the particles' phase space distribution (density and momentum) is interpolated on a fixed grid. From this charge distribution, the resulting E and B fields are retrieved on the grid.

For the simulations in this work, the PIC-code FBPIC (Fourier-Bessel Particle-In-Cell) was used [83]. FBPIC differs from many other 3-dimensional PIC codes in that it uses a cylindrical coordinate system. In principle, the representation of particles and fields in radial and azimuthal coordinates is equivalent to a representation in Cartesian coordinates. However, the choice of these coordinates makes the code very fast in situations where high azimuthal resolution is not required. When a PWFA is initialized with a cylindrically symmetric drive bunch, the wake is also cylindrically symmetric. Therefore, the full 3D problem is reduced to a 2D problem in the radial and longitudinal coordinates. The second distinctive feature of FBPIC is its field solver: E and B fields are calculated from Maxwell equations in spectral space as this procedure is numerically more robust [84].

PIC simulations are presented in Chapter 4 and Chapter 5. An exemplary input deck and a detailed discussion of software parameters are given in appendix A.

2.2 ATLAS3000 at CALA

The experiments for this dissertation were carried out with the ATLAS-3000 laser system of the Center for Advanced Laser Application (CALA) in Garching, an institute of the Ludwig-Maximilians-University Munich. ATLAS3000, whose properties are described in detail below, is a Petawatt Ti:Sa laser delivering multiple 10 Joule pulse energy at a pulse length below 30 fs. This type of high-power, short-pulse laser system is crucial for the Hybrid L-PWFA experiments discussed in this thesis, as it can resonantly drive the LWFA stage at plasma densities on the order of $10^{18}\mathrm{cm}^{-3}$.

CALA, whose mission centers around developing laser-driven particle and x-ray sources for medical applications, also houses other lasers and radiation-protected areas

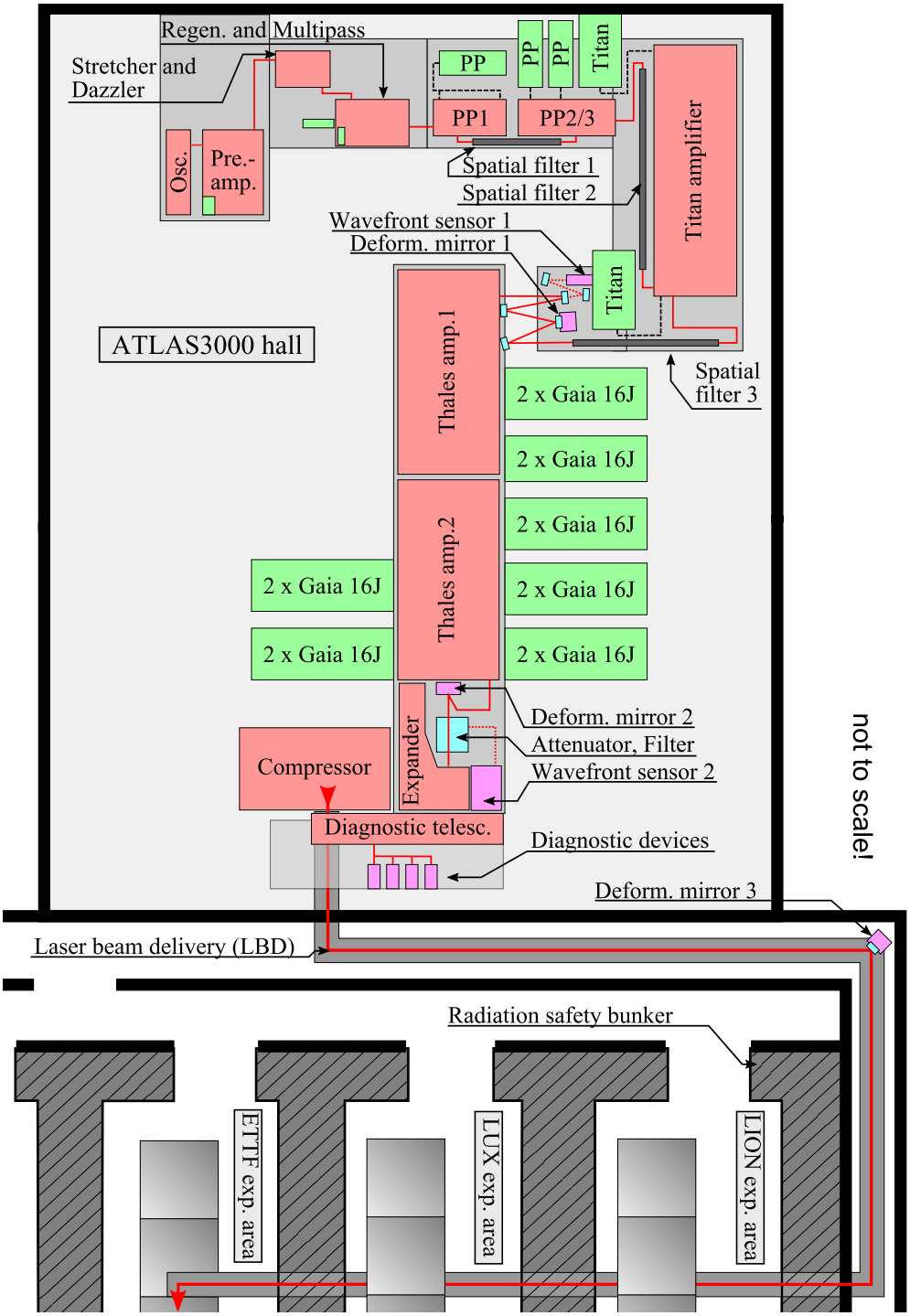

Figure 2.1: ***Overview of the CALA laser and experiment area.*** *Layout adapted from [85].*

for the application experiments (see Fig. 2.1), which in this case took place in the Electron and Thomson Test Facility (ETTF) (see section 2.3).

2.2.1 General layout of the laser system

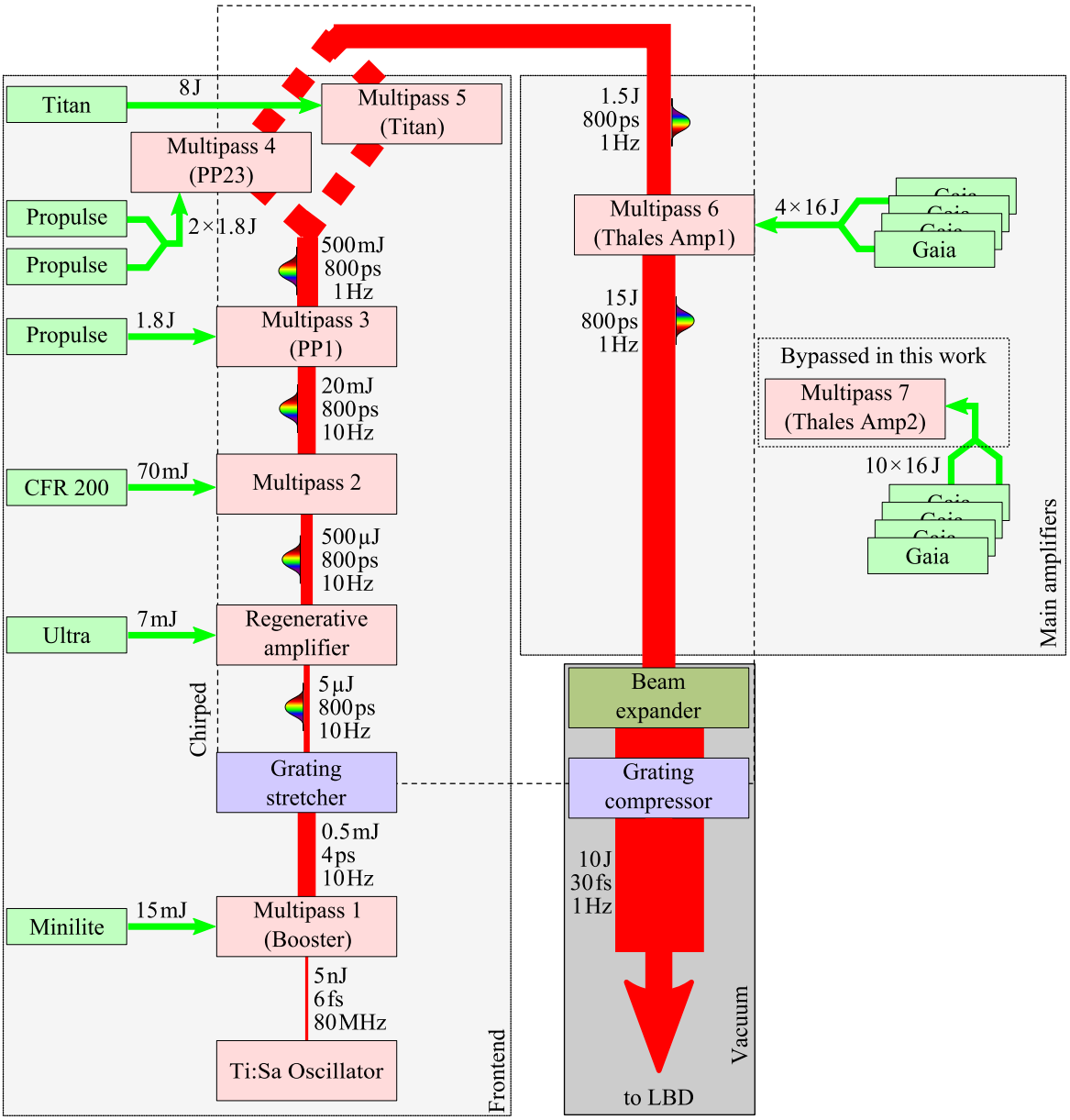

Figure 2.2: ***Building blocks of the ATLAS3000 CPA laser system.*** *Layout adapted from [85].*

ATLAS3000 is one of the world's most powerful laser systems, and it has the following main parameters: ATLAS3000 is a chirped pulse amplification (CPA) [11] system based on Titanium-doped Sapphire as a gain medium. The laser can deliver pulses with up to 70 Joule at a pulse length below 30 fs and a repetition rate of 1 Hz. In order to achieve these parameters, ATLAS consists of the following building blocks that are further detailed below: The laser pulses from a commercial oscillator are stretched in a grating stretcher and amplified in a series of homebuilt preamplifiers. The pulses are

then brought to their final energy in two main amplifiers called Amp1 and Amp2 (see Fig. 2.2). After full amplification, the beam is transported in a vacuum, magnified in an in-house custom built beam expander, and then compressed to below 30 fs in an in-house custom built grating-based pulse compressor (see Fig. 2.3). After compression, the laser is either sent onto the diagnostic table or into the beam delivery system, which transports the laser to the experimental areas (see Fig. 2.1). The modules Oscillator to Multipass 4/5 are referred to below as the frontend. This part of the current system at CALA is mainly identical to the 300 TW laser system used at the former Laboratory for Extreme Photonics (LEX) and was recently described in detail in Gilljohann's dissertation [85].

Frontend

The homebuilt frontend of the ATLAS3000 consists of the following building blocks (see Fig. 2.2): The laser chain starts from a commercial 80 MHz, fs-modelocked oscillator (Laser Quantum Venteon), which replaced a former 70 MHz oscillator (Femto Lasers Rainbow) during this work. Subsequently, a Pockels cell picks pulses at 10 Hz from the oscillator pulse train. These pulses are pre-stretched to the ps-level in a glass block and amplified to the 1 mJ-level in a first multipass amplifier (Multipass 1 in Fig. 2.2).

Next, the pulses are stretched to approximately 800 ps in a grating stretcher. After the stretcher, an acousto-optic modulator (Fastlite Dazzler) allows for dispersion control and spectral shaping. Due to the limited efficiency of the acousto-optic modulator, the pulse energy is reduced to the 1 µJ-level. The following amplifier is a regenerative amplifier (regen) in ring configuration supplied by Amplitude. As a high gain amplifier, the regen brings back the pulse energy to around 500 µJ. After the regen, a multipass amplifier (multipass 2 in Fig. 2.2) boosts the pulse energy to 20 mJ.

Several multipass amplifiers (3, 4, and 5 in Fig. 2.2) subsequently increase the pulse energy to 1.5 J. These multipass amplifiers are all pumped by flashlamp-pumped, frequency-doubled Nd:YAG lasers (Amplitude ProPulse and Titan). After Multipass 3, 4, and 5, telescopes equipped with spatial filters clean the wavefront and successively magnify the beam. The frontend previously delivered up to 10 J. Therefore, not all amplifiers are needed to reach the desired seed energy of 1.5 J for the main amplifiers. Depending on the availability of the pump lasers, different configurations have been implemented over time by bypassing either multipass 4 or 5.

New main amplifiers by Thales

During the upgrade from ATLAS300 to ATLAS3000, two final power amplifiers (Multipass 6 and 7 in Fig. 2.2, referred to as Thales Amp1 and Amp2) built by Thales were added to the system.

Amp1 is a 4-pass amplifier with a nominal beam diameter of 6 cm. The Ti:Sa crystal is pumped by 4 times 16-J, 532 nm, ns flashlamp-pumped YAG laser with 1 Hz repetition (Gaia HP). The pulse energy after Amp1 is up to 25 J. After Amp1, a Galilean telescope expands the beam to a beam diameter of 9 cm. During the thesis, the refractive telescope provided by Thales was replaced by a reflective telescope to

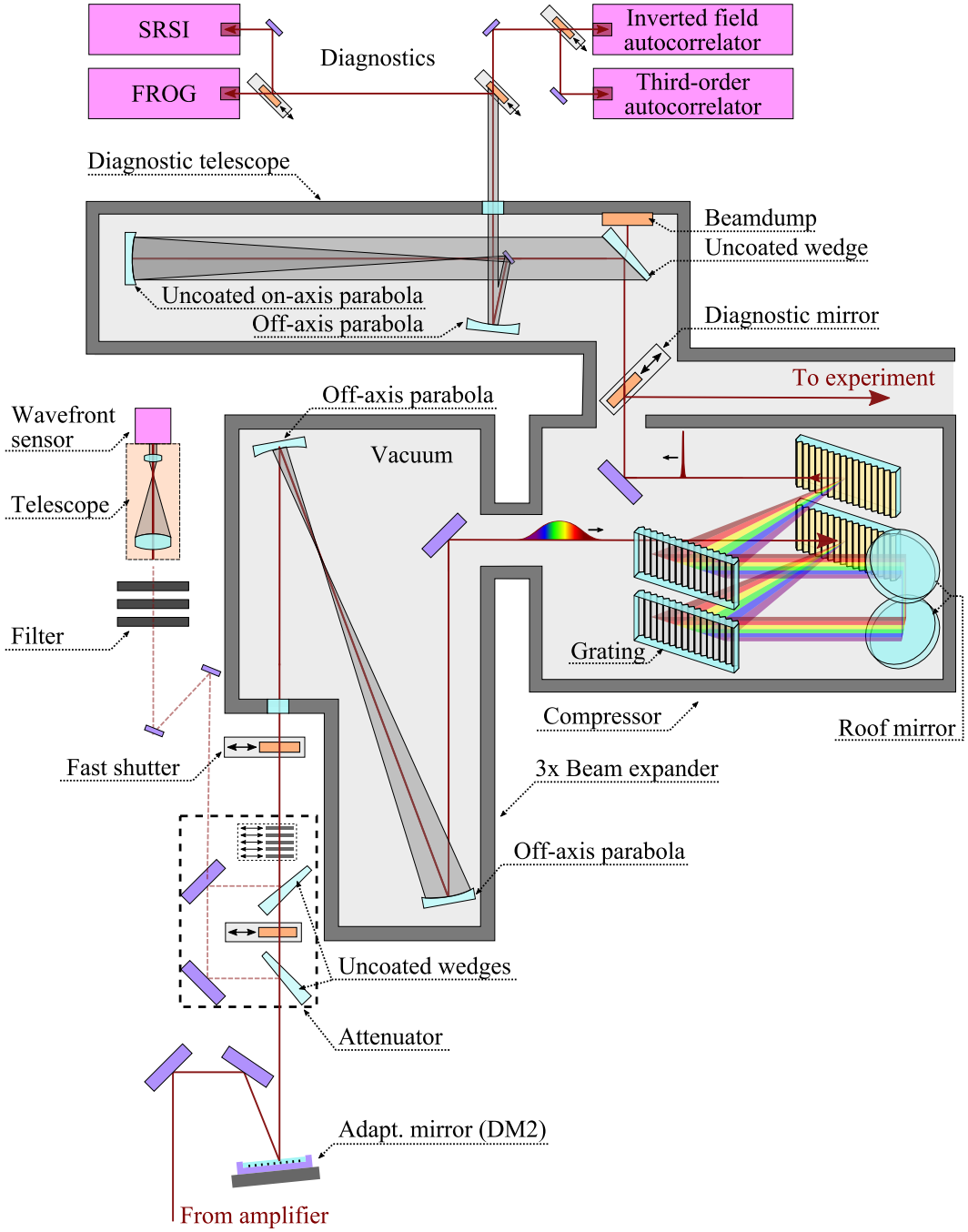

Figure 2.3: ***Layout of the ATLAS3000 compressor and diagnostics.*** *Layout adapted from [85].*

minimize spatio-temporal couplings (see section 2.2.4).

Amp2 is a 3-pass amplifier. The Ti:Sa crystal is pumped by 10 Gaia HP. When using all pump lasers, the system can produce pulse energies of more than 90 J before compression. Both amplifiers' input and output are equipped with a diagnostic suite to monitor their performance. The diagnostic suite comprises of a near-field camera, a spectrometer, and an energy meter.

As detailed in the following, these and other diagnostics are used for thorough control of all beam parameters (spatially, temporally/spectrally, and stability). Due to the high intensity on target, spatial and temporal wings of the laser will notably interact with the plasma. Consequently, imperfections in the beam must be suppressed as well as possible.

2.2.2 Spatial beam shaping

There are different ways to passively and actively optimize and stabilize the laser wavefront.

For the experiments presented in this work, Amp2 was bypassed. This configuration limits the pulse energy after amplification to about 20 J. However, bypassing Amp2 also has three big advantages concerning the stability of the LWFA experiment. Firstly, the beam path in air is shortened, and therefore, the laser is less susceptible to wavefront distortions caused by air convection. Secondly, the smaller beam picks up fewer aberrations from gratings, beam line, and focusing optics. Both effects lead to an increase in achievable focus quality. Thirdly, the smaller beam diameter increases the confocal parameter, which reduces the effect of spatial intensity fluctuations in the plasma gradient.

For active wavefront optimization, there is a collection of three spatial filters in the frontend and three deformable mirrors placed strategically in the laser chain. The first deformable mirror DM1 (ISP system) has 35 actuators and an active diameter of 60 mm. DM1 is placed between the frontend and the main amplifiers. The wavefront is optimized in a closed loop with a wavefront sensor (Phasics). DM1 is needed to ensure smooth propagation through the final amplifiers, as spatial filters can not be practically implemented at the given beam size and energy.

After Amp2, there is a second 52-actuator deformable mirror DM2 (ISP system). It also operates in a closed loop with a wavefront sensor (Phasics). This adaptive mirror guarantees a flat wave front and good propagation through the compressor. Furthermore, the mirror can compensate for variations in the collimation of the laser due to different thermal lensing in the final amplifiers when working at different amplification levels.

The quality of the focal spot in the experiment is optimized using DM3, a 300 mm deformable mirror with 52 actuators (ISP systems) in the vacuum beam line. A reflective attenuator reduces the laser intensity far enough to image and record the focus at the target. After the final focus, the beam is imaged onto a home-built Shack-Hartmann sensor for wavefront retrieval [86]. The retrieved wavefront is used in a closed loop with DM3 for focus optimization. The results of the focus optimization are presented in Section 2.3.

2.2.3 Spectral and temporal beam shaping

Due to the limited spectral gain curve of Ti:Sa, the laser spectrum tends to narrow and redshift during amplification. However, to support short pulses, the spectral width of the pulses needs to be maintained. Spectral filters for passive spectral shaping are

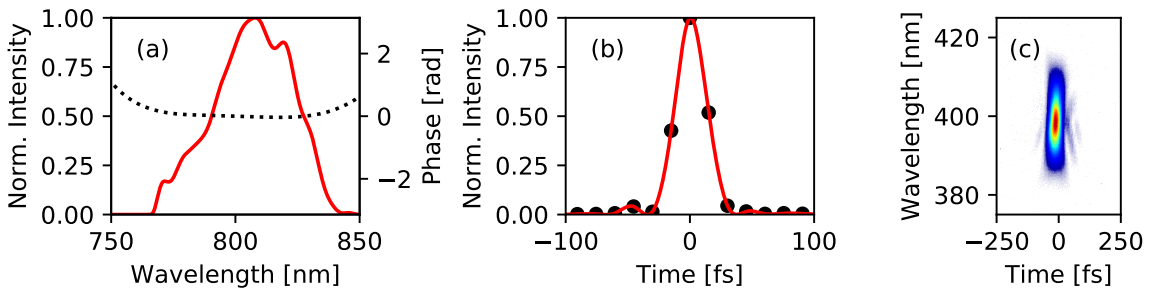

Figure 2.4: ***Pulse compression of ATLAS3000.*** *Panel (a) and (b) show the results of a self-referenced spectral interference measurement (Wizzler). The spectral phase was optimized in a closed loop with the Dazzler. Panel (c) shows the FROG trace of the optimized pulse. The clean trace confirms the absence of higher-order spectral phase errors. The ATLAS pulses typically have a 27- to 30-fs (FWHM) pulse length, depending on their spectral shape.*

implemented at different positions in the laser chain. In the first amplifier (booster), the beam passes through a spectral notch filter before each pass. The spectral filter suppresses the central gain maximum and increases the spectral wings' relative intensity. After the frontend, the spectral redshift, due to the gain in the final amplifiers, is precompensated by a pair of reflective spectral filters. Two acousto-optic modulators (Fastlite Dazzler and Mazzler) in the laser chain enable active spectral shaping. The most effective tool for spectral shaping is the Mazzler, as it is located inside the regen cavity and acts on the beam during each amplification pass. The desired spectral shape is optimized in a closed loop, with a spectrometer supplying the feedback signal.

A dedicated diagnostic section for temporal pulse diagnostics has been set up after the grating compressor. An uncoated wedge and an uncoated on-axis parabola in vacuum attenuate the beam (see Fig. 2.3). The parabola is part of a demagnifying Keplerian telescope. After reducing the beam diameter to 4 cm, the strongly attenuated beam exits the vacuum through a thin window and propagates in air. It is relay-imaged onto the input apertures of several diagnostic devices.

The gratings of the compressor are aligned to compensate for the stretcher dispersion and most of the summed-up material dispersion of the laser chain. The residual spectral phase is recorded by self-referenced spectral interference (SRSI; Fastlite Wizzler) and eliminated in a closed loop with the Dazzler. A measurement device based on frequency-resolved optical gating (FROG; Swampoptics GRENOUILLE) is used to visually confirm the absence of higher-order spectral phase errors. The typical pulse length of ATLAS3000 is 27 to 30 fs (FWHM), depending on their spectral shape.

FROG and Wizzler have a high temporal resolution but a limited dynamic range in intensity and time. A third-order autocorrelator (UltrafastInnovations Tundra) confirms the good temporal contrast of the laser pulses on a ns-scale. The amplified spontaneous emission (ASE) contrast level at several 100 ps before the pulse is on the order of $1 : 10^{10}$ (see Fig. 2.5). The coherent contrast becomes worse than $1 : 10^{9}$ only within the last 50 ps and worse than $1 : 10^{6}$ within the last 5 ps.

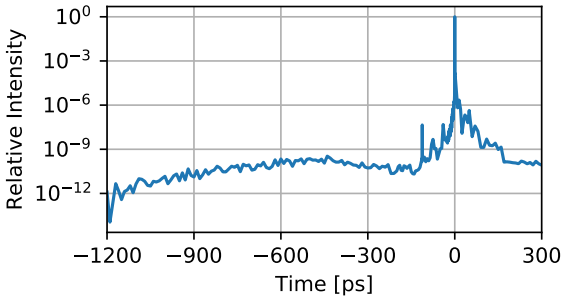

Figure 2.5: ***Typical temporal contrast of ATLAS3000.*** *The temporal contrast was measured using a third-order auto-correlator (UltrafastInnovations Tundra).*

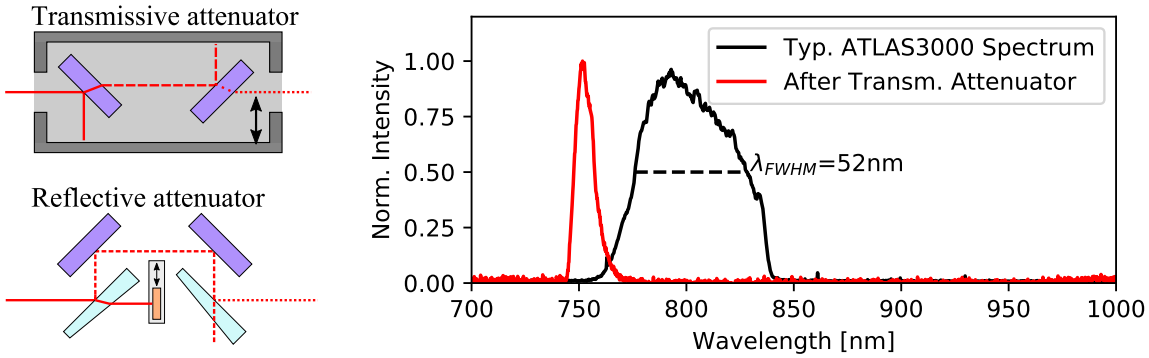

Figure 2.6: ***Typical spectrum of ATLAS3000.*** *The black line represents a typical spectrum of the ATLAS3000 laser after full amplification. For comparison, the transmission of the former transmissive attenuator is plotted (red). The spectrum of the new reflective attenuator closely resembles the fundamental spectrum. Note that the spectra are normalized and that the attenuated beam contains about* 10^5 *times less energy than the full beam.*

2.2.4 Spatio-temporal couplings

So far, spatial and temporal beam properties have been discussed separately. However, especially at relativistic intensities, the effects of spatio-temporal couplings (STCs) on the laser-plasma interaction become non-negligible [87]. STCs are related to a variation of the wavefront of different frequency components. The lowest-order STCs are pulse front tilts arising from linear angular dispersion. Consequently, different spectral components are transversely displaced in focus, leading to an increased focal spot and a decreased local spectral width. Both effects limit the achievable intensity in focus. In ATLAS, a custom built inverted field auto-correlator characterizes these pulse front tilts after compression. The in-house custom built compressor allows for individual alignment of all gratings. Therefore, the gratings can be adjusted to minimize residual pulse front tilts.

To enable the characterization of STCs by spectrally resolved wavefront measurements at the target [88], the spectrum of the attenuated diagnostic beam needs to be similar to the unattenuated beam. To this end, a new reflective attenuator was

implemented during this thesis's time frame. The previous implementation of a transmissive attenuator used the leakage of two dielectric mirrors. As a result, the spectrum measured in the experiment was not representative of the full laser spectrum as the mirrors mainly let through light at the blue spectral edge of the pulse (see Fig. 2.6).

2.3 Experimental area: ETTF

The experiments for this work are conducted in the Electron and Thomson Test Facility (ETTF), one of the target areas within CALA. The experimental area is 3 m wide, 18 m long, and inside a radiation safety bunker. The experiment is set up in a 14 m-long vacuum chamber with a transverse profile of $\sim 1 \times 1$ m^2.

2.3.1 Beam focusing

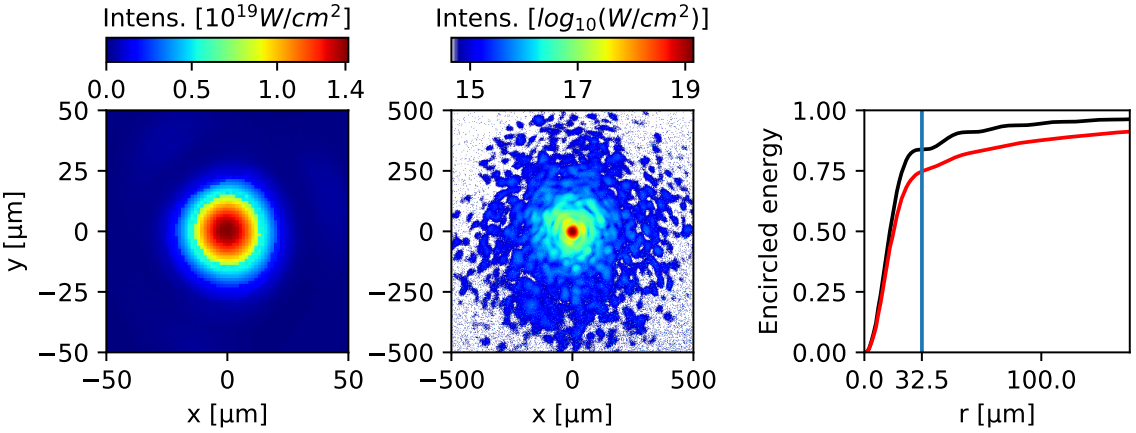

Figure 2.7: ***ATLAS3000 focus in ETTF.*** *The left panel shows the central part of the focus on a linear color scale. The middle plot shows an HDR image of the focus on a logarithmic scale, covering the full dynamic range of 4.5 orders of magnitude and the full field of view of* $1\,\mathrm{mm}^2$*. The right panel shows the encircled energy as a function of the radial position for the ATLAS3000 focus (red) and an ideal Airy pattern (black).*

The first 6 meters of the vacuum chamber are used as the beam handling and focusing area. For this work, a 6 m focal length parabola is used. The final amplifier, Amp2, and the magnifying telescope between Amp1 and Amp2 are bypassed during the experiments. Therefore, the beam diameter after amplification is 6 cm and, consequently, 18 cm before focussing. This results in an F/33 focusing geometry. The measured FWHM focus diameter is 26 µm (27 µm) in x (y) dimension. The focal spot quality is optimized using DM3 in closed-loop with a home-built Shack-Hartmann sensor for wavefront retrieval [86]. The reconstruction of the focal spot (see Fig. 2.7) has a calculated Strehl ratio of 82%, defined as the reduction in peak intensity compared to the focus of a perfect top-hat beam with a flat wavefront, and assuming that all energy

is contained within the dynamic range of 4.5 orders of magnitude and within the spatial field of view of 1 mm by 1 mm (170 μrad by 170 μrad). These assumptions neglect that parts of the beam are scattered at even larger angles due to scattering from dust and scratches, high-order wavefront distortions, and diffraction from pick-off mirrors in the beam. Note that the high dynamic range (HDR) focus image was retrieved from seven different filter settings with ten shots averaged per setting. Therefore, the HDR image represents an average focus quality, and the single-shot focus quality could still fluctuate (the shot-to-shot intensity variation was measured at 4% in the focal plane on a representative day).

The calculated peak intensity of the laser of $\sim 1.4 \times 10^{19}\,\mathrm{W/cm^2}$ has a significant error margin of 20%. This uncertainty arises from the unknown compressor and beam line transmission. The combined transmission was measured to be $\sim 2/3$ during the commissioning of the system. Retrospectively, it was figured out that this value quickly dropped to values below 0.5 due to blackening of the beam line mirrors and, to a lesser extent, the diffraction gratings. The typical time scale of degradation is on the order of a few shooting days or about 10,000 shots equivalently. The blackening can be removed by exposing the optical surface to an oxygen plasma or ozone atmosphere. The affected optics are meanwhile equipped with permanent setups for cleaning and are cleaned as needed. However, at the time of the experiments presented in this work, the severity of the blackening was not known, and the cleaning setup did not yet exist. Consequently, the exact transmission values during the experiment can not be reconstructed.

2.3.2 Target area

The central part of the ETTF chamber hosts the interaction region. In the scope of this thesis, a new target holder has been designed. For the hybrid L-PWFA experiments, the main components of the target are two separate gas jets with variable spacing serving as LWFA and PWFA, respectively, and a plasma mirror in between them (see Figure 2.8). All components are mounted on a Hexapod for precise positioning relative to the laser focus. The setup is accessible for optical probing (see section 2.3.3) and optical injection (see section 2.3.4). The main components of the target are discussed in the following, and a more detailed description of the setup can be found in Appendix C.

Double-jet target

The plasma targets for LWFA and PWFA were gas jets from de Laval-type nozzles. Both nozzles are round and have exit diameters of 5 mm (LWFA) and 4 mm or 7 mm (PWFA) (see Appendix C for more details on the nozzle design). The nozzles create supersonic gas jets of adjustable gas density. The first nozzle uses a gas mixture of 96% H_2 and 4% N_2. Together with a silicon wafer in the supersonic gas flow, which creates a sharp density down ramp this setup provides the conditions for using shock-front assisted ionization injection in the LWFA stage [89]. The LWFA stage is operated at a plateau plasma density of $1.3 \times 10^{18}\,\mathrm{cm^{-3}}$. The full density characterization can be found in section 2.3.3. The second nozzle uses either pure Hydrogen or a gas mixture

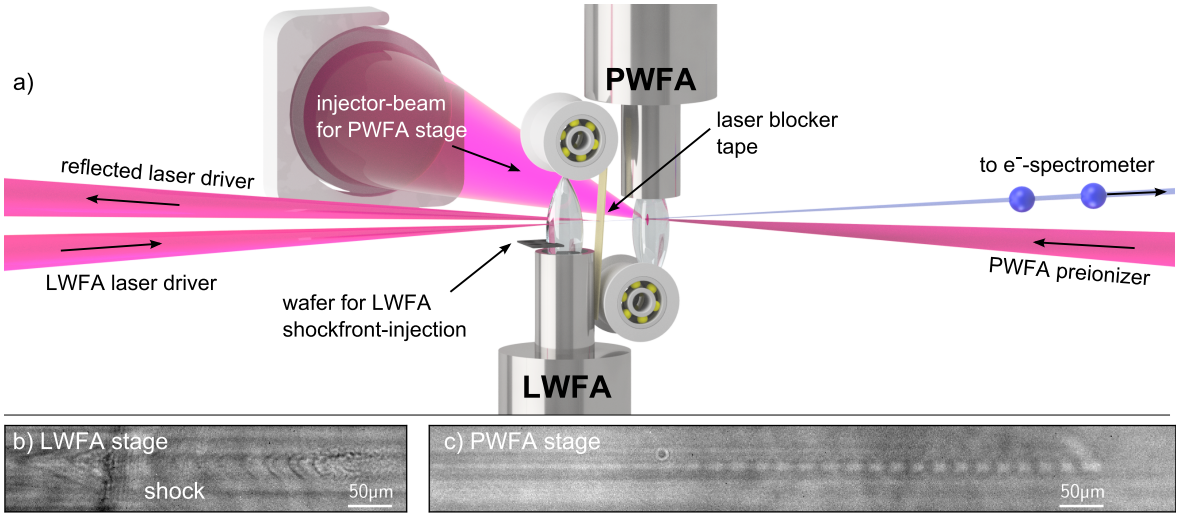

Figure 2.8: ***Experimental setup for staged LWFA-PWFA with internal injection in the PWFA stage.*** *Schematic of the double-jet setup for staged LWFA-PWFA experiments. The ATLAS3000 laser propagates from left to right along the z-axis in the first plasma. This setup generates LWFA electrons via shock-front-assisted ionization injection. The removable 25 µm-thick polyimide tape after the first jet prevents the laser from entering the second jet for some experiments. The second gas target serves as the PWFA. An auxiliary laser beam picked from the main beam serves as an injector. For experiments with laser blocker tape, the second target can be pre-ionized with another auxiliary laser beam. A few-cycle probe was used to image the laser-driven plasma wave in the LWFA stage (b) and the electron-driven plasma wave in the PWFA stage (c).*

of Hydrogen and Helium or Nitrogen[1]. Further details on the second nozzle in all experimental conditions are discussed in the respective chapters and are summarized in Table 2.1 (see page 46).

LWFA electrons exhibit a small source size but comparably large divergence on the order of a few mrad. To provide a sufficiently dense electron bunch as a driver for the PWFA stage, the gap between the gas jets has to be small, typically on the order of several millimeters. In this setup, however, the laser is potentially still strong enough to drive a wakefield independently. For proof of principle experiments, an additional laser blocker tape is placed in the small gap between the jets to differentiate between both driver mechanisms.

Laser blocker tape

A simple plasma mirror removes the spent drive laser after the LWFA. A removable 25 µm-thick polyimide tape serves as the plasma mirror. The laser ignites an overdense surface plasma and is reflected. In experiments with a laser blocker, an additional beam can be delivered from the downstream direction to pre-ionize the second gas jet (see

[1]The gas mixture was used in preparation for experiments on all-optical density down ramp (Torch) injection [90–92]. However, no evidence of Torch injection was found, and this subject is not covered in more detail in this work for compactness.

section 5.2.1 for a discussion of the effect of the preionizer). The residual transmission through the plasma mirror is calculated by comparing the beam's brightness on a scattering screen downstream of the target with and without tape in place. The measured transmission is on the order of a few percent (see Apendix C.3). The exact value depends on the energy level and the position of the tape relative to the focus position. Given the measured transmission, the laser is not expected to drive a wakefield in the second jet. The influence of the tape on the relativistic electron bunch will be discussed in Chapter 4, including in particular the beam's divergence increase and emittance degradation because of the Weibel instability [93].

2.3.3 Diagnostics

The last 6 meters of the ETTF vacuum chamber downstream of the target host the diagnostics section.

Dipole spectrometer and spectrum analysis

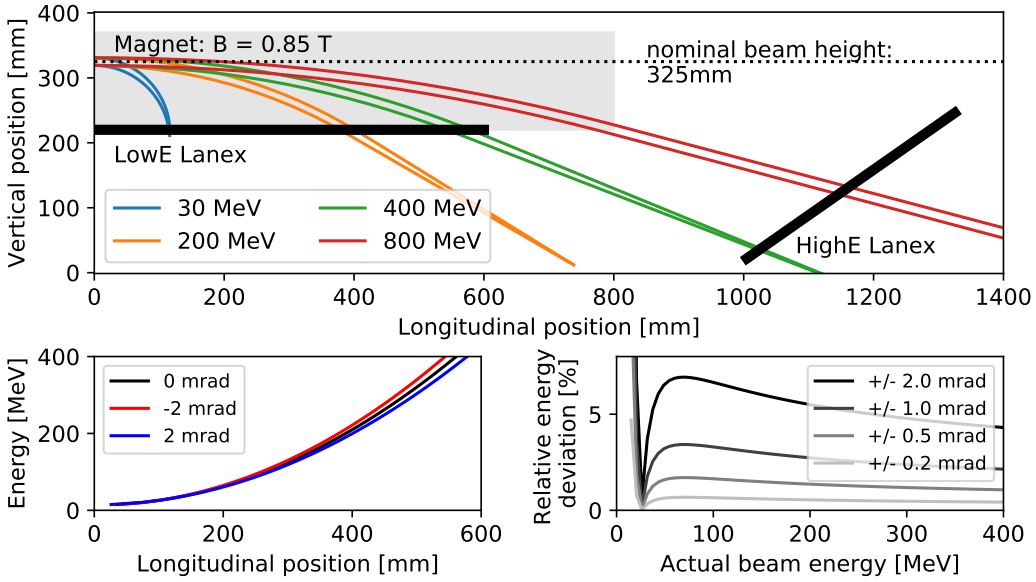

Figure 2.9: ***Magnetic dipole spectrometer.*** *Electrons are energy-selected in a magnetic dipole and detected via scintillating screens. The top panel shows example trajectories for four energies and a deviation of +/- 2 mrad from the nominal beam pointing. The lower left panel shows the energy calibration curve for different values of the initial beam pointing. The lower right panel shows the absolute value of the relative energy deviation for different values of the initial beam pointing.*

The electron beam spectrometer (Figure 2.9) consists of an 80 cm long dipole magnet, 2.9 m downstream of the wakefield accelerator. The electron trajectories are bent inside the magnetic field of $B_\perp = 0.85\,\mathrm{T}$, on a circular orbit with the energy-dependent Larmor radius $r_L = \frac{\gamma m_e c}{e B_\perp}$. The electrons intercept with a scintillating screen

(Lanex) after exiting the magnetic field. For energies $> 400\,\mathrm{MeV}$ a second scintillating screen is placed further downstream behind the magnet. The scintillation light is imaged onto an array of cameras. The spectrometer and the scintillator light yield are fully calibrated [94–96]. For most energies, the electron trajectories with different initial beam pointing do not cross in the plane of the scintillating screen. Consequently, the electron energy deduced from the interception position depends on the beam pointing (see Figure 2.9 lower left). If necessary, this uncertainty can be eliminated by moving an additional scintillation screen in front of the dipole magnet. This allows the pointing and divergence of the electron beams to be measured. The measured energy variations due to the varying angle of the electron trajectories also limit the energy resolution to the few-percent-level for beams with divergences of about 1 mrad (see Figure 2.9 lower right).

During the analysis of the experiments, inconsistencies in the previous charge calibration routine were noticed. For details of the calibration of the electron spectrometer, see Appendix B

Optical probing

In ETTF, optical probe beams are available to characterize the plasma targets. For the probe, a half-inch mirror picks a small portion of the laser pulse just after entering the ETTF chamber. In the most straightforward configuration, the probe beam is directed to the target and crosses the gas target perpendicular to the propagation direction of the drive beam. The interaction plane is imaged onto a camera using an achromatic lens (1:1 or 1:2 imaging). In addition to this overview probe beam, further beams, and imaging modes are available for different applications.

Few-cycle-shadowgraphy

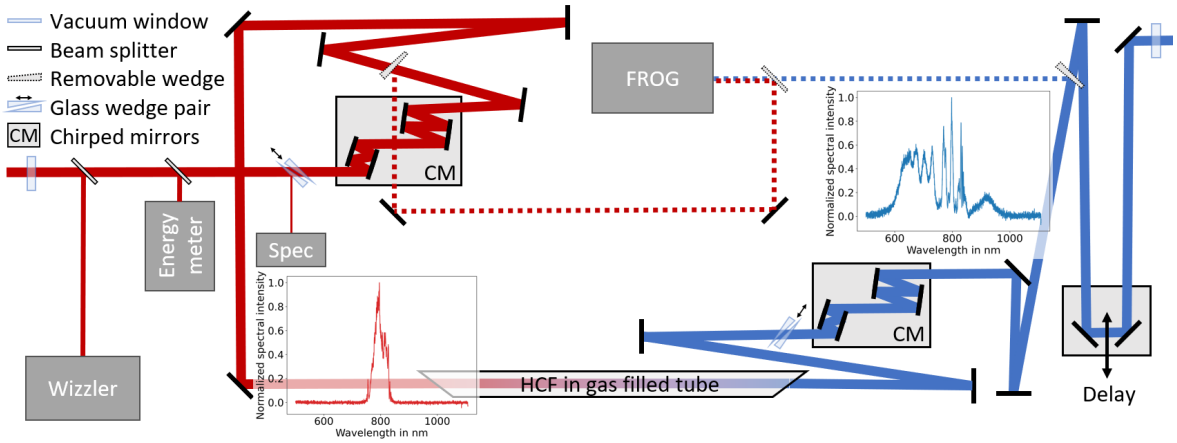

Figure 2.10: ***Setup for few-cycle probe beam generation.***[2]

[2]The schematic of the probe beam generation is reproduced by kind permission of Florian Haberstroh.

Few-cycle-shadowgraphy is used to directly visualize and identify the plasma waves driven by the laser or the electron beam in LWFA and PWFA, respectively (see Figure 5.1). For the few-cycle beam (see Figure 2.10), a small portion of the probe pulse is sent out of the vacuum, spectrally broadened, and subsequently compressed to sub 10 fs pulse length. For spectral broadening, approximately 500 µJ are focused into an Argon-filled hollow-core fiber. During 1 m of propagation, the spatial mode smooths, and the spectrum is broadened by self-phase modulation. Chirped mirrors compress the probe pulses close to their Fourier limit. The short pulse duration makes capturing images of the plasma wave possible. To achieve the necessary spatial resolution, the beam is imaged onto one or several spectrally filtered CCD cameras using a long working distance microscope (Mitutoyo 5x) combined with a suitable tube lens. For more details on generating the few-cycle probe, see Ding's dissertation [97].

Interferometry

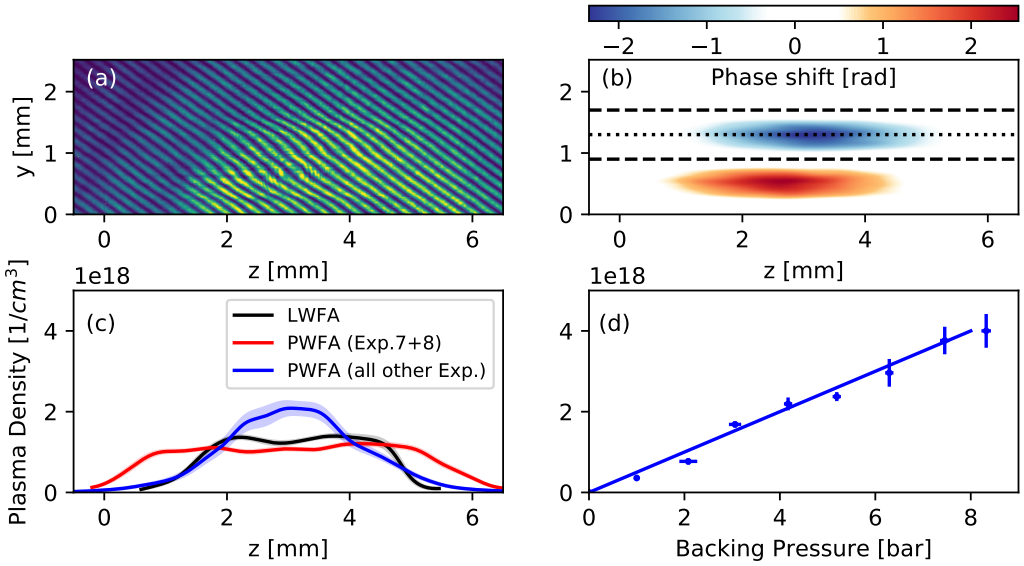

Figure 2.11: ***Plasma density distribution of the LWFA and PWFA targets.*** *The density was measured using a Nomarski interferometer. Panel (a) shows the recorded interference pattern (4 mm-diameter PWFA target), with the density information encoded in the bending of the interference stripes. Panel (b) shows the phase map extracted from (a) together with the laser axis (dotted line) and the area used for Abel transformation (inside dashed lines). Panel (c) shows a lineout of the reconstructed plasma density along the laser propagation axis for the 5 mm-diameter LWFA target (black), the 7 mm-diameter PWFA target (red), and the 4 mm-diameter (blue) PWFA target used in the experiment. The density measurements are taken under experimental conditions but with no density down ramp for injection created. Panel (d) shows the scaling of the plasma density in the 4 mm-nozzle with backing pressure.*

An interferometer setup characterizes the plasma density distributions in the LWFA and the PWFA target. In interferometry mode, the magnification of the probe imaging

system is chosen to see the entire length of the gas targets. This work employs a Nomarski-type interferometer in the optical path of the probe imaging setup. In this type of interferometer, a Wollaston prism produces two orthogonally polarized copies of the probe image propagating under an angle. After some distance, both beams are transversely shifted such that the image of ionized and neutral parts of the gas target overlap. A polarizer, set at 45 degrees relative to both orthogonally polarized beams, projects them onto the same polarization direction, and their interference pattern is recorded with a camera (see Fig. 2.11a). The line-integrated optical thickness of the plasma can be deduced from the measured phase shift (see Fig. 2.11b). Note that both copies of the beam carry the phase information, visible as two regions of phase shift of opposite sign. By assuming rotational symmetry, the density distribution can be reconstructed using the Abel transformation (see Fig. 2.11c for lineouts along the laser axis and Appendix C.2 for a description of the nozzles creating these density profiles). The interferometrically reconstructed density aligns well with the density derived from the plasma wavelength from few-cycle shadowgraphy.

2.3.4 Down ramp generation in PWFA stage

Two mechanisms for density down ramp generation are implemented and interchangeable for the PWFA stage. The first implementation is a simple 200 µm-wide wire as an obstacle in the gas flow. The 4 cm long wire is tensioned between two holders. The longitudinal position of the shock depends on the wire position, which is adjusted with a motorized stage.

The second implementation is a density down ramp created by a laser pulse ionizing and heating the plasma locally. Subsequently, the generated plasma slab expands and constitutes density down ramps for injection. Figure 2.12 schematically shows this setup, which will be referred to as an optical injector in the following. For this setup, a small portion of the main laser beam is picked and individually delivered to the target. The energy of the injector beam can be adjusted between 0 and 50 mJ in a variable attenuator consisting of a half-wave plate in a rotational mount to set the beam polarization prior to a pair of thin film polarizers. With this combination, the energy of the optical injector can be continuously adjusted. The arrival time of the injector laser beam can be adjusted between 0 and 2 ns with a motorized delay stage.

The injector beam is perpendicularly focused onto the propagation axis of the electrons in the PWFA stage (see also Figure 2.8). The focusing optic is a 15 cm focal length spherical mirror used under an angle of incidence of approximately 15°. The resulting, strongly astigmatic intensity distribution in the plane of the electron beam is shown in inset (a) of Figure 2.12. Its peak intensity within the (10×330) µm^2 (FWHM) focal spot is 2×10^{16} W/cm^2. An intensity lineout along the axis of wakefield propagation (z) is given in inset (b). Assuming the Hydrogen to be ionized for a laser intensity $I_{laser} > 2 \times 10^{14} \frac{W}{cm^2}$ (blue line), the ionized region was roughly 100 µm wide.

Chapter 3.5 discusses the influence of the stability of both shocks on the witness spectra obtained in the PWFA.

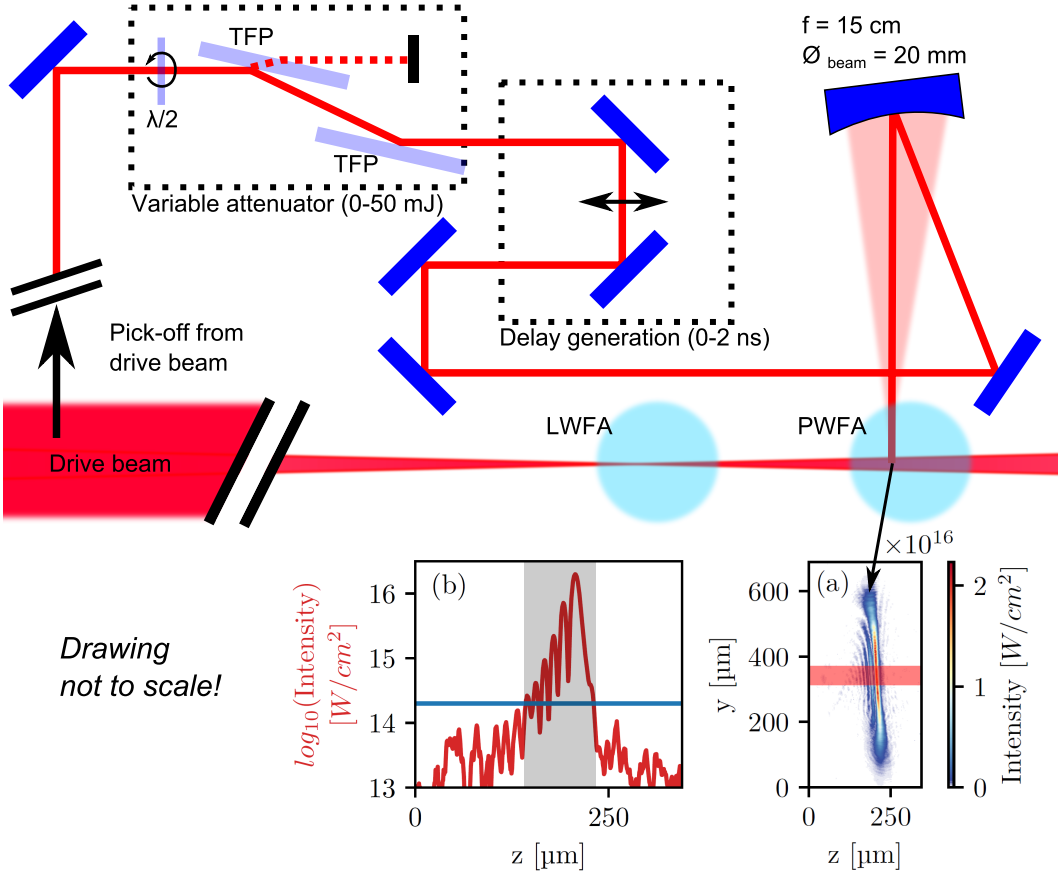

Figure 2.12: ***Schematic drawing of the injector beam setup.*** *The injector beam is picked from the main beam prior to focusing and final beam steering. The energy of the injector beam can be adjusted between* $0 - 50$ mJ *utilizing a rotating half-wave plate and a pair of thin film polarizers (TFP). The relative delay between the injector and driver can be varied between* $0 - 2$ ns *with a motorized delay stage. A spherical mirror used under an off-axis angle of* $15°$ *produces an astigmatic focus perpendicular to the wakefield axis in the PWFA. Inset (a) shows the spatial intensity distribution of the injector beam in the plane of the wakefield. Inset (b) shows a lineout of the beam intensity along the wakefield axis as indicated by the red-shaded area in (a). The threshold intensity for BSI in Hydrogen is indicated by the blue line in (b).*

2.4 Summary of experiments

2.4.1 High-charge LWFA

[3]As explained in the theory chapter, high-power lasers, and high-current electron bunches can drive strong wakefields suitable for electron acceleration. Consequently, in high-charge LWFA experiments, the laser driver and the injected electron bunch can

[3]This section summarizes the publication by Götzfried et al. [29]. The author of this thesis contributed the chapter on LWFA bunches with charge in excess of 1 nC and charge densities in excess of 20 pC/MeV obtained with the ATLAS3000 laser system operating at about 300-TW peak power.

significantly contribute to the wakefield formation. In [29], we studied the influence of high-charge electron bunches on the wakefields in an LWFA experiment. The beam loading effect on the electron spectra was demonstrated experimentally and in simulations. When the LWFA drive laser diffracts or depletes, we observed a transition into a regime with beam-dominated wakefield excitation. Therefore, this work bridged the gap in the description of laser- and beam-driven wakefield accelerators.

Beam loading

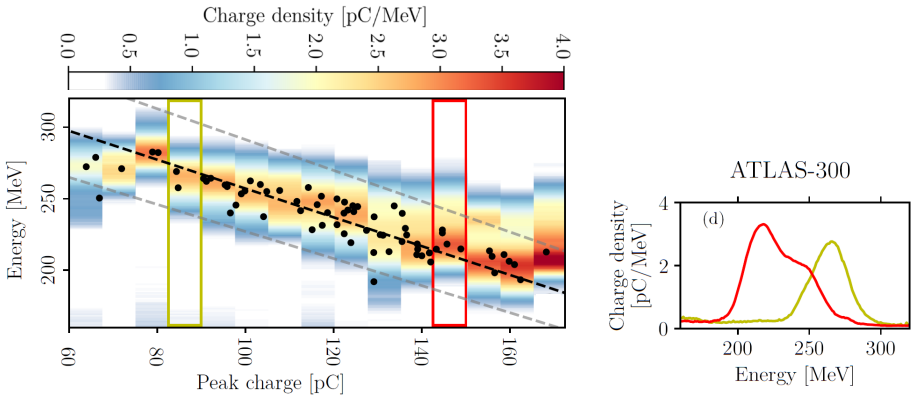

Figure 2.13: ***The effect of beam loading in an LWFA.*** *The left panel shows the spectra of LWFA-generated electron beams obtained with ATLAS300. The shots are sorted by charge. The right panel shows representative examples of a low-charge and a beam-loaded spectrum. Simplified reproduction of Fig. 3 of [29].*

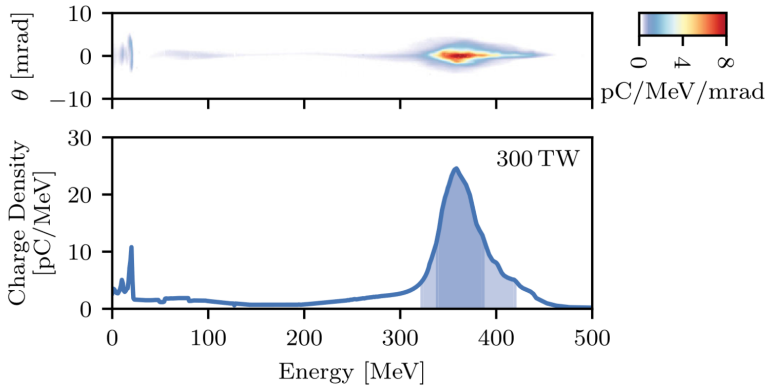

Figure 2.14: ***High-charge electron bunches from LWFA.*** *A high-charge shot from the commissioning experiments of the ATLAS3000 laser. Simplified reproduction of Fig. 6 of [29].*

Götzfried et al. investigated beam loading based on data from different laser systems. The beam-loaded regime of LWFA was identified from the spectral distribution of the generated electron bunches. First, and most notably, the electron energy decreased with increasing bunch charge under otherwise identical conditions (see Fig. 2.13

left). Secondly, beam loading also modified the spectral distribution of the electrons. Skewed electron spectra, with most charge at lower energies and a gradual fall-off to higher energies were observed (see Fig. 2.13 right). This skewness was attributed to the modification of the longitudinal wakefield structure by the high-charge electron bunch.

In the same publication, the author of this work contributed the first LWFA results from the ATLAS3000 laser (see Fig. 2.14). These LWFA-generated electron bunches were obtained at a laser power of approximately 300 TW and contained a charge of approximately 1 nC. These bunches also showed the characteristic skewness of the spectrum. For the LWFA-generated bunches in this work, the skewness due to beam loading is even better visible in Figure 5.6(a) (see page 85).

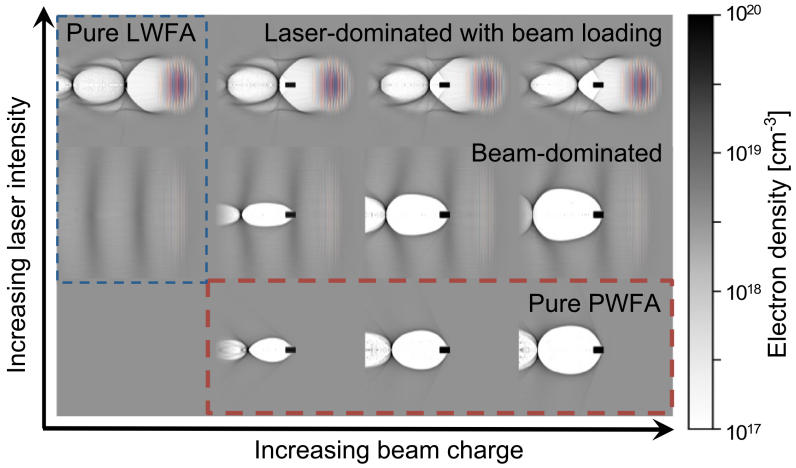

Figure 2.15: ***Different regimes of laser- and particle-driven wakefields.*** *PIC simulations of a 2D-parameter scan of laser intensity and particle-beam current. Simplified reproduction of Fig. 1 of [29].*

Transition from LWFA to PWFA

Götzfried et al. identify beam loading to be indicative of the ability of an electron bunch to drive wakefields on its own. Figure 2.15 shows the shape of the resulting wakefields for different combinations of laser intensity and particle beam current. Depending on their relative strength, different regimes of laser- and particle-driven wakefields can be identified. In the beam-loaded case (upper right edge in Fig. 2.15), the intense laser drives a strong wakefield, placing the electron bunch in the accelerating phase of its wakefield. The distortion of the sheath trajectories compared to the unloaded case (upper left edge in Fig. 2.15) is obvious. A lower-intensity laser can only drive a weak linear wakefield (middle row in Fig. 2.15). In this case, the wakefield dynamics are dominated by the electron bunch that expels all plasma electrons from the otherwise only weakly perturbed plasma (middle right in Fig. 2.15). If this regime change happens because the laser weakens due to diffraction or depletion in an LWFA experiment, it is called 'self-mode transition' [25, 98, 99]. The characteristics of the wakefield in this transition regime are very similar to the pure PWFA case (lower right edge in Fig. 2.15).

In hybrid L-PWFA a high-current electron bunch, capable of driving a subsequent PWFA, is generated via LWFA. This sequence is conceptually similar to self-mode-transition. However, in our experiment, the transition is not gradual but changes directly from beam-loaded LWFA to pure PWFA by introducing a vacuum gap between two separate plasma targets.

2.4.2 Summary of PWFA setups

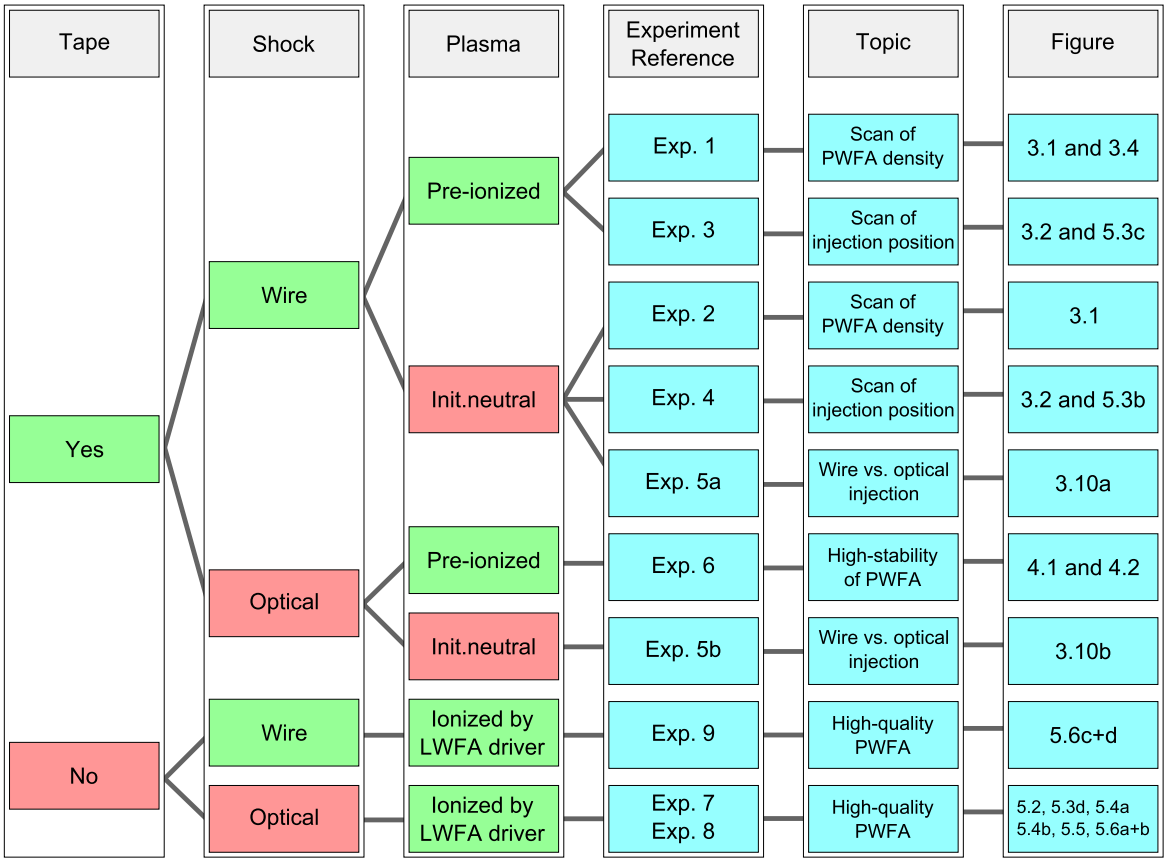

Figure 2.16: ***Summary of experimental conditions.*** *The experimental references assigned in this schematic will be used to identify the experiments in the results chapters.*

In the scope of this thesis, 8 different implementations of the PWFA experiment were realized to investigate different aspects of hybrid L-PWFA. The distinctive characteristics of the experiments are the use of a laser blocker tape, the mechanism for shock generation, and the ionization state of the gas target. The different setups are detailed in the chapters on the respective experiments. In addition, Figure 2.16 organizes all experiments visually according to these categories and relates the various implementations to the aspects of PWFA examined. For future reference, Figure 2.16 also assigns identifiers to all experiments. These identifiers are used in the results chapters to refer to specific experiments. Table 2.1 gives a detailed summary of all experiments' drive beam and target parameters.

Table 2.1: ***PWFA driver and target properties.*** *Summary of experimental conditions.*

Experiment	Exp.1	Exp.2	Exp.3	Exp.4	Exp.5
Figure	3.1 and 3.4	3.1	3.2 and 5.3(c)	3.2 and 5.3(b)	3.10
Driver charge	(390 ± 60) pC	(390 ± 60) pC	(390 ± 60) pC	(390 ± 60) pC	(430 ± 91) pC
Driver energy	(289 ± 20) MeV	(289 ± 20) MeV	(289 ± 20) MeV	(289 ± 20) MeV	(361 ± 25) MeV
Driver diverg. (FWHM, no blocker, no 2nd jet)	(2.6 ± 0.6) mrad	(2.6 ± 0.6) mrad	(2.6 ± 0.6) mrad	(2.6 ± 0.6) mrad	(2.9 ± 0.6) mrad
Gap between stages	1 cm	1 cm	1 cm	1 cm	1 cm
Nozzle PWFA	4 mm	4 mm	4 mm	4 mm	4 mm
Gas PWFA	H_2	H_2	H_2	H_2	96% H_2 + 4% N_2
Peak density PWFA	$(0 - 3.5)10^{18}$ cm^{-3}	$(0 - 3.5)10^{18}$ cm^{-3}	2.5×10^{18} cm^{-3}	2.5×10^{18} cm^{-3}	
Down ramp generation	wire	wire	wire	wire	compares both
Laser blocker tape	25 µm Kapton	25 µm Kapton	25 µm Kapton	25 µm Kapton	25 µm Kapton
Pre-ionizer	on	off	on	off	off

Experiment	Exp.6	Exp.7	Exp.8	Exp.9
Figure	4.1 and 4.2	5.2, 5.3(d) and 5.4(a)	5.4(b), 5.5 and 5.6(a+b)	5.6(c+d)
Driver charge	(340 ± 46) pC	(657 ± 61) pC	(657 ± 61) pC	(461 ± 99) pC
Driver energy	(287 ± 18) MeV	(235 ± 14) MeV	(235 ± 14) MeV	(284 ± 30) MeV
Driver diverg. (FWHM, no blocker, no 2nd jet)	(1.1 ± 0.2) mrad	(0.9 ± 0.1) mrad	(0.9 ± 0.1) mrad	(4.4 ± 0.5) mrad
Gap between stages	1 cm	1 cm	1.9 cm	1.25 cm
Nozzle PWFA	4 mm	7 mm	7 mm	4 mm
Gas PWFA	50% H_2 + 50% He	H_2	H_2	H_2
Density PWFA	$(2.0 \pm 0.2)10^{18}$ cm^{-3}	$(1.1 \pm 0.2))10^{18}$ cm^{-3}	$(1.1 \pm 0.2))10^{18}$ cm^{-3}	$(2.0 \pm 0.2)10^{18}$ cm^{-3}
Down ramp generation	optically	optically	optically	wire
Laser blocker tape	25 µm Kapton	no	no	no
Pre-ionizer	on	off	off	off

3 Controlled injection in an LWFA driven PWFA

In the early hybrid collaboration experiments [29, 40, 42, 43], density down ramp injection in a PWFA stage was a substantial challenge. In general, injection in PWFA is more complicated to achieve than injection in LWFA. This is due to the phase velocity of the wake – given by the drivers' group velocity – which is essentially c for highly relativistic electrons (as compared to $v_{g,\mathrm{laser}} < c$ in LWFA). Successfully injecting plasma electrons into the accelerating phase of the wakefield requires the electrons' longitudinal velocity to exceed the wake's phase velocity (Eq. 1.28). As the velocity of plasma electrons increases with driver strength, the experiment aims for high-current LWFA-generated drive beams. Furthermore, the reduction of the wake's phase velocity depends on the gradient of the density transition. Thus, the PWFA stage needs sharp down ramps for successful injection.

Conclusive experimental evidence for controlled internal injection in an LWFA-driven PWFA was obtained in parallel, but independent experiments at CALA and HZDR, starting from 2020. During these experiments, suitable conditions were achieved using LWFA electron bunches with several hundred pico-Coulomb of charge and density down ramps created by a wire in a supersonic gas jet. The HZDR data on internal injection was first published within the Hybrid collaboration by Couperus Cabadağ et al. [44]. Their publication focuses on the influence of PWFA density and injection position on the energy gain of the witness. This chapter validates these findings based on own data collected during the CALA-Hybrid campaign.

3.1 Experimental setup

The general setup and configurations for all experiments were introduced in Section 2.4.2. As in [44], the data is taken using a wire-generated hydrodynamic shock front for injection. In this experiment, the wire-generated shock is the method of choice due to its easier experimental implementation. The influence of replacing the wire-generated shock with an optically-generated shock is discussed later in Section 3.5 (*Optically-generated density down ramps*).

The LWFA-generated drive beams for the following two sets of experiments (referred to as Exp.1-Exp.4 in the methods Section 2.4.2) have an average charge of $(390 \pm 60)\,\mathrm{pC}$ (SD) and an average peak energy of (289 ± 20) MeV (SD). The plasma density and injection position scans are performed with the laser blocker tape in position between both accelerator stages. The laser blocker rules out any influence of the remaining drive laser from the LWFA on the wakefield formation in the PWFA. Thus, the energy loss of the drive beam in the PWFA stage can be attributed entirely to the effect of the self-driven wakefield.

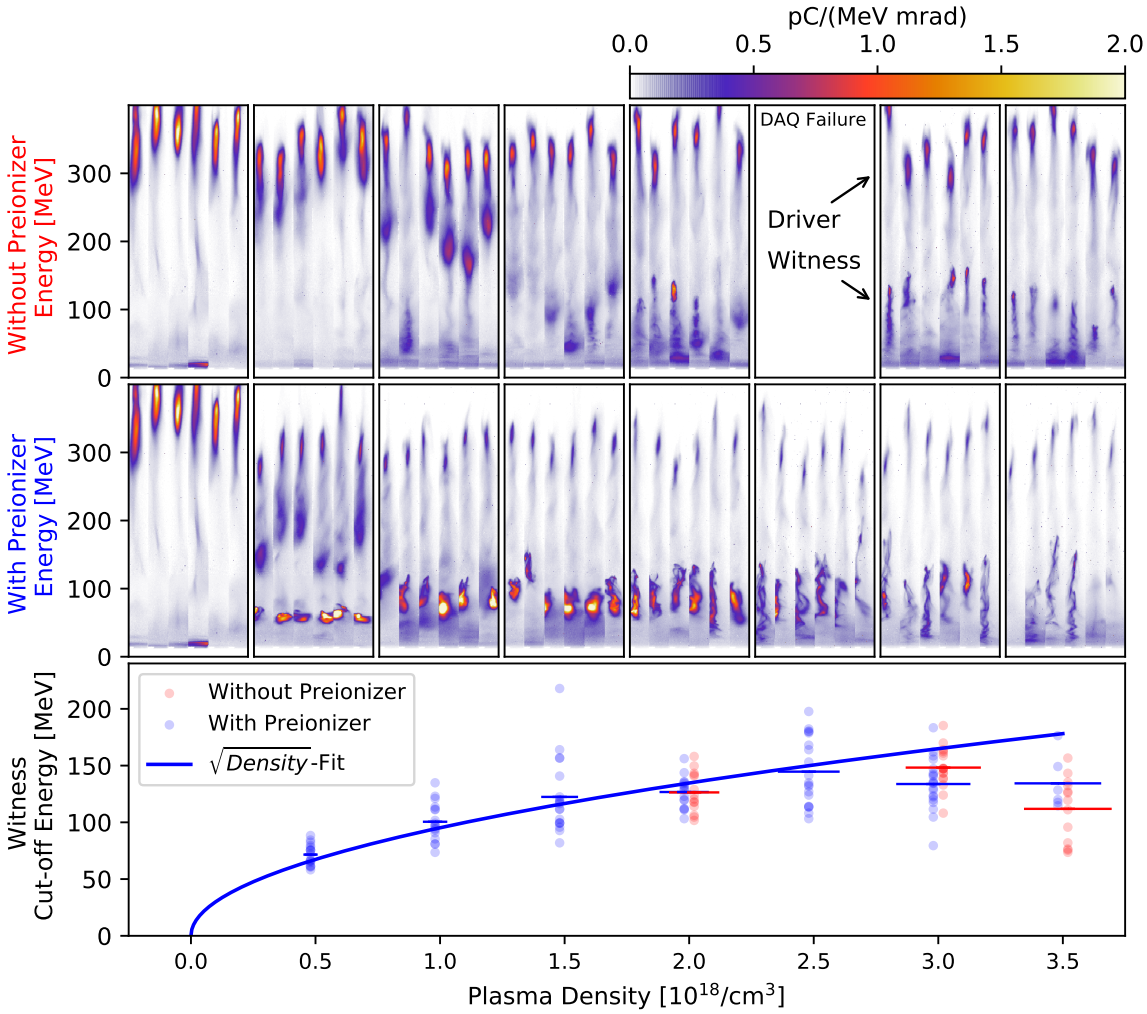

Figure 3.1: ***Scan of plasma density in the PWFA stage.*** *The witness energy varies as a function of the density in the PWFA stage. The top row shows data for an initially neutral gas (beam-self-ionized case) in the second stage. The middle row shows the case of a pre-ionized PWFA stage under otherwise identical conditions. The bottom row shows the maximum witness energy combined for both cases and a $\sqrt{Density}$-fit of the data with pre-ionization. The density in the PWFA stage is inferred from the measured backing pressure according to the relationship shown in Figure 2.11. Error bars in the x-direction indicate the uncertainty of this density calibration. Different data sets for nominally identical densities are plotted slightly shifted horizontally for better readability.*

3.2 Scan of plasma density in PWFA

In this set of experiments (referred to as Exp.1 and Exp.3 in the methods Section 2.4.2) we relate the deceleration of the driver and the gain of the witness energy to the density in the PWFA stage. The case of 0 density corresponds to the second jet being switched off (see first column of Figure 3.1). When the PWFA stage is switched on, the driver spends its energy driving a wakefield in the second stage. The beam-plasma interaction

strongly decelerated the driver bunch. The resulting spectra are qualitatively similar to the earlier description of collective deceleration by Chou et al. [40].

Deceleration of the driver

One significant feature of the decelerated driver spectra is that the peak of the spectral energy distribution at around 300 MeV barely depends on the plasma density. In an electron bunch of non-negligible length, some electrons will always be at positions with vanishing longitudinal wakefields, namely in the head of the beam, where the wakefield is not yet generated. Thus, the energy of these electrons is not affected by the PWFA stage.

The higher the plasma density is, the stronger the drivers' integrated energy loss gets. The reason for this energy loss is that a higher fraction of the driver charge is decelerated to lower energies. At a high enough density, a part of the driver is even entirely stopped and consequently lost. The deceleration can be seen particularly clearly in the top row of Figure 3.1. At densities between $(0 - 1.5)10^{18}$ $1/\mathrm{cm}^3$, the low-energy tail of the spent driver shifts towards lower energies and approaches zero energy.

In the case of a pre-ionized PWFA stage (see middle row of Figure 3.1), stronger wakefields build up [43, 65]. In turn, similar driver deceleration is observed at lower nominal density (lower neutral gas density) compared to the case of an initially neutral PWFA stage. As an example, a similar deceleration of the driver is observed for a nominal plasma density of $0.5 \times 10^{18}\,1/\mathrm{cm}^3$ in the pre-ionized case and for $1.5 \times 10^{18}\,1/\mathrm{cm}^3$ in the self-ionized case. In both cases, the low-energy tail of the spent driver spectrum approaches energies around 100 MeV.

For each PWFA plasma density under investigation, the remaining driver charge after the interaction in the PWFA is higher for the experiment without a pre-ionizer. Thus, effectively, less charge contributes to the wakefield formation, making the scheme with initially neutral gas less efficient. Also, no witness beam is injected at low densities, likely because it takes longer to build up strong wakefields. At high enough densities (here $> 2 \times 10^{18}\,1/\mathrm{cm}^3$), witness beams are reliably injected and reach similar energies as in the pre-ionized case. The effect of pre-ionization on the charge and divergence of the witness beams will be discussed in Section 5.2.1.

Acceleration of the witness

In the experiment with pre-ionized PWFA target, the witness energy increases with rising PWFA density. The witness energy gain scales approximately as the square root of the density. This scaling is a first-order approximation of the expected gain because it describes the maximum longitudinal wakefield as a function of density (Eq. 1.24). The increasing witness energy over a large range of densities indicates that depletion does not yet limit the energy gain of the witness. In other words, even with stronger wakefields at higher densities, the drive beam still has energy left to spend on driving the wakefield. However, the onset of driver depletion will eventually limit the gain in witness energy. Such an onset of driver depletion can explain the flattening of the gain

curve (see bottom row of Fig. 3.1) for densities of $> 2.5 \times 10^{18}\,1/\mathrm{cm}^3$. Also, the injection dynamics and, thus, the witness charge depend on the plasma density and will alter the scaling via beam loading. Beam loading will be analyzed using PIC simulations in Section 4.3.

The witness energy depends not only on the acceleration gradient but, as shown in the following, also on the length over which the electrons are accelerated at a given gradient.

3.3 Scan of injection position

A density down ramp offers the possibility of localized injection in the PWFA. As a result, for a given target length, the acceleration length can be precisely controlled utilizing the injection position of the witness. In the next set of experiments (referred to as Exp.2 and Exp.4 in the methods Section 2.4.2), we relate the energy gain of the witness to its injection position in the PWFA stage.

Effective acceleration gradient

The effective acceleration gradient is estimated using a linear fit to the dependence of the witness energy on the injection position. However, this analysis is a rough estimate as it neglects several effects. Firstly, the influence of the fluctuating witness charge is neglected. The witness charge changes with injection position, as it depends on the local gas density and wakefield strength. Secondly, the acceleration is not necessarily constant. In particular, a higher acceleration gradient is observed for positions further in the central part of the gas flow. That is, in areas of higher density in the nozzle. The linear fit neglects this longitudinally varying gradient. A piecewise analysis of the witness energy gain could map the acceleration gradient along the nozzle's longitudinal position. However, the statistical quality of the dataset does not allow a conclusive evaluation of these effects.

For the self-ionized case, the calculated accelerating gradient is 101 GV/m (with a 95%-confidence interval of [93;108]), as shown in the lower panel of Figure 3.2. For the pre-ionized case, this value increases to 157 GV/m; 95%-CI: [148;166]. This increased gradient can be attributed to the ambient conditions under which the wakefield is created. In the beam-self-ionized case, only a narrow plasma column with a diameter similar to the electron beam's transverse size of a few µm is formed [47, 65]. Some sheath electrons can escape into the surrounding neutral gas region and are not attracted back by the ion column. This smears out the bubble structure trailing the driver and weakens the field strength inside the wake. In the pre-ionized case, the diameter of the ionized region is much larger, close to the 100 µm-diameter of the ionizer pulse. This limits the escape possibilities of the sheath electrons and causes a higher wakefield amplitude. The stronger wakefields in the pre-ionized case also align with simulation results [44, 65]. This finding underlines the importance of using pre-ionized plasma targets to use the drivers' capability to drive strong wakefields.

The zero point of the x-axis in Figure 3.2 corresponds to the position from which

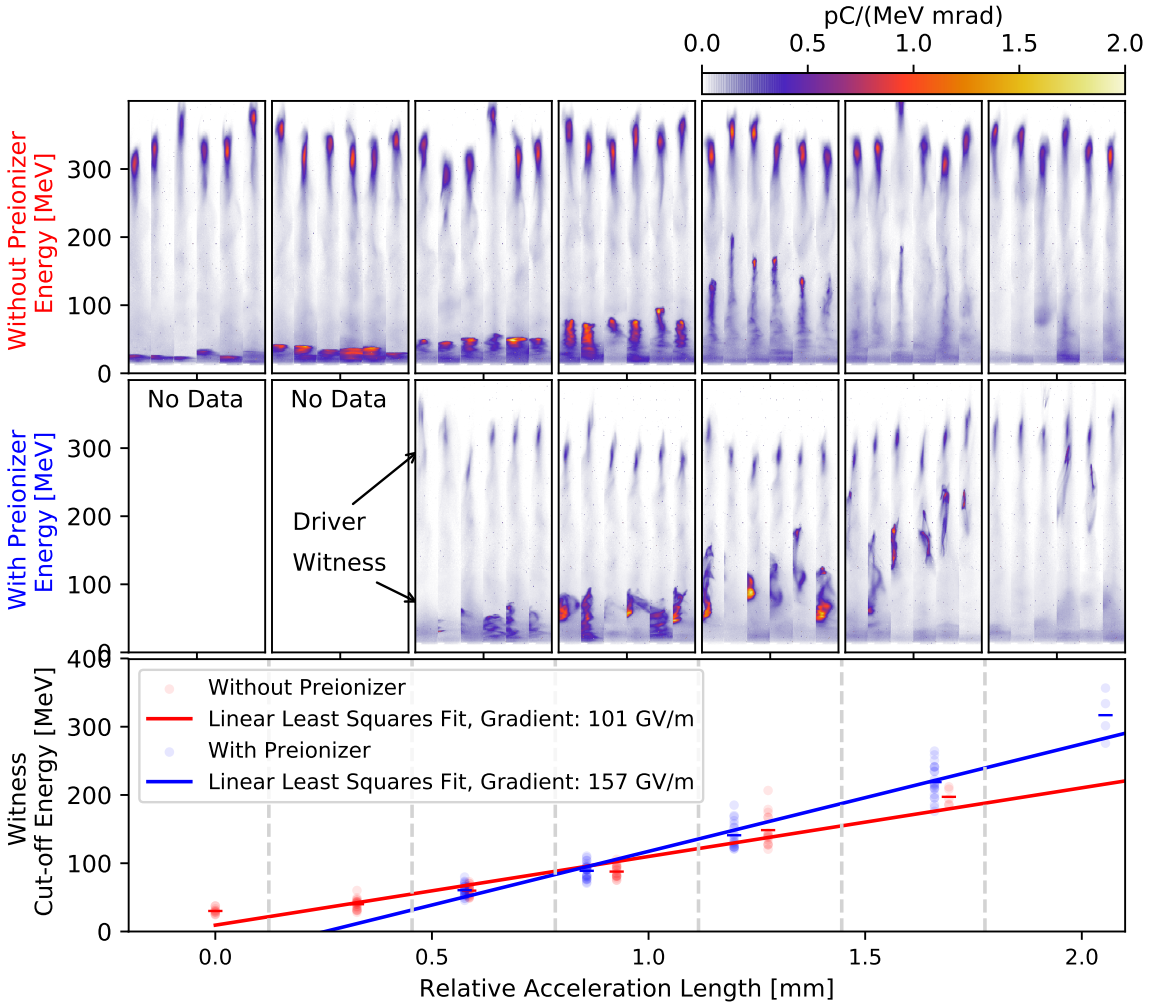

Figure 3.2: ***Scan of injection position in the PWFA stage.*** *The witness energy varies as a function of the injection position in the PWFA stage. The top row shows data for an initially neutral gas (beam-self-ionized case) in the second stage. The middle row shows the case of a pre-ionized PWFA stage under otherwise identical conditions. The bottom row shows the maximum witness energy for both cases and their respective linear least squares fit. During these scans, the peak plasma density was constant at* $2.5 \times 10^{18}\,1/\mathrm{cm}^3$*. The exact injection position for the data in the top two rows corresponds to the position of the data points between the respective gray dashed lines in the bottom row. The injection positions relative to the density profile of the target can be seen in Figure 3.3.*

no witness beam was produced. Figure 3.3 visualizes the definition of the zero point of the x-axis and the injection positions relative to the plasma density distribution retrieved from the experiment. The absence of a witness for injector positions beyond this point might be related to two effects. A witness injected in the down ramp of the gas target will gain very little energy as it continuously dephases due to the decreasing density. Furthermore, at decelerating gradients on the order of 100 MV/mm, the zero point of the x-axis also roughly corresponds to the point where depletion of the driver

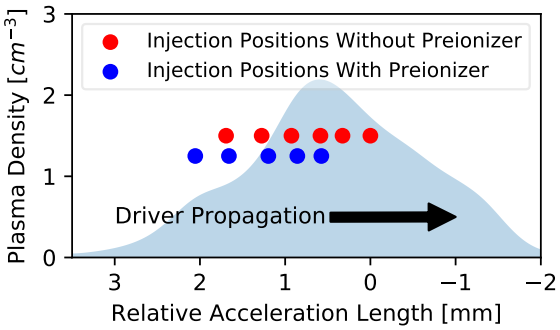

Figure 3.3: ***Definition of the injection position in the PWFA stage.*** *The injection position of the shots in Figure 3.2 is given relative to the unperturbed density distribution in the PWFA stage. The 0 position corresponds to the point after which no acceleration of the witness is observed.*

starts to be relevant.

In conclusion, the experiments show that controlled injection into an LWFA-driven PWFA is possible. Whether this Hybrid setup is also useful depends on several factors. On the one hand, a sufficiently high efficiency of the PWFA stage must be achieved, and on the other hand, gains in the quality of the electron beams (be it stability or charge density) must be shown. Both factors will be investigated in the following chapters.

TAKE-HOME MESSAGE

LWFA-generated electron bunches drive wakefields in the strong blowout regime in the PWFA stage. Witness bunches are internally injected in a controlled way at a density down ramp. The energy of these witness bunches can be adjusted by controlling the injection position and the plasma density in the PWFA.

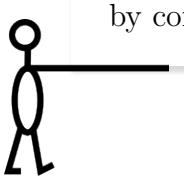

3.4 Energy transfer efficiency

No accelerator can reach a 100 % energy transfer efficiency. Thus, a staged hybrid accelerator scheme will always come with a penalty in overall efficiency. However, improvements in individual beam parameters, such as the energy stability or the bunch density, can outweigh this disadvantage. The following section estimates the overall energy transfer efficiency in a PWFA stage compared to previously published PWFA results.

Driver-to-witness or wake-to-witness efficiency

Two different parameters are commonly used in the literature to evaluate the energy transfer efficiency of a PWFA stage. The integrated energy gain of the PWFA wit-

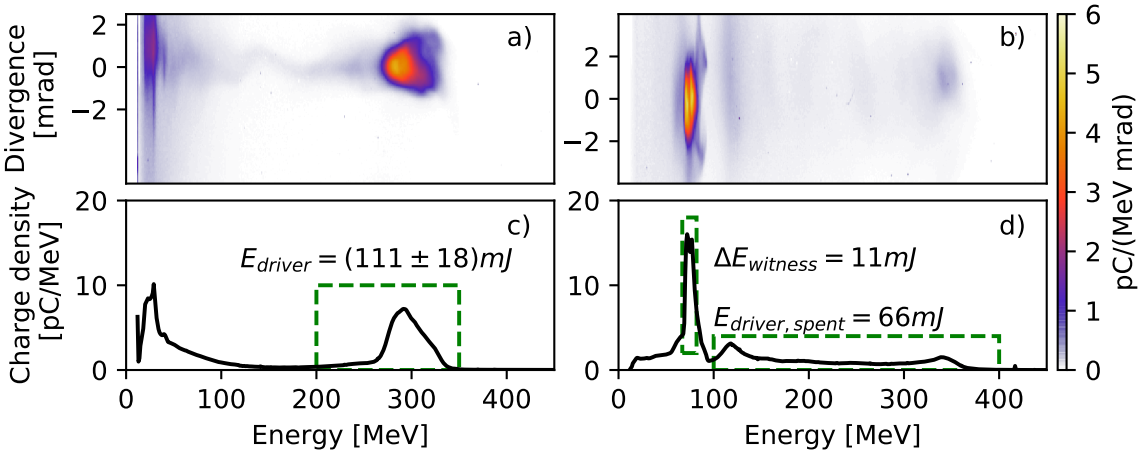

Figure 3.4: ***Example spectra of a staged LWFA PWFA experiment with 10% overall energy transfer efficiency.*** *(a) and (c) show a representative LWFA-generated drive bunch from a set with an average charge of* (390 ± 60) pC *and an average peak energy of* (289 ± 20) MeV. *The charge of the witness bunch shown in (b) and (d) is* 140 pC. *The dashed lines indicate the spectral features used to calculate the energy transfer efficiency.*

ness bunch ($\Delta\varepsilon_{\text{witness}} = Q_W \Delta E_W$) is compared to either the integrated energy of the incident LWFA-generated driver bunch ($\varepsilon_{\text{driver}} = Q_D E_D$) or to the driver's energy loss ($\Delta\varepsilon_{\text{driver}} = Q_D \Delta E_D$) instead

$$\eta = \frac{\Delta\varepsilon_{\text{witness}}}{\varepsilon_{\text{driver}}}, \tag{3.1}$$

$$\tilde{\eta} = \frac{\Delta\varepsilon_{\text{witness}}}{\Delta\varepsilon_{\text{driver}}}, \tag{3.2}$$

where εs are integrated bunch energies, Qs are charges, and Es are energies per electron. The calculated quantities η and $\tilde{\eta}$ differ greatly in some cases. Therefore, paying close attention to the respective definitions when comparing published figures is important. η can be understood as an *overall* energy transfer efficiency. It includes the whole energy of the driver and not only the energy loss due to the interaction in the PWFA stage. However, in published literature, the second version $\tilde{\eta}$ is often quoted (e.g. [34, 74]) as this definition yields higher efficiency figures even far from driver depletion.

It is clear that the energy transfer efficiency depends on the energy and the charge of the witness beam at the respective working point of each experiment. For reference, two experimental conditions from this study are analyzed and compared. In the first case, the witness charge was very high with 140 pC, and the peak energy was moderate at 75 MeV (see Fig. 3.4). In this experimental configuration, the energy transfer efficiency reached its highest values. For the data from Fig. 3.4, we find $\varepsilon_{\text{driver}} = (111 \pm 18)$ mJ (run average and SD) and $\Delta\varepsilon_{\text{witness}} = 11$mJ. These numbers yield an overall efficiency from incident driver to witness of

$$\eta = \frac{11\,\text{mJ}}{111\,\text{mJ}} = 10\%.$$

Table 3.1: ***Energy transfer efficiency in PWFA experiments.*** *Summary of published results on energy transfer efficiency in PWFA. Witness and driver charges are denoted by Q_W and Q_D. ΔE_W is the witness energy gain and E_D the initial driver energy.*

Publication	Driver	Inj.	η [%]	$\tilde{\eta}$ [%]	Q_W [pC]	ΔE_W [MeV]	Q_D [pC]	E_D [MeV]	$\frac{\Delta E_W}{E_D}$ [%]
This work (Fig. 3.4) [68]	LWFA	int.	10	24	150	80	390	290	28
This work (Fig. 5.4) [68]	LWFA	int.	3.1	4.4	30	162	630	250	65
Litos2014 [34]	conv.	ext.	0.6	24	74	1600	1020	20350	8
Litos2016 [100]	conv.	ext.	5.2		120	5300	600	20350	26
Lindstrom2021 [74]	conv.	ext.	0.9	42	100	45	500	1000	5
Knetsch2021 [91]	conv.	int.	0.2		33	45	790	1116	4
Ullmann2021 [92]	conv.	int.	0.6		500	780	3200	20000	4
Kurz2021 [43]	LWFA	ext.	2.9		12	66	104	260	25
Kurz2021 [43]	LWFA	ext.	1.2		25	14	119	244	6
Pompili2021 [101]	conv.	ext.	0.4		20	6.8	350	89.5	8

If applying the alternative definition, taking into account only the energy loss of the drive beam, the efficiency is

$$\tilde{\eta} = \frac{11\,\mathrm{mJ}}{(111-66)\mathrm{mJ}} = 24\%.$$

The efficiency was lower if the witness bunch is not optimized for high charge, but for beam quality as discussed in Section 5.4 (*Increasing angular spectral charge density*). Charge and energy of the beams from Figure 5.6(a)+(b) are summarized in Table 3.1. These numbers yield an overall efficiency of

$$\eta = \frac{5\,\mathrm{mJ}}{162\,\mathrm{mJ}} = 3.1\%,$$

or alternatively

$$\tilde{\eta} = \frac{5\,\mathrm{mJ}}{(162-48)\mathrm{mJ}} = 4.4\%.$$

Comparing the overall energy transfer efficiencies η from Table 3.1, the result of this work is at least a factor of 2 higher than shown in experiments with either external [34, 43, 74, 100, 101] or internal [91, 92] injection. To the author's knowledge, a value of $\eta = 10\%$ is the highest overall driver to witness energy transfer efficiency observed for any PWFA to date.

The values of $\tilde{\eta}$ reported in literature [34, 74] are higher but on the same order of magnitude compared to the highest values obtained in this work. The two cited experiments use a driver witness pair from a conventional accelerator. The two beams interact with the plasma in the PWFA over a length much shorter than the depletion length for the driver. Thus, they transfer a much lower fraction of the total drive beam energy (10 times smaller fraction than in this work). As a consequence, they also reach a ten times lower ratio of the witness's electron energy gain to driver electron energy ($\frac{\Delta E_W}{E_D}$).

The high degree of depletion in this work is facilitated by the combination of a high plasma density in the low $10^{18}\frac{1}{\mathrm{cm}^3}$ range and a moderate driver energy of a few 100 MeV. In contrast, PWFAs driven by conventional accelerators typically operate at much higher driver energies of many GeV. Moreover, they are typically limited to lower plasma densities n_e of the order of $10^{16}\frac{1}{\mathrm{cm}^3}$ to meet resonance conditions because of their longer bunches. As shown before, the wakefields scale approximately with $\sqrt{n_e}$. Consequently, at low densities, a much longer interaction length is needed to extract the driver energy efficiently.

TAKE-HOME MESSAGE

The overall energy transfer efficiency from LWFA- to PWFA-bunch reaches up to 10%. This value is among the highest efficiencies ever achieved in a PWFA.

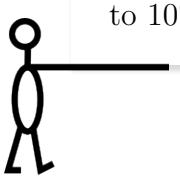

Some concluding remarks on efficiency

There will always be a trade-off between a high energy transfer efficiency and a high witness quality in a wakefield accelerator. This is because high energy extraction efficiency always comes with the penalty of high energy spread or low energy gain. The shadowgraphic probe images of the wakefield typically show more than ten oscillation periods behind the driver (see Figure 2.8). These long-lived wakefields indicate a poor energy extraction from the wakefield, which in turn oscillates until the energy is dissipated by other means. In contrast, it can be assumed that in the case of complete energy extraction, both the radius of the sheath trajectory and its slope would approach zero at the end of the bubble (as is the case at the front of the bubble). As a result, the longitudinal field would drop from some maximum value within the witness bunch to zero at its end. That is to say, the witness would be chirped with its energy decreasing to nearly zero at its tail.

The wire-generated down ramps presented in this chapter are easy to implement but have, at the same time, serious limitations. When using wire-generated shocks, one is limited to supersonic jets. While this might be an acceptable constraint, serious stability issues can arise as the properties of the down ramp are inherently coupled to the gas density distribution and flow of the jet (see Section 3.7).

3.5 Optically-generated density down ramps

This section introduces a purely optical method for generating density down ramps. This mechanism for down ramp generation relies on a laser pulse to ionize and heat the plasma locally. Subsequently, the generated plasma slab will expand on an ns-time scale and constitute density down ramps for injection. The setup of the optical injector and details on its timing, intensity, and shape have been presented in Figure 2.12. In

addition, Figure 3.5(a) shows a shadowgram of the shock structure overlaid with the intensity distribution of the injector beam.

3.5.1 Density reconstruction from shadowgraphic images.

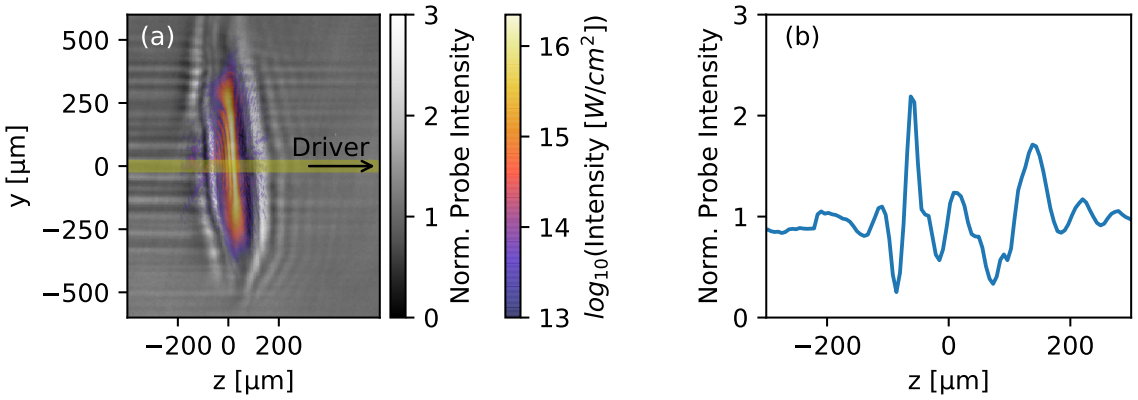

Figure 3.5: ***Shadowgraphic image of the optically-generated shockfront.*** *Panel (a) shows a shadowgraphic probe image of the optically-generated shock structure. The intensity distribution of the injector beam is overlaid in false colors. Panel (b) shows a lineout of the probe image along the drivers' propagation axis (yellow in (a)).*

The injector focus has a high aspect ratio of 330 µm : 10 µm. As seen in Figure 3.5(a), the resulting shock structure essentially consists of two plasma slabs moving away from each other. This geometry can be modeled as a 1D problem for the vicinity of the wakefield axis. Thus, only density variations along the wakefield propagation axis (z) must be considered.

Figure 3.5(b) shows an example of the shadowgraphic intensity variation along the wakefield axis. The visibility on the transverse probe relates to the plasma refractive index $\eta(y,z)$ and, in turn, to the plasma density distribution $n_p(y,z)$. The normalized intensity modulation $\frac{I(z)-I_0}{I_0}$ of the shadowgraphic probe image is given by [102, 103]:

$$\begin{aligned}\frac{I(z)-I_0}{I_0} &= -l \times \frac{d^2}{dz^2}\int_0^{\Delta y} \eta(y,z)dy \\ &= -l \times \frac{d^2}{dz^2}\int_0^{\Delta y} \sqrt{1-\frac{n_p(y,z)}{n_{crit}}}dy \\ &\approx -l \times \frac{d^2}{dz^2}\int_0^{\Delta y}\left(1-\frac{n_p(y,z)}{2n_{crit}}\right)dy = \frac{l}{2n_{crit}}\int_0^{\Delta y}\frac{d^2(n_p(y,z))}{dz^2}dy,\end{aligned} \tag{3.3}$$

where l is the distance from the source of the density modulation (or its image plane) to the detector. The integral goes to Δy, corresponding to the extent of the phase object along the line of sight.

According to Equation 3.3, the intensity distribution of a shadowgraphy image is proportional to the second derivative of the line-integrated refractive index or plasma

density distribution, respectively. In areas of constant density, no deviation of the beam is expected. A global linear plasma density gradient translates into the bending of the probe beam but no intensity variation. This behavior is similar to the effect of an infinitely wide wedge prism. Intensity fluctuations are expected when there is a non-vanishing second derivative of the transverse density distribution. Simply put, an inhomogeneous plasma can be viewed as a collection of focusing and defocusing lenses.

This analogy also already contains one of the main limitations of the model described by Equation 3.3. The derivation assumes a situation similar to a thin lens. This assumption implies that light rays bend by a slight angle in a defined plane. The image then consists of the superposition of these rays in some other defined plane at a large distance. The situation in the experiment does not meet those assumptions. The strong density variations around the shock translate into rapidly evolving, small-scale intensity variations. The formation length of these intensity variations is much shorter than the extent of the plasma density down ramp along the probes' line of sight. Furthermore, the imaging optics' depth of field is larger than the distance to the refracting object. A complete solution to the problem would include describing the probe propagation in terms of Fresnel–Kirchhoff diffraction, which is beyond the scope of this work. These limitations must be considered when interpreting the reconstructed density distribution according to Equation 3.3.

Modeling the density distribution

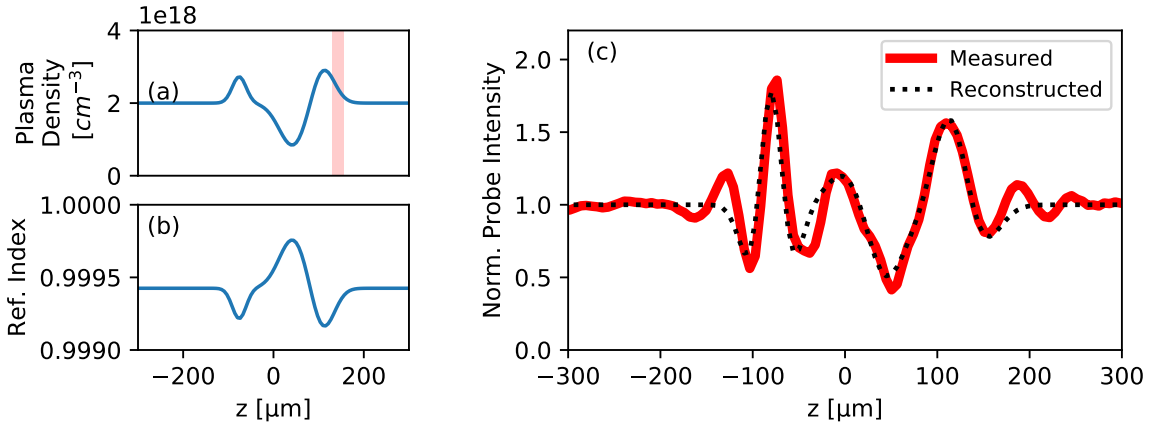

Figure 3.6: ***Reconstruction of the density profile for injection.*** *Panel (a) and (b) show the best guess density distribution and the respective plasma refractive index. The length of the down ramp is compared to the plasma wavelength (red-shaded). Panel (c) compares the measured shadowgram of the shock structure (red) with the one derived from the fitted density distribution (black dotted).*

Solving Equation 3.3 for n_p involves integrating the measured data twice. As a result, the solution is very susceptible to noise. To circumvent this problem, the shock structure was modeled by a superposition of the background density and three Gaussian functions with adjustable position, amplitude, and width:

$$n_p(z) = n_0 - a_{\text{dep.}}\exp\left(-\frac{(z-z_{\text{dep.}})^2}{w_{\text{dep.}}^2}\right) + a_{\text{l.p.}}\exp\left(-\frac{(z-z_{\text{l.p.}})^2}{w_{\text{l.p.}}^2}\right) + a_{\text{r.p.}}\exp\left(-\frac{(z-z_{\text{r.p.}})^2}{w_{\text{r.p.}}^2}\right), \tag{3.4}$$

where $n_0 = 2 \times 10^{18}\,\text{cm}^{-3}$ is the background plasma density. In this equation, a_x are amplitudes, w_x are widths, and z_x are positions of both peaks and the central density depression. From this plasma density, the plasma refractive index and the expected shadowgraphic image can be calculated analytically. a_x, w_x, and z_x are used as fitting parameters for the measured probe intensity distribution. In the fitting model, the width of the central density depression is chosen such that the particle number, according to the background density, is conserved.

Despite the very generic choice of the fitting model, it correctly reproduced the main features of the shadowgraphic image. Figure 3.6(a) shows one representative density distribution that optimized the fit of the probe intensity modulation shown in 3.6(c). The width of the reconstructed plasma density down ramps is on the order of the plasma wavelength (red shaded in 3.6(a)). This value can be considered an upper limit to the width of the actual density gradient, as different effects likely blur the measurement. According to the Rayleigh criterion, the resolution of the imaging setup (referred to here as the overview probe) is approximately $1.22\lambda(f/\#) = 1.22 \cdot 0.8\,\mu\text{m} \cdot 10 \approx 10\,\mu\text{m}$, which is on the order of the plasma wavelength itself. Furthermore, the sharpness of the gradient will be blurred by any non-collinear alignment of the injector and probe beam.

Note that the modulation depth of the density lineout in Figure 3.6(a) may have a large systematic error. According to Equation 3.3 the intensity modulation of the shadowgram is proportional to the product of observing distance l and the thickness Δy of the region ionized by the injector beam. In particular, l is not well defined as the image formation happens within the depth of field of the imaging setup of $200\,\mu\text{m}$. For the analysis, $l = 200\,\mu\text{m}$ and $\Delta y = 5\,\text{mm}$, corresponding to the width of the target, were set.

To see whether the height and steepness of the shock change noticeably with time after ionization, we recorded the shadowgrams at different delay times.

3.5.2 Expansion of the shock front

A shadowgraphic probe image of the density perturbation is recorded for different delays between the injector beam and the driver. Figure 3.7(a) shows the temporal evolution of the probe intensity in a slice around the wakefield axis. For this analysis, the position of the probe's intensity maxima is tracked. Their positions are indicated by the black dotted line in Figure 3.7(a). It is clearly visible that the double shock structure expands over time. Figure 3.7(b) shows the distance between the first and the second shock as a function of the injector delay. These points can be well fitted with a slope of $\sim 78\,\frac{\mu\text{m}}{\text{ns}}$; 95%-CI: [67;88]. The interception with the y-axis at zero delays

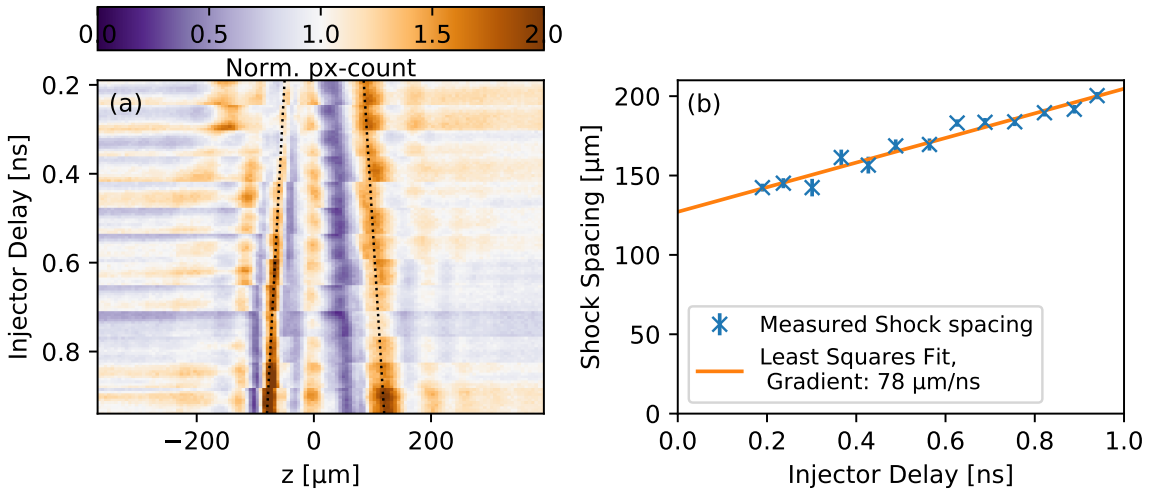

Figure 3.7: ***Expansion of optically-generated shockfront.*** *(a) shows the measured probe intensity around the down ramp as a function of the delay between the injector and driver. Black dotted lines indicate the location of both density spikes. (b) shows the distance between both shocks as a function of the injector delay and a linear least squares fit of the data.*

at 127 μm corresponds to the width of the initially ionized volume. The measured propagation velocity of $\frac{78\,\mu\text{m/ns}}{2} = 39\,\mu\text{m/ns}$ can be identified as the ions' speed of sound and implies a plasma temperature of $k_b T_e = c_s^2 m_i / Z = (39\,\mu\text{m/ns})^2\, 1.7 \times 10^{-27}\,\text{kg} \overset{\wedge}{\approx} 16\,\text{eV}$ (see Equation 1.29).

3.5.3 Temporal evolution of the density down ramp

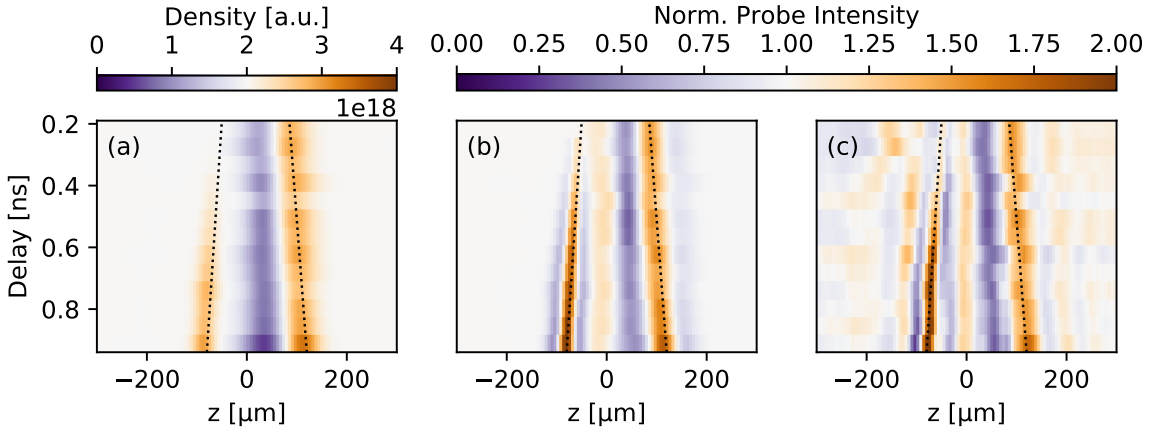

Figure 3.8: ***Temporal evolution of the density profile for injection.*** *(a) shows the best guess density distribution as a function of injector delay. (b) and (c) are the reconstructed and measured shadowgraphic probe images as a function of injector delay.*

For each delay between the injector beam and the driver, the measured probe in-

tensity along a longitudinal slice (compare Fig. 3.5) is fitted according to the model introduced above. Figure 3.8(a) shows the evolution of the reconstructed density distribution as a function of the injector delay. With increasing delay, the modulation becomes stronger. In particular, the central density depression deepens, and the left-going (upstream) density spike becomes higher. In contrast, the height of the right-going (downstream) density spike seems to be largely independent of the timing.

3.6 Injecting at an optically-triggered down ramp: Timing scan

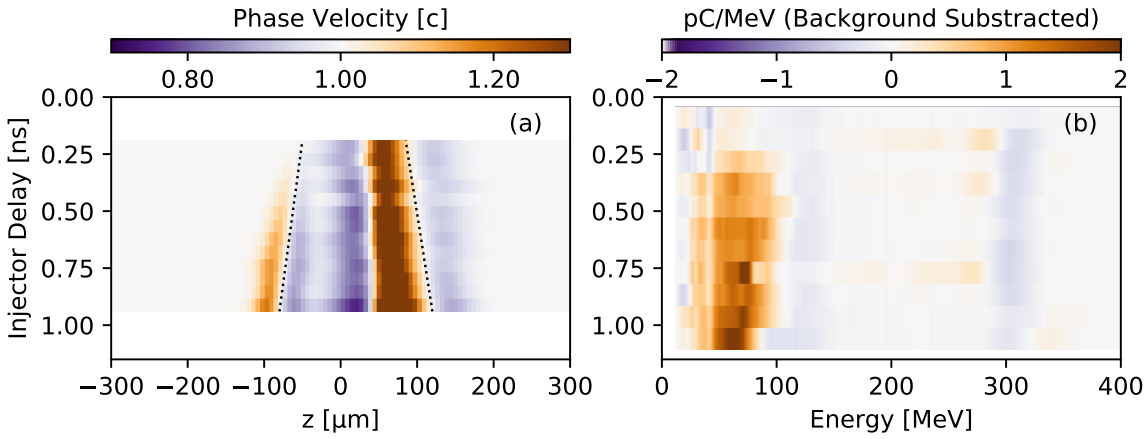

Figure 3.9: ***Wakefield phase velocity and witness spectrum as a function of injector beam delay.*** *(a) shows the phase velocity variation at the bubble's end. The phase velocity is given across the injection region as a function of the injector delay. The black dotted line corresponds to the position of the density spikes as in the previous figure. (b) shows spectra after the PWFA as a function of the injector delay. For this plot, spectra are binned according to the chosen injector beam delay in steps of 100 ps. A reference spectrum without an injector beam was subtracted.*

Based on the reconstructed density distribution n, the normalized phase velocity β_p at the back of the first wakefield period can be calculated as a function of position and injector timing (Equation 1.28 in Section 1.4.1):

$$\beta_p = \frac{\beta_b}{1 + \frac{\chi}{k_{p,0}} \frac{1}{2n} \frac{dn}{dz}}, \tag{3.5}$$

where $\beta_b \approx 1$ is the phase velocity of the driver and $-\frac{\chi}{k_{p,0}} \overset{\text{at } \chi=-2\pi}{=} \lambda_p$ corresponds to the plasma wavelength at the background density. Figure 3.9(a) shows β_p around the density perturbation as a function of the injector beam timing. The lowest values (darkest blue), and therefore the highest chance for injection, are obtained for the largest delay of the injector beam.

To relate the properties of the density down ramp to the actual injection, also the witness spectra are shown as a function of the injector beam timing (Figure 3.9b). For this plot, spectra are binned according to the chosen injector beam delay in steps of 100 ps. A reference spectrum without an injector beam is subtracted from all spectra. By that, the decelerated driver charge is, up to shot-to-shot fluctuations, removed from the spectra. For a delay of 300 ps and longer, a witness bunch is injected and accelerated to $50 - 100$ MeV. For longer delays, more witness charge is injected and, in turn, accelerated to lower energies. This enhanced injection is consistent with the previously described steepening of the down ramp with increasing delay.

As the optical injection scheme produces two shocks, there are two down ramps for injection. From the spectra, it can not be seen at which the witness beam has been injected. Interestingly, the lowest phase velocity at the back of the bubble is obtained in the down ramp of the upstream shock (between -100 and $-50\,\mu$m in Fig. 3.9(a)). Thus, injection in this region should be favored. However, it is not clear if such a witness would survive the up ramp section between +50 and $100\,\mu$m in Fig. 3.9(a), where it likely slips out of the accelerating phase of the first bubble. Previous studies indicate that only the second down ramp in a double shock significantly contributes to the witness charge [44]. However, a more detailed study of the injection dynamics at a complex density distribution should be part of future simulation campaigns.

In conclusion, the optically triggered injection method adds more experimental degrees of freedom. The timing of the injector beam determines the steepness of the density down ramp, and, in turn, the injected charge. This control of the witness charge can be useful to exploit beam loading in the PWFA (see Section 4.3). Furthermore, the following section proves that the optical injection scheme can also be beneficial in terms of the stability of the generated witness beams.

3.7 Wire- vs. optically-generated density down-ramps

The wire-generated shock and the optically-generated one are interchangeable for this set of experiments (referred to as Exp.5a and Exp.5b in the methods Section 2.4.2). Experiments are performed using both mechanisms under otherwise identical conditions.

The position of the optically-generated shock is much more stable than that of the wire-generated one, as seen in Figure 3.10. By not relying on the vibration stability of the wire and the hydrodynamics of the gas flow, there are fewer degrees of freedom for variations of the density down ramp. As verified via shadowgraphy, the position of the wire-generated shock varies by 47 µm (SD). In contrast, the position of the optically-generated shock fluctuates by less than the camera resolution of 10 µm (SD). In the latter case, based on the previously established accelerating gradients of up to 150 MeV/mm, the influence of the injection position on the measured energy fluctuations is negligibly small.

Both injection mechanisms generate witness beams with peak energies in the range

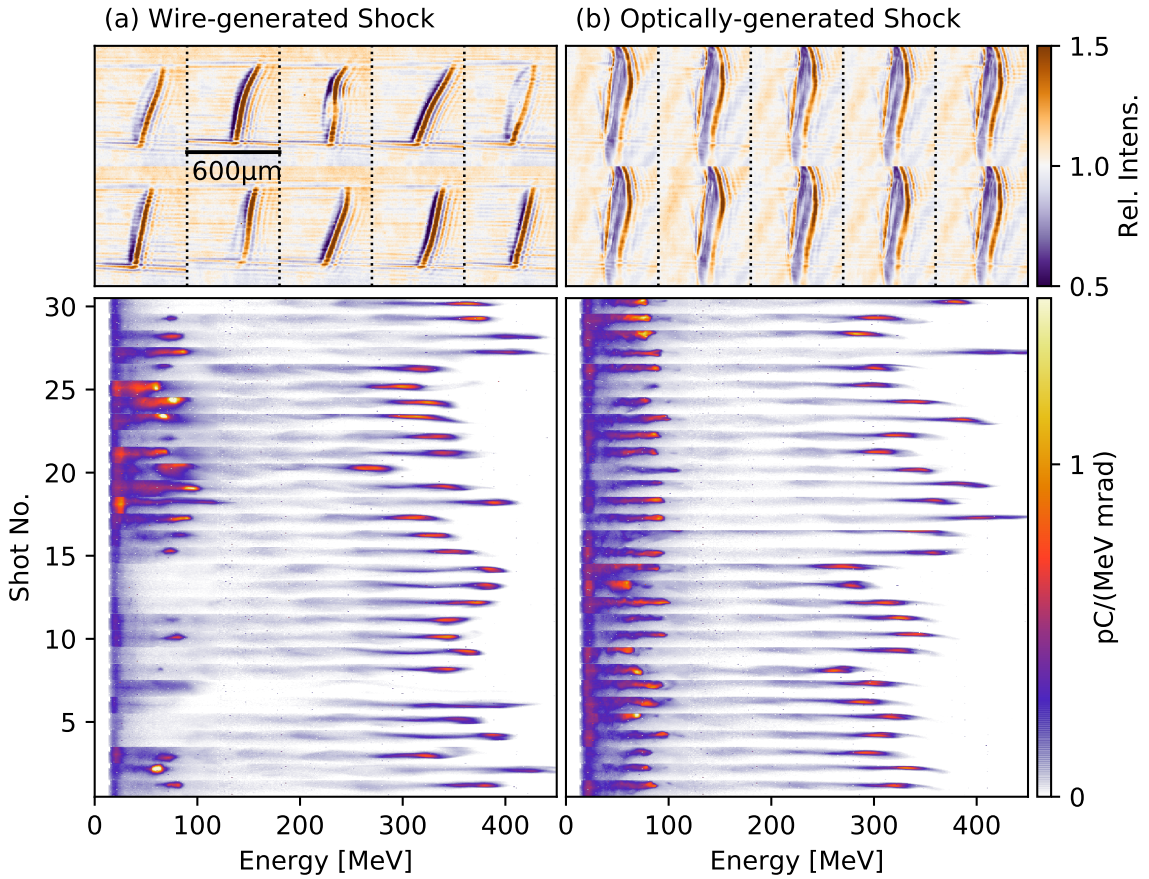

Figure 3.10: ***Comparison of the injection at a wire- and at an optically-generated density down ramp in the PWFA stage.*** *The two panels show sets of shadowgrams along with 30 consecutive shots for each of the two mechanisms for down ramp generation. Both mechanisms generate witness beams with peak energies in the range of* $(70-110)$ MeV*. While in the wire-shock case, a particularly high charge is injected on some shots, the optically-generated shock leads to higher stability of both energy and charge of the witness beam. Position, shape, and gradient vary stronger in the case of the wire-generated shock.*

of $(70-110)$ MeV, as seen in the lower panel of Figure 3.10. The optically-generated shock leads to the injection of a witness in 100% of the shots in this set. It is, therefore, more reliable than the wire-generated shock ($\sim$ 70%). The stability of the witness energy is higher with the optically-generated shock. The witness cut-off energy in this set is (92 ± 8) MeV (9% SD) as compared to (88 ± 15) MeV (17% SD) for the wire generated shock.

As seen in the upper panel of Figure 3.10, not only the position and shape but also the contrast of the shadowgrams fluctuates much more in the wire shock case. These variations of the down ramp can explain the strong shot-to-shot fluctuations in injected charge for the wire case [69, 104, 105]. The influence of shot-to-shot variations of the witness charge is discussed quantitatively later in Section 4.3 (*Witness energy in PIC simulations*).

Unless otherwise stated, the setup with an optically-generated density down ramp is used for the rest of the experiments presented in this work.

3.8 Summary and significance

The central result of this chapter is the controlled internal injection of witness bunches at a down ramp in a PWFA. The energy of the witness can be controlled by the plasma density and the acceleration length. The measured acceleration gradient is up to 157 GV/m at a plasma density of $2.5 \times 10^{18} \frac{1}{\mathrm{cm}^3}$. This experiment achieves a high degree of depletion, making the method efficient at maximum values of $\eta = 10\%$. The combined laser-to-driver and driver-to-witness efficiency can be greater than 1%. The efficiency estimate is based on the results of this work and on the energy transfer efficiency from the laser to LWFA electrons of up to 10% [29]. Furthermore, a much higher fraction of the driver energy is transferred to the witness than previously shown for PWFAs driven by rf-machines. Since the physics of the PWFA scales with the plasma density, the high-depletion operating mode can serve to investigate future modes of operation of larger low-density systems.

In addition to the wire-generated shock, an optically-triggered density down ramp is implemented for injection in PWFA. Utilizing the delay between the injector laser and the driver, the steepness of the density down ramp and the injected charge can be controlled. Furthermore, the optically-generated shock is more stable and injects witness beams more reliably than the previously used wire-generated shock. The achieved reproducibility and control over the injection process is a prerequisite for optimizing the witness beams in terms of stability (Chapter 4: *Stability of staged L-PWFA*), divergence, and spectral width (Chapter 5: *High quality witness bunches*).

4 Stability of staged L-PWFA

The control over the injection process established in the previous chapter enables targeted experiments to optimize specific witness beam parameters. This section investigates and evaluates the experimentally achieved energy stability of the witness beam using an optical injector. PIC simulations underline the importance of beam loading for stabilizing the witness energy in a PWFA.

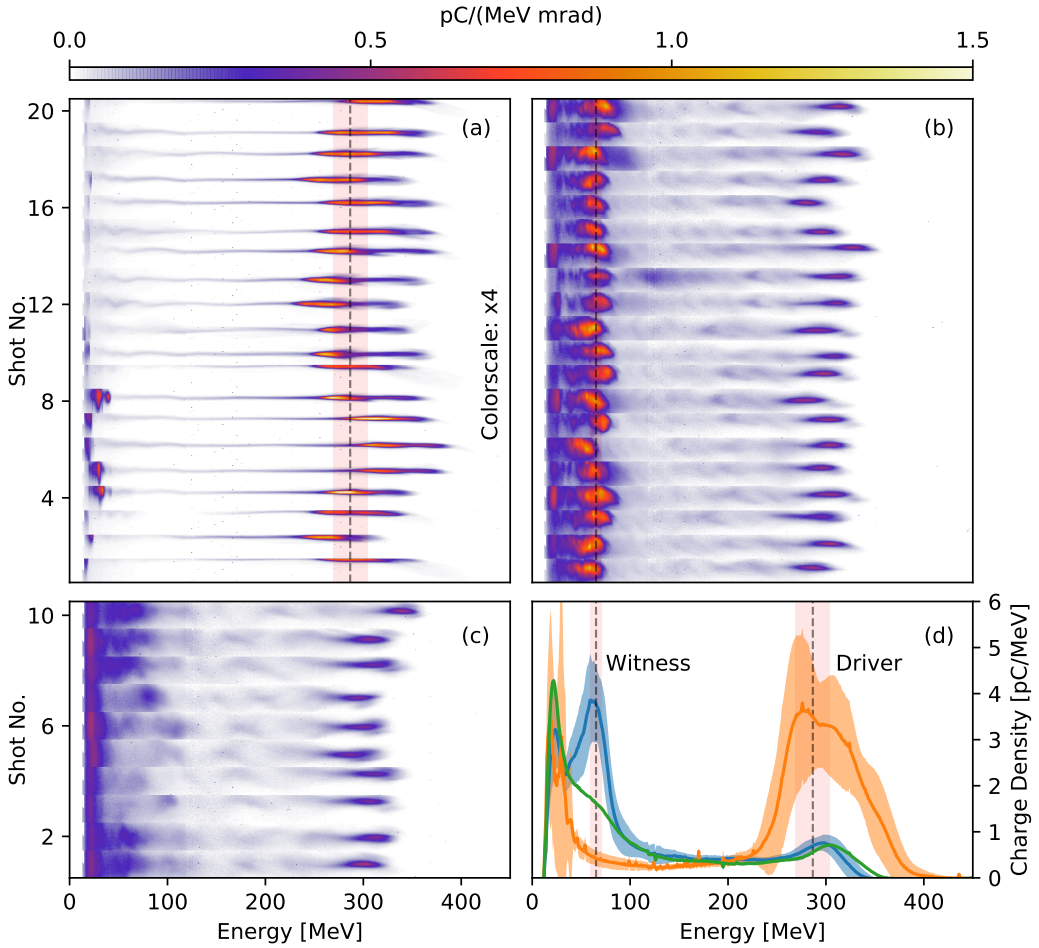

Figure 4.1: ***Comparison of driver and witness stability.*** *(a) Set of 20 driver reference shots. (b) Another set of 20 consecutive shots shows the high stability of the internally injected witness beam. For comparison, panel (c) shows only the decelerated driver in a run without a down ramp for injection in the PWFA. The spectrum of the driver (orange), witness (blue), and the case without injection (green), together with their respective standard deviations, are plotted in (d). The dashed lines and the red shaded areas indicate the mean and standard deviation of the driver and witness energy. Please note that the scale on the color bar has to be multiplied by a factor of 4 in panel (a).*

4.1 Experimental setup

The general setup and configurations for all experiments are introduced in Section 2.4.2. To convert the theoretically predicted high stability of the wakefields (Section 1.3.3) into stable witness energy, a localized and stable injection is necessary. For this reason, the optically-generated shock and a pre-ionized plasma are used for the following experiments (referred to as Exp.6 in the methods Section 2.4.2). The optically-generated shock decouples the injection position from the mechanical and hydrodynamic stability of the gas target. This highly stable injection scheme is an important prerequisite for generating witness beams with higher stability than the drive beam itself.

In this experiment, the LWFA-generated driver has a peak energy of (287±18) MeV (6%, SD). The integrated charge of all electrons with an energy above 200 MeV is (340 ± 46) pC (14%, SD). For details of the driver, see the reference set of 20 LWFA-only shots in Fig 4.1(a).

4.2 Stability of witness energy in experiments

Energy stability[1]

As in the previously described experiments, the LWFA-generated electrons are decelerated during their interaction with the plasma in the PWFA stage. Shots without injector in the PWFA, showing a broadband background of decelerated driver charge, can be found in Fig. 4.1c. When the optical injector is switched on, witness beams are reliably injected and clearly visible on top of the decelerated driver charge (Fig. 4.1b and lineout in panel c). The witness peak energy is (65 ± 6) MeV (9%, SD). Its absolute fluctuation (red shaded area in Fig. 4.1d) is only one-third of the drivers. Their relative energy jitter is of the same order as the drivers.

The simplified analytical model derived before (Eq. 1.25) relates the witness energy to the driver current and the plasma density. From the square-root scaling ($E_z^{max} \propto -\sqrt{I_0 n_0}$), the expected relative deviation of the longitudinal electric field is about half of the relative deviation of both drive beam current and plasma density. Assuming that the drive bunch length is constant, the charge of the drive beam is proportional to its current. Consequently, 14% variation of driver charge should translate into 7% fluctuation of E_z. Furthermore, 4% (SD) density jitter due to an imperfect regulation of the backing pressure for the PWFA stage should lead to another 2% variation of E_z. For both errors being independent and normally distributed, this accounts for an energy jitter of 5 MeV due to driver and density fluctuations in this experiment. Hence, the prediction of the simplified model is consistent with the measured energy of (65 ± 6)MeV.

The ratio of relative fluctuations in witness energy $\delta E_{\text{witness}}$ and driver charge δQ_{driver} is a practical measure of the susceptibility of the PWFA stage to fluctuations of the driver. The measured value of $|\delta E_{\text{witness}}[\%]| \leq 0.68\,|\delta Q_{\text{driver}}[\%]|$ is smaller

[1] This section closely follows section III of the authors' publication: Foerster et al. PRX (2022) [68].

than 1 and therefore indicates a damping behaviour[2]. Section 4.3 (*Witness energy in PIC simulations*) provides a more detailed discussion of the expected energy stability based on simulations modeling this experiment. Furthermore, these simulations give insight into beam loading effects due to the witness charge that is (59 ± 19) pC (SD) in this experiment.

TAKE-HOME MESSAGE

Using a stable, optically-triggered injection scheme, the experimentally measured energy stability in the PWFA approaches the theoretically predicted, high value and is comparable to pure LWFA.

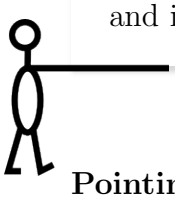

Pointing stability

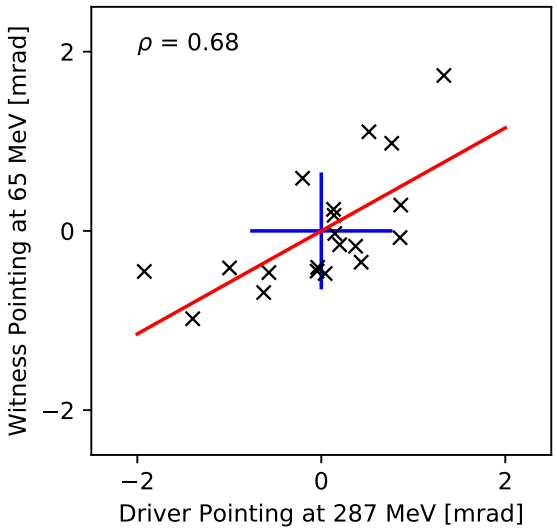

Figure 4.2: ***Pointing of driver and witness beam.*** *The pointing of both beams at their respective mean energies is correlated with a Pearson correlation coefficient of 0.68. The standard deviations of the pointing of driver (*0.8 mrad*) and witness (*0.7 mrad*) are marked as blue lines. The data is taken from the set presented in Fig. 4.1(b).*

The experimental data shows a clear correlation between driver and witness pointing. The pointing of both species in the shots from Fig. 4.1(b) at their respective mean energies correlates with a Pearson correlation coefficient of 0.68 (1: perfect linear correlation, 0: uncorrelated, -1: perfectly anti-correlated). No matter in which direction the electron beam from the LWFA stage points (assuming typical experimental jitters of a few Millirad), the witness will be injected and accelerated in its wake. The average of the pointing difference between the driver and witness beam amounts to 0.02 mrad

[2]Please note that this number includes all contributions to the variation of witness energy. The '=' sign would apply if the variation in witness energy is only due to charge variations of the driver.

only. Also, the standard deviation of the witness pointing (0.7 mrad) is even smaller than the one of the driver (0.8 mrad). In Fig. 4.2, these results are presented. Given these numbers, it is not expected that staged L-PWFA adds any pointing-related issues for potential applications.

4.3 Witness energy in PIC simulations

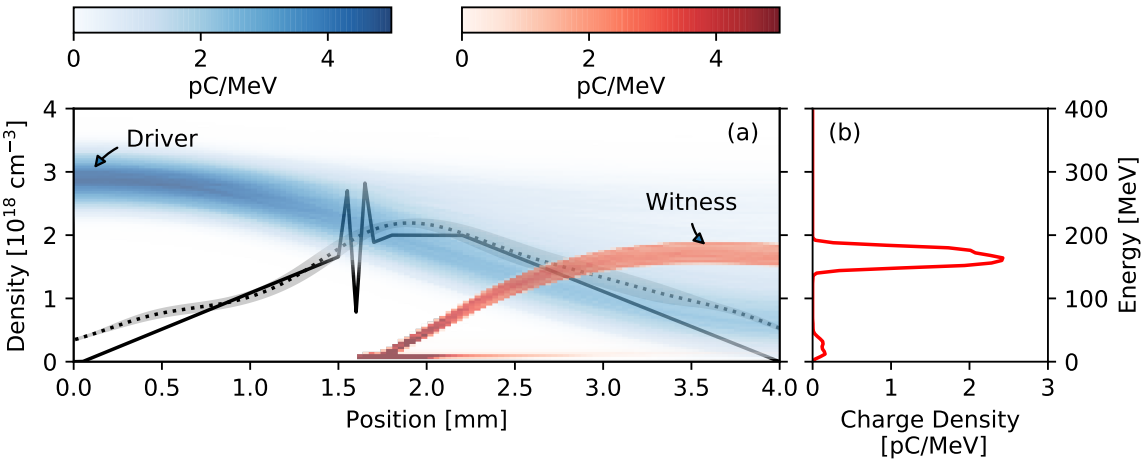

Figure 4.3: ***Overview PIC simulations.*** *The simulated density profile (solid black) is a simplified model of the measured plasma density profile (dotted black, without down ramp for injection) of the 4 mm wide nozzle at a peak plasma density of* $2 \times 10^{18}\,1/\mathrm{cm}^3$*. Panel (a) also visualizes the evolution of the driver (blue) and the witness spectrum (red) over the length of the target. (b) shows the spectrum of the witness beam at the end of the simulation.*

[3]A set of 100 PIC simulations models the previously described experiment and its driver charge and energy variations (see Table 4.1). Additional sets of PIC simulations – scanning driver charge and energy independently and in a large range – provide further insight into the wakefield generation and witness acceleration in the PWFA. A last set of simulations investigates the influence of the driver emittance on the witness beam properties. In PIC simulations, these parameter scans can be carried out in a more controlled manner and in a range that was not feasible in the experiment.

The simulated density profile models the 4-mm-wide nozzle used in the previously described experiment (presented in Fig. 4.1) in terms of length and its maximum plasma density of $2 \times 10^{18}\,1/\mathrm{cm}^3$, including its long and gentle density up and down ramp. The position of the density transition for injection is chosen according to the experiment. The plasma distribution and the exact height and gradient of the shock, however, may differ from the experiment as the shock and the density distribution in low-density parts of the nozzle were not resolved in our diagnostic. Figure 4.3 shows the simulated density profile together with the evolution of the driver and the witness

[3]This section closely follows section III and the supplemental material of the authors' publication: Foerster et al. PRX (2022) [68].

Table 4.1: ***PIC Simulations of PWFA Stage.*** *Summary of drive beam parameters for all sets of PIC simulations.*

Set	Rand. Fluct.	Energy Scan	Charge Scan	Emittance Scan
Figure	4.5	4.4	4.8	4.10
No. of Sims.	100	100	50	40
Driver energy	(287 ± 18) MeV	$(0.5 - 8) \times 287$ MeV	287 MeV	287 MeV
Energy spread	29 MeV	$(0.5 - 8) \times 29$ MeV	29 MeV	29 MeV
Driver charge	(340 ± 46) pC	340 pC	$(240 - 440)$ pC	340 pC
Driver emit.	1 µm	1 µm	1 µm	$(0.1 - 20)$ µm

spectrum for the reference case of a 340 pC, 287 MeV, and 10% energy spread drive beam. The driver's energy loss while propagating through the plasma and the injection of a witness beam at the density transition and its subsequent acceleration are evident.

Table 4.1 summarizes the driver parameters for all sets of PIC simulations. A complete overview of the input parameters of all simulations is given in Appendix A.

4.3.1 Scan of driver energy

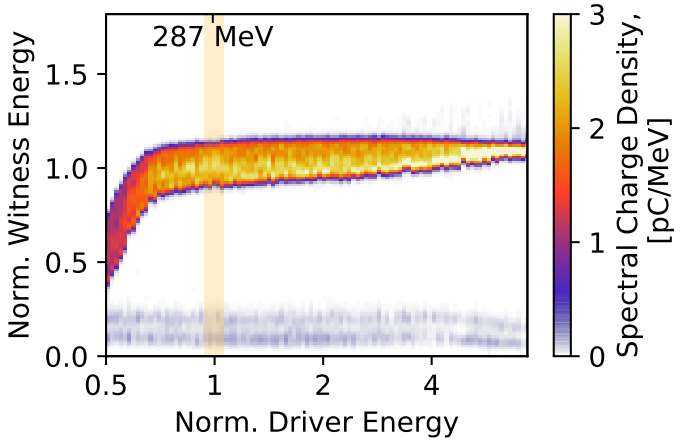

Figure 4.4: ***Scan of driver energy in PIC simulations.*** *The witness spectrum is plotted as a function of the driver energy at a constant driver charge of* 340 pC*. The driver energy is varied between 0.5 and 8 times the experimental value of* 287 MeV*. Please note the logarithmic x-axis.*

The first set of 100 simulations varies the driver energy between half and eight times the experimental value of 287 MeV while keeping the driver charge constant at 340 pC. As expected from the theoretical model [Section 1.3.3], the witness energy barely depends on the driver energy over a broad energy range. This range by far exceeds the measured energy fluctuations in the experiment (shaded orange in Fig. 4.4). Only below a certain energy level, which is on the order of 200 MeV for the target length and density in the simulations, does depletion of the driver become influential.

These findings set practical limits for the design of a PWFA experiment. The acceleration distance should be such that the driver is close to depletion. This choice is the best trade-off between acceleration efficiency (longer acceleration distance desired) and stability (avoiding depletion despite energy fluctuations of the driver).

4.3.2 Stability of the witness in PIC simulations

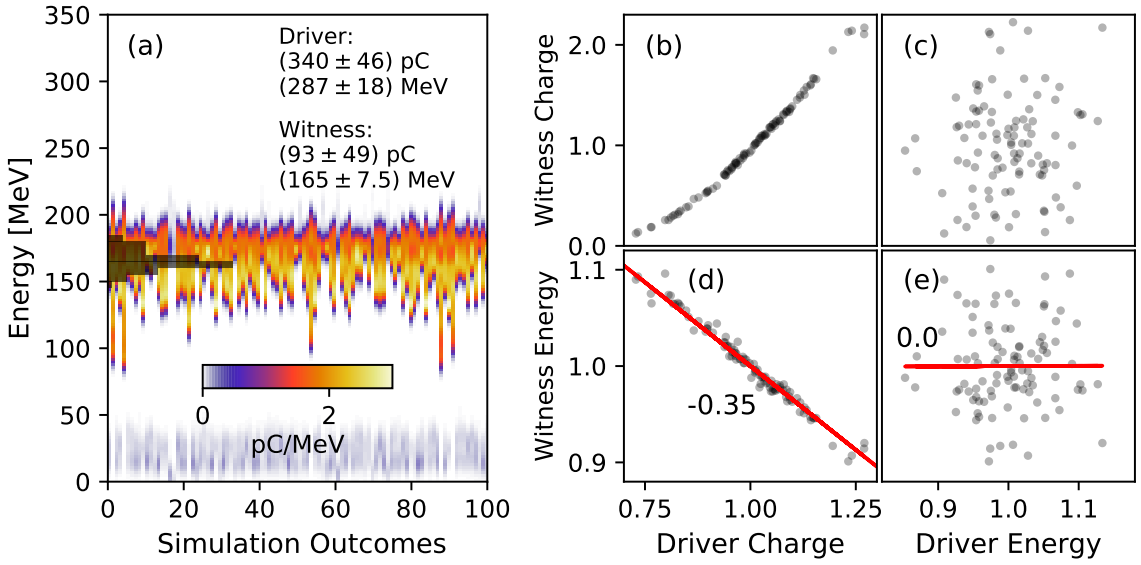

Figure 4.5: ***PIC results for random driver charge and energy variations.*** *Panel (a) shows the witness spectra from a set of 100 simulations. The drivers' charge and energy independently vary around the experimental working point. Panels (b)-(e) sort and rearrange the same simulations by charge and mean energy of driver and witness. A clear correlation of the driver charge with witness charge, and witness energy (slope=-0.35) is visible. There is no significant correlation of the witness properties with the driver energy.*

The next set of 100 simulations varies driver charge and energy around the experimental working point (287 MeV and 340 pC). A normal distribution with a standard deviation according to the experimental values is assumed for both quantities. A random and independent sampling of these distributions generates the input values for individual simulations. The waterfall plot in Figure 4.5(a) summarizes the simulation outcome by showing the individual witness spectra for the whole set of 100 simulations. The witness mean energy is (165 ± 7.5) MeV (SD) and its mean charge is (93 ± 49) pC (SD). Therefore, the relative energy variation of the simulated witness is approximately half of the value measured in the experiment ($|\delta E_{\text{witness}}[\%]| \leq 0.34\,|\delta Q_{\text{driver}}[\%]|$). The next sections elaborate on the reasons for this higher stability of the witness energy than observed in the experiment.

To understand the relatively high stability of the witness energy in PIC simulations, they are sorted by driver charge and energy, respectively. The scatter plots in Fig.4.5(b)-(e) represent the data from panel (a) with random fluctuations of driver

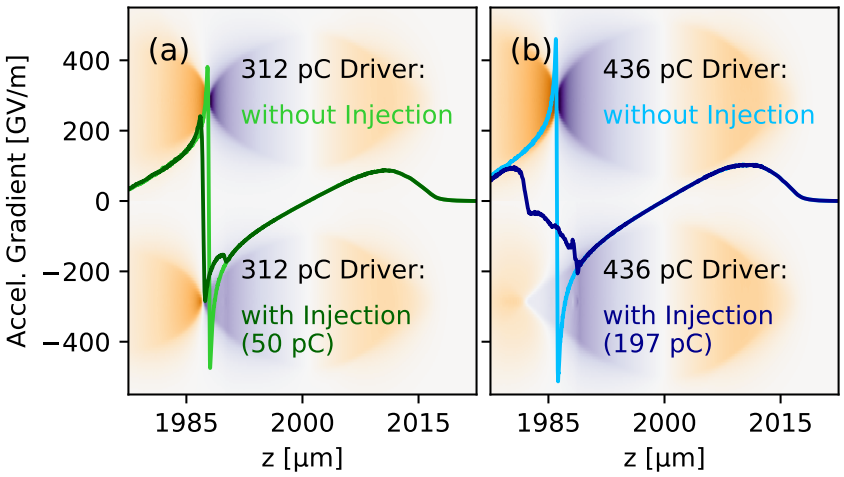

Figure 4.6: ***Beam loading at different levels of driver and witness charge.*** *The on-axis longitudinal electric field is plotted for two different driver charges of (a)* 312 pC *and (b)* 436 pC*. For both drivers, the situation with (dark-colored lines) and without a down ramp for injection (light-colored lines) is compared. Beam loading results in an inversion of the wakefield's slope at the witness's position. Since the amount of injected charge scales with the driver charge, this effect leads to an approximate local flattening of the field (a) or strong overloading of the wakefield (b).*

charge and energy. While the witness properties show no statistically significant dependence on the driver energy, they clearly correlate with the driver charge. The higher the driver charge, the more witness charge is injected. Contrary to the conclusion from the simplified model, the witness energy decreases with increasing driver charge. This negative slope means that the higher witness charge overcompensates the effect of the stronger wakefields, which are expected at a higher driver charge. This behavior strongly indicates beam loading [29], requiring a closer look.

4.3.3 Scan of driver charge

The beam loading effect is studied in more detail in a dedicated scan of the driver charge. In this set of simulations, the driver charge is scanned between $240 - 440$ pC while keeping all other input parameters fixed. Following on from this, the simulations are run again, but without the down ramp for injection. Consequently, in this set of simulations, no witness bunch is injected. The difference in wakefield strength between both cases quantifies the effect of beam loading. The influence of the witness bunch on the wakefields (dark-colored lines) is clearly visible compared to the unloaded case (light-colored lines), as seen in Figure 4.6. For a driver charge of 312 pC (4.6a), a witness with 50 pC is injected, reducing the maximum field strength and lengthening the bubble by 1 μm. For a higher driver charge of 436 pC (4.6b), a witness with 197 pC is injected, lengthening the bubble by 5 μm. This witness current is much too high for optimal beam loading, as seen by the steep negative slope of the field.

Probing the longitudinal phase space in PIC simulations

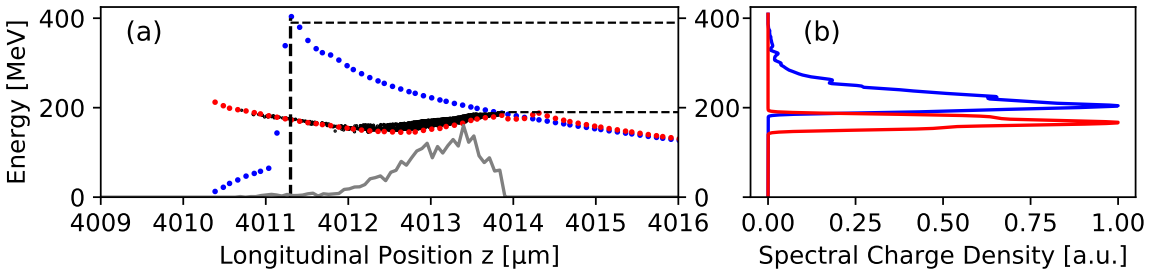

Figure 4.7: ***Hypothetical energy gain of the witness in an unloaded PWFA.*** *Dotted lines in (a) represent the energy gain of test particles as a function of their co-moving coordinate. The red dotted line corresponds to the simulation outcome with a density down ramp for witness injection. The phase space of the witness bunch (solid black) follows the red curve. The spectrum in (b) is calculated by projecting the witness current (gray in a.u.) onto the phase space of the test particles from the simulation without injection (blue dotted).*

To quantify the effect of the beam loading on the witness spectra, all simulations include an additional electron species to probe the wakefields. These test particles sample the longitudinal extent of the bubble, have a negligible charge density, and are initialized to be very rigid at a high electron energy of 10 GeV. They mimic "test electrons" in the usual sense of electrodynamics, i.e., the electrons are exposed to the electromagnetic forces of the wakefield but do not alter the field themselves. The difference in γ_z of individual test particles in the last time step of the simulation and the time step where witness injection occurs represents the energy gain of witness electrons as a function of their co-moving coordinate.

For the simulations with density down ramp, the energy gain of the test particles (red dotted line in Fig. 4.7a) is identical to the one of the injected witness (solid black). In contrast, the test particles gain much more energy in the unloaded wakefield, as indicated by the blue dotted line. This increased energy gain concerns all particles at positions behind the leading edge of the witness beam (for $z < 4014\,\mu\text{m}$ in the example). An artificial spectrum (Fig. 4.7b) for the unloaded case is calculated by projecting the witness current (gray line) from the simulations with injection onto the phase space of the test particles from the simulations without injection. Parts of the phase space that have interacted with the second bucket of the wakefield during parts of the simulation (corresponding to points beyond the kink at 4011.3 µm in Fig. 4.7a) are discarded. In the unloaded case, the slope of the wakefield imprints a chirp on the witness bunch. This chirp leads to a broader spectrum and higher cut-off energies (blue line in 4.7b) compared to the beam-loaded case (red line in 4.7b).

Spectra with and without beam loading

A comparison of the witness spectra as a function of the driver charge for both the loaded and unloaded wakefield scenario shows the influence of beam loading on the witness energy gain (see Fig. 4.8b). Again all numbers are normalized to the nominal

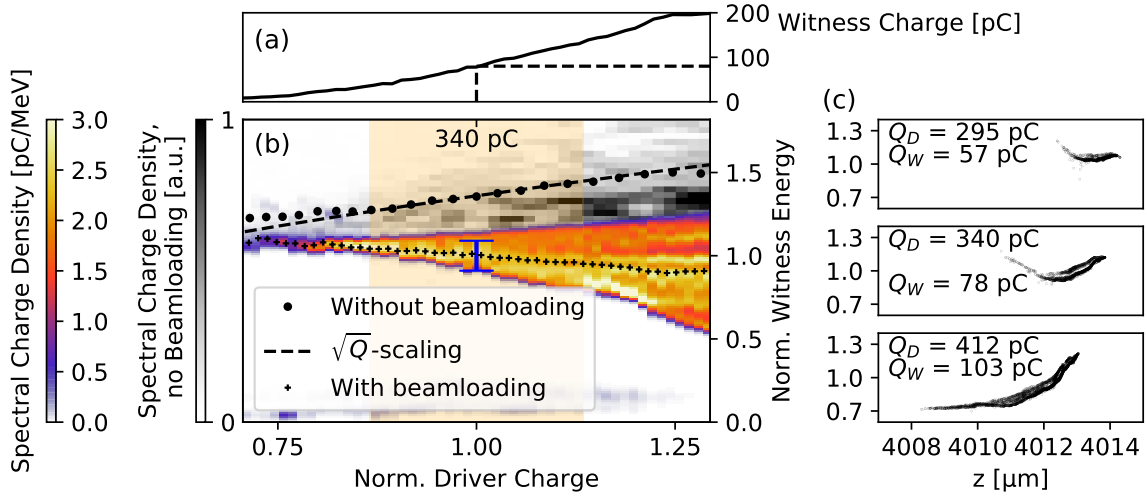

Figure 4.8: ***Scaling of the witness energy with the charge of the driver.*** *In (b), the evolution of the witness spectrum with increasing driver charge for both the beam-loaded and unloaded case are compared. The standard deviation of the witness energy in the experiment is given as a blue error bar for comparison. In (a), the witness charge is plotted for the spectra from (b). Panel (c) shows the longitudinal phase space for three different values of driver charge and corresponding witness charge.*

experimental working point for convenience. The mean energy of the witness in the hypothetical unloaded case increases with increasing driver charge. The variation of driver charge of ± 30% is not wide enough to confirm without any doubt the theoretical $\sqrt{Q}$-scaling for the longitudinal wakefield strength as a function of the driver charge. However, the slope of $\delta E_{\text{witness}}[\%] = +0.48 \cdot \delta Q_{\text{driver}}[\%]$ around the working point is in good agreement with the theoretical prediction (slope = +0.5).

In the simulations with witness injection, the mean witness energy slightly decreases with increasing driver charge at a rate of $\delta E_{\text{witness}}[\%] = -0.35 \cdot \delta Q_{\text{driver}}[\%]$ around the experimental working point. This energy decrease is accompanied by a broadening of the spectrum towards stronger drivers.

The downward shift of the spectra is in contrast to the analytical model and the simulations of the unloaded case. The decreasing energy gain is a direct consequence of the reduced wakefields due to the increasing amount of injected charge. This beam loading also explains the broadening of the spectra. Figure 4.8c shows that the witness bunches become longer with increasing charge. At the same time, the fields seen by the tail of the bunch become weaker (cf. Figure 4.6b). Thus, the spectrum, representing the projection of the longitudinal phase space onto the energy axis, becomes broader.

PIC simulations are a vital tool to reveal these correlations between driver charge and witness properties, as here, the complete set of driver and witness properties is available. In contrast, in all PWFA experiments, the PWFA stage deletes the information about the initial driver charge. Therefore, only the mean and standard deviation of driver charge and witness energy (orange shade area and blue bar in Fig. 4.8(b)) of similar runs can be compared, but not the sign of $\delta E_{\text{witness}}/\delta Q_{\text{driver}}$.

The experimentally measured fluctuations in witness energy were likely larger than predicted by the simulations because the injected witness charge also fluctuated due to other parameters that were kept constant in the simulations (e.g., gas density distribution, down ramp gradient and height). A random contribution to the witness energy weakens the correlation of driver charge and witness charge and, consequently, the stabilizing effect of the beam loading.

TAKE-HOME MESSAGE

PIC parameter scans of the driver's charge and energy show no dependence of the witness energy on the driver's energy. The theoretical scaling of the wakefields with the driver charge ($E_z \propto \sqrt{Q_{driver}}$) is confirmed. Also, a further energy-stabilizing influence of beam loading in the PWFA is found.

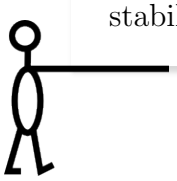

4.4 Discussion of the limited energy gain in PWFA

[4]In general, the energy of the witness is ultimately limited by two factors; the depletion of the drive beam and the accelerating field seen by the witness until the driver depletes.

Driver depletion is quite a complex process, as the decelerating field usually varies along the drive bunch's length. As a consequence, parts of the beam might already be stopped before other parts have efficiently transferred their energy via the wakefield to the witness. A first preliminary study on driver depletion and beam break-up is presented in Section 6.2 (*Future developments*).

In the specific implementation of our PWFA target, there were major limitations for the effective accelerating field. Due to spatial constraints, the wakefield axis was aligned to be 5 mm away from the nozzle exit in the PWFA stage for the data shown in Fig. 4.1. As a result, there was no plateau region in the density distribution of our target. As seen in Fig. 4.3, the effective acceleration length is limited to about 1.5 mm because of the long density down ramp and the associated dephasing of the witness bunch due to bubble lengthening in the down ramp. While these issues can be solved easily by choosing a suitable target, there is a more general problem, namely the degradation of driver emittance.

There are two primary sources of driver emittance growth. The first concerns the experimental setup with laser block tape between both acceleration stages and is due to the Weibel-type current filamentation instability [93, 106]. In this two-step process, the drive laser triggers strong currents by pushing electrons into the ionized tape while being reflected at its overdense plasma surface. The stream of low-energy electrons filaments, creating strong transverse field gradients in the tape. Subsequently, the LWFA electrons suffer an emittance growth during their interaction with the resulting magnetic fields in the structured plasma of the laser blocker tape.

[4]This section closely follows the supplemental material of the authors' publication: Foerster et al. PRX (2022) [68].

The second important source of emittance growth is a result of the drive beam entering the PWFA with its phase space not matched to the local betatron oscillations. Due to the emittance growth, the beams' full potential to drive strong wakefields in the PWFA is not used. In the following, the consequences of this increase in driver emittance are investigated using PIC simulations.

4.4.1 Scan of driver emittance

Setup of the PIC simulations

For the following set of simulations, the normalized emittance was initialized with values between $\epsilon_n = 0.1 - 20$ mm mrad. To that end, the RMS-divergence σ_θ was varied while the RMS-radius of the drive beam before entering the PWFA was kept constant at $\sigma_r = 5\,\mu\text{m}$. The position and angle coordinates in phase space were uncorrelated (untilted ellipse) for all simulations. This assumption roughly approximates the influence of a tape placed $l \sim 1\,\text{cm}$ after the LWFA and just before the PWFA. In this scenario, the size of the bunch when traversing the tape is mainly given by the free space propagation at the measured divergence of the LWFA electrons of $\sigma_{\theta,\text{LWFA}} \sim 0.5\,\text{mrad}$:

$$\sigma_{r,\text{ at tape}} = \sigma_{\theta,\text{LWFA}} \times l = 0.5\,\text{mrad} \times 1\,\text{cm} = 5\,\mu\text{m}$$

The interaction with the tape then scrambles up the electron's phase space distribution, as reflected by the increased beam divergence $\sigma_{\theta,\text{ after tape}} = 2\,\text{mrad} > \sigma_{\theta,\text{LWFA}}$. The geometry and the definition of the symbols are summarized in Figure 4.9. With these approximations, the experimental value of the normalized driver emittance after the laser blocker is

$$\begin{aligned}\epsilon_\text{n} &= \gamma\sigma_{r,\text{ at tape}} \times \sigma_{\theta,\text{ after tape}} \\ &= 500 \times 5\,\mu\text{m}\,2\,\text{mrad} \\ &= 5\,\text{mm mrad},\end{aligned}$$

and therefore within the range considered in the PIC simulations.

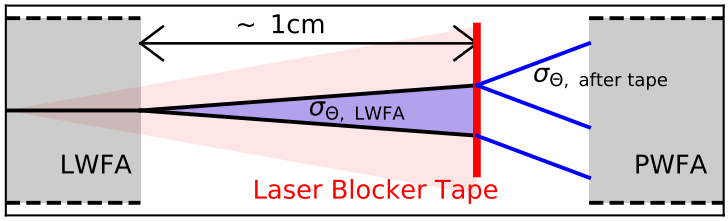

Figure 4.9: Development of the driver divergence

Driver self focusing

The LWFA-generated electron beam starts driving a wakefield when entering the PWFA target. As presented in the theory chapter, the transverse component of these

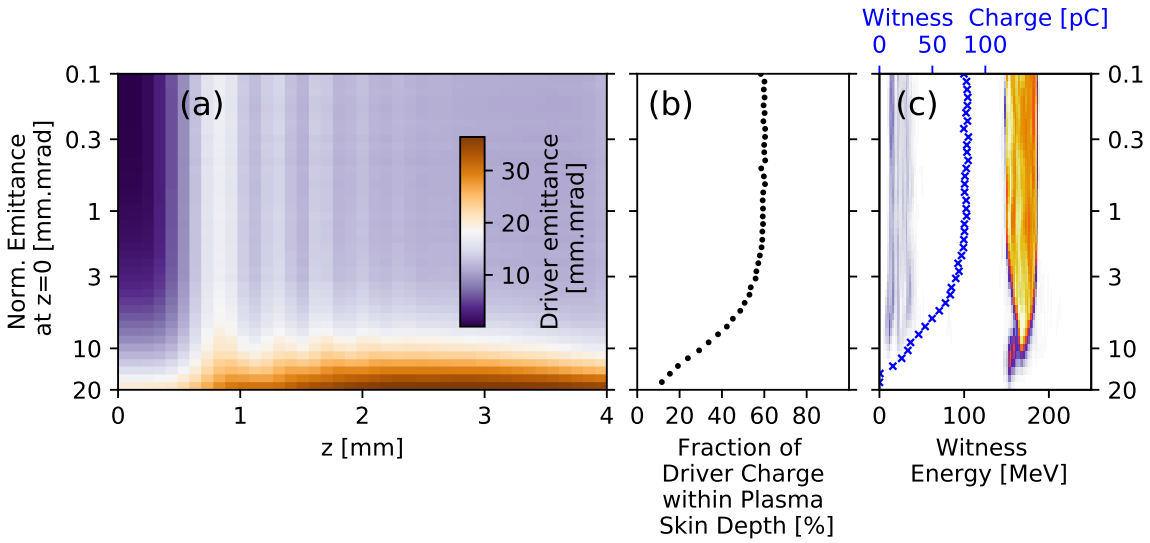

Figure 4.10: ***Simulation results on a scan of the driver emittance.*** *Different driver and witness parameters are given as a function of the initial normalized emittance of the drive beam. For all initial emittance values* $< 5\,\text{mm mrad}$ *the driver evolution (a) is very similar, and the emittance saturates at a level of* $\sim 10\,\text{mm mrad}$*, given by the fact that the beam is not matched to the local betatron oscillation when entering in the plasma. Both the amount of driver charge refocused in the plasma to a spot smaller than the plasma skin depth (b) and the witness spectrum and the injected charge (c) are mostly constant as long as the initial driver emittance is* $< 5\,\text{mm mrad}$*.*

wakefields causes a focusing force on the electron beam [66, 107]. The more charge is refocused to a spot smaller than the blowout radius, the stronger the excited wakefield is (see Section 1.3.3). To quantify the beam self focusing, the amount of charge refocused to a diameter of less than one plasma skin depth $\lambda_p/2\pi$ is analyzed. This charge, is mostly insensitive to the driver emittance in a range between 0.1 and 5 mm mrad, as seen in Fig. 4.10(c). For higher values of the driver emittance, the amount of captured charge and, equivalently, the wakefield strength drops quickly.

In Figure 4.10(a), the evolution of the driver emittance during propagation through the PWFA is plotted. At our experimental conditions, it quickly degrades to a value around 10 mm mrad. Only for very large initial emittance of larger 10 mm mrad the evolution in the plasma is drastically different and the driver degrades even further. This emittance evolution can be understood when considering the phase space trajectories of individual electrons in the wakefield. These particle trajectories are determined by the betatron oscillations and are analyzed in the following.

Phase space matching

As the drive beam is sent into the PWFA stage without using any refocusing device, it is relatively wide ($\sigma_{r,\,\text{at tape}} \sim 5\,\mu\text{m}$). Figure 4.11(a) shows the driver phase space at the beginning of the PWFA and compares its contour (dashed black) with a matched one (dashed blue) of equal emittance. The mismatch is evident from the very different

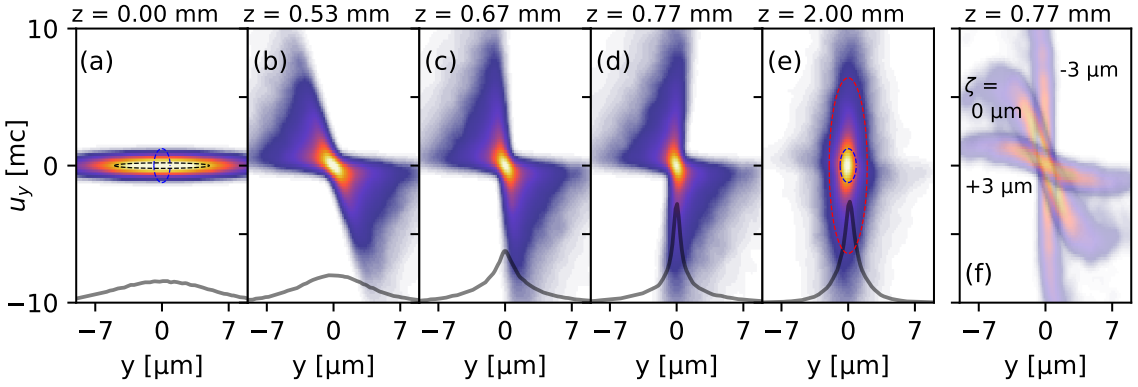

Figure 4.11: ***Evolution of driver phase space when entering PWFA.*** *In (a)-(e), the $y - u_y$ phase space of the drive beam is plotted at different propagation distances z in the PWFA. Grey lines indicate the charge density as a function of the transverse position y. The contour of the initial RMS phase space ellipse is plotted as a black dashed line in (a). For reference, the phase space ellipse of a matched bunch of equal emittance (dashed blue) is given in (a) and (e). In addition, panel (e) shows the RMS phase space ellipse of the degraded beam after propagation (dashed red). Panel (f) shows the the dependence of the betatron phase advance on the co-moving coordinate ζ (the z-slice) in the same timestep as in (d).*

ratios of the semi-axes of the two ellipses.

During propagation, the beam rotates in phase space and becomes more focused. In the simulation, it takes 0.77 mm to reach the point of tightest focus. At the same time, a substantial increase of the filled phase space area is visible, i.e. the emittance is spoiled. The reason for this becomes clear in Figure 4.11(f). Here the phase space distribution is plotted for individual longitudinal slices of the drive bunch. The head of the beam ($\zeta = +3\,\mu\text{m}$) barely evolves, as it does not see the focusing fields inside the bubble. In contrast, the tail of the bunch ($\zeta = -3\,\mu\text{m}$) sees the full wakefield and has the fastest betatron phase advance. Note that even the slice emittance will eventually increase because the phase space distribution smears out due to chromatic effects and nonlinear contributions to the focusing force. At the center of the nozzle (Fig. 4.11(e)), the overall shape of the phase space distribution is very close to the matched one, however, at a much higher than the initial emittance value.

The mismatch of the phase space of the drive beam can be seen as detrimental to the experiment, as its full potential to drive a strong wake is not used. However, the simulations also show the insensitivity of the PWFA to the driver emittance over a wide range of realistic emittance values of an LWFA-generated electron bunch. The lower energy gain in experiments with laser blocker tape could be related to the drop in wakefield strength for > 5 mm mrad observed in the simulations. However, due to the uncertainty about the exact phase space of the driver after the laser blocker and the exact density distribution of the PWFA, we cannot fully reproduce the low-energy witness spectra in our simulations.

4.5 Summary and significance

The central result of this chapter is the experimental proof of highly stable witness beams. An optically-generated density down ramp decouples the injection position of the witness beams from jitters in the hydrodynamic gas flow of the PWFA target. The increased stability of the injection translates into higher stability of the witness energy. The fraction of relative witness energy jitter to relative driver charge jitter is as low as 0.68 and indicates a damping behavior of the PWFA towards charge fluctuations of the driver. It should be noted that the energy stability in this experiment is comparable [91] or even superior [92] to recent experiments involving large-scale rf-accelerator-driven PWFAs and all-optical density down ramp (Torch) injection.

Extensive PIC simulations underline the importance of the beam loading effect in PWFA. In the simulations, the witness charge increases with driver charge, limiting its own energy gain due to beam loading. Based on the simulation results, beam loading can further stabilize the witness energy. In future experiments, the adjustability of the optically-generated down ramp should be further exploited. Ideally, the injected charge correlates positively with the driver charge, with a slope that exactly cancels the effect of the stronger wakefield. This way, the amount of witness charge injected would fully compensate for the shot-to-shot variations in the driver charge. For even better control of the amount of injected charge, the injection should be further decoupled from target and drive beam properties. This decoupling can be achieved in advanced injection schemes like a plasma photo-cathode (Trojan Horse) [45]. These advanced injection schemes are also the reason why the setup with laser blocker tape is still of great interest for future experiments. These experiments require that the spent laser driver of the LWFA is removed, leaving unionized energy levels in high-Z gasses for controlled ionization and injection by an injector laser beam.

PIC simulations reveal the driver's emittance evolution. The drive beam is sent into the PWFA stage without using any refocusing device. Consequently, after a free space drift of several mm, the phase space distribution of the witness is not matched to the local plasma conditions when entering the PWFA. Therefore, the initial driver emittance is not conserved during the interaction with the plasma in the PWFA stage. It quickly degrades to around 10 mm mrad in our experimental conditions. Using a plasma lens between both stages in future experiments may increase the strength of the wakefield. However, more charge will be injected with a stronger wakefield and the same density down ramp. It remains to be investigated, through simulations or experiments, what charge level is appropriate for flattening the longitudinal phase space in this future regime. In any case, the properties of the optically generated down ramp have to be adjusted to avoid excessive beam loading.

So far, the ability of an LWFA-driven PWFA to produce witness bunches with stable energy has been discussed. The following chapter shows that improvements in other quality parameters are also possible. In particular, witness beams can be produced that are spectrally and spatially denser than their respective driving beams.

5 High quality witness bunches

As outlined in the previous chapter, a staged L-PWFA can generate electron beams with improved energy stability. The following section explains how to modify the experimental setup to achieve further gains in beam quality. Here, quality refers to the beam's divergence, energy spread, charge density, or a combination thereof. Experiments show that some of these parameters can be improved by carefully adjusting the injection and acceleration process.

The concept of 6D beam brightness is often used to evaluate the usefulness of electron beams for applications and is commonly defined as the beam current I divided by its two transverse emittances ϵ_n and its energy spread σ_δ (in units of 0.1%):

$$B_{6D} = \frac{I[A]}{\epsilon_{n,x}[m]\epsilon_{n,y}[m]\sigma_\delta[0.1\%]} \tag{5.1}$$

The brightness is a measure of the electron density in phase space. However, since phase space is generally not directly accessible experimentally, this chapter first focuses on the generated witness bunches' divergence and spectral charge density. Then, a new figure of merit, the angular spectral charge density is introduced. It combines both the spectral and spatial density of the electron bunch. Simply put, it is a reduced version of the 6D-brightness, considering only those beam properties accessible in the experiment.

5.1 Experimental setup

The general setup and configurations for all experiments are introduced in Section 2.4.2. The next set of experiments (referred to as Exp.7, Exp.8, and Exp.9 in the methods Section 2.4.2) does not use a laser blocker tape between both jets. This setup modification leaves an electron beam and an already diffracted laser in the second jet. Their relative contribution to the wakefield formation in the second jet is analyzed. With a vacuum divergence given by the focusing geometry of 15 mrad (half opening angle), the laser intensity I_l drops by about two orders of magnitude with respect to the first jet after 1 cm of vacuum-propagation between both stages:

$$\frac{I_{l,LWFA}}{I_{l,PWFA}} \sim \frac{(1\,\mathrm{cm} \times 30\,\mathrm{mrad})^2}{(30\,\mu\mathrm{m})^2} = 100. \tag{5.2}$$

The actual divergence is likely even higher because this estimate neglects self-focusing in the first jet, which leads to a smaller spot and larger divergence at the exit of the first plasma. Götzfried et al. [29] observe a similar reduction in intensity in start-to-end PIC simulations for their earlier publication on high-charge bunches from LWFA. Assuming no laser energy loss in the LWFA stage, the divergence leads to an upper boundary for the normalized vector potential of $a_0 \leq 0.34$. Consequently, the laser is expected to drive a weak, linear density perturbation at most. The electron beam, on the other hand, can still drive a strong wakefield in the blowout regime. Its divergence is typically one order of magnitude smaller than that of the laser, and the beam can self-focus at lower plasma densities than the laser [42].

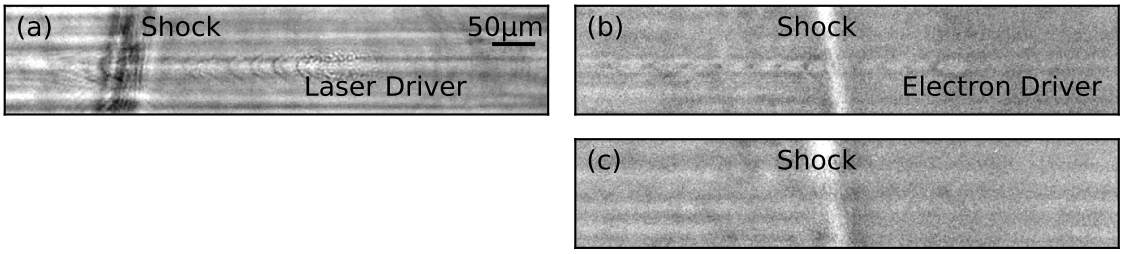

Figure 5.1: ***Plasma-waves in the LWFA and the PWFA stage.*** *(a): A laser-driven plasma wave in the LWFA stage after crossing through the shock-front. (b): In the PWFA stage both the electrons from the LWFA stage and the diffracted and depleted laser are present. The wave train exhibits a distinct bubble-like feature at the position of the drive beam. (c): The driver current in the PWFA stage is reduced by removing the blade for shock-front injection in the LWFA stage. Under otherwise identical conditions, no plasma wave is observed in this setup. One can conclude that predominantly the electrons drive the wakefield in the second stage. The horizontal stripes, which are particularly visible in the case of the laser-driven plasma wave, arise from the filamented ionization of the plasma by off-axis intensity maxima. In all images, the respective driver propagates from left to right.*

Optical probing experiments verify these considerations about the relative contribution of both driver species. Figure 5.1(a) and (b) show the few-cycle shadowgraph of a plasma wave, which propagates to the right. For both stages, the respective density down ramp for injection is visible. In the laser-driven case, a grainy feature leads the wave train (Fig. 5.1a), a typical observation for the case of a highly relativistic laser driver. The wakefield is flanked by off-axis striations extending further downstream than the peak of the laser driver. These striations are attributed to the laser being intense enough to ionize plasma in off-axis intensity maxima and already early in the leading edge. In the second jet, a distinct bubble-like feature leads the wave train (Fig. 5.1b), while a grainy feature, as in LWFA, is not present. In Figure 5.1(c), the LWFA-generated drive bunch is switched off by removing the blade for shock-front injection in the LWFA stage. At otherwise identical conditions, the plasma wave in the second jet vanishes, indicating no observable laser-driven wakefield. Therefore, from these considerations, we can conclude that the contribution of the diffracted laser beam in the PWFA stage is negligible.

The drive beam (Fig. 5.2a) for the next experiment has a charge of (657 ± 61) pC (SD) in the high-energy feature at 250 MeV. When switching on the PWFA, but without a down ramp for injection, a broadband background of decelerated driver charge as shown in Figure 5.2(b) is observed.

5.2 Decreasing witness divergence

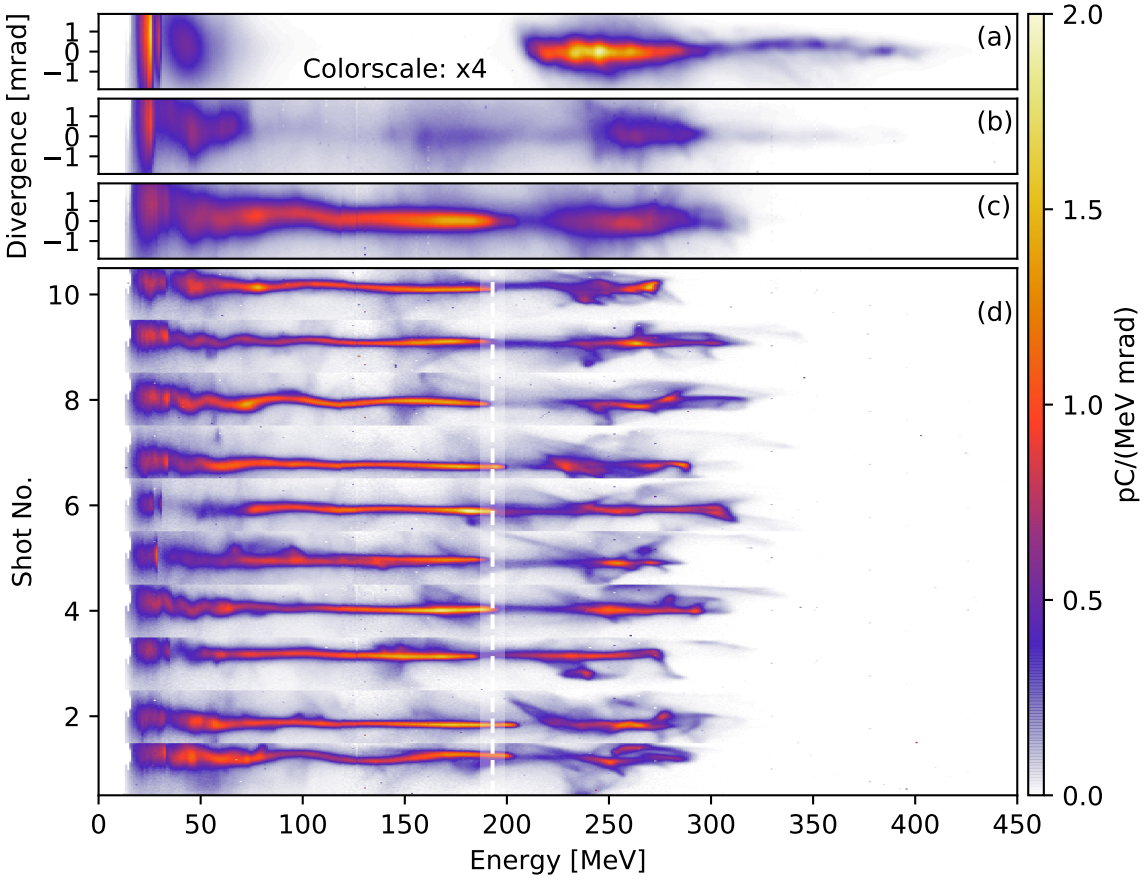

Figure 5.2: ***Spectral Features of LWFA and PWFA electron-bunches.*** *Panel (a) shows the spectrum of the LWFA-generated drive beam. The low-energy feature at* 30 MeV *is attributed to a second injection event. Panel (b) shows the driver spectrum after the PWFA stage without a down ramp for injection. In addition to the initial driver features, there is a broadband background due to decelerated driver charge. Panel (c) shows the spectrum after the PWFA stage with an injector. The high-energy cut-off of the witness bunch injected at the density down ramp is visible at* 200 MeV *on top of the spectral features from (b). Panels (a) to (c) show pointing aligned averages of 10 consecutive shots. Panel (d) shows the high witness energy stability of 10 consecutive shots. Please note that the scale on the color bar has to be multiplied by a factor of 4 in panel (a).*

For an injector laser beam with a peak intensity of $2 \times 10^{16}\,\mathrm{W/cm^2}$ and 10 mm gap between the jets, broadband witness bunches are produced on every shot. A pointing aligned averaged spectrum is shown in Figure 5.2(c) together with a set of 10 consecutive shots in panel (d) of the same figure. The charge of these broadband witness bunches was (100 ± 25) pC. The large error margin is mainly given by the uncertainty about the decelerated driver charge and its spectral overlap with the witness. These witness bunches feature sub-Millirad divergence over their whole spectrum and have a

distinct and stable high-energy cut-off energy at (193 ± 6) MeV (3%, SD in the set of 10 consecutive shots shown in Fig.5.2(d)). This low jitter of the witness energy is in line with the observations reported in the previous chapter. The sub-Millirad divergence of these bunches is much lower than typically reported for LWFA bunches in the same energy regime (typ. few-Millirad-level) and was previously only observed for near-GeV beams [108] (see also Figure I.3 in the Introduction).

5.2.1 Influence of pre-ionization of the target

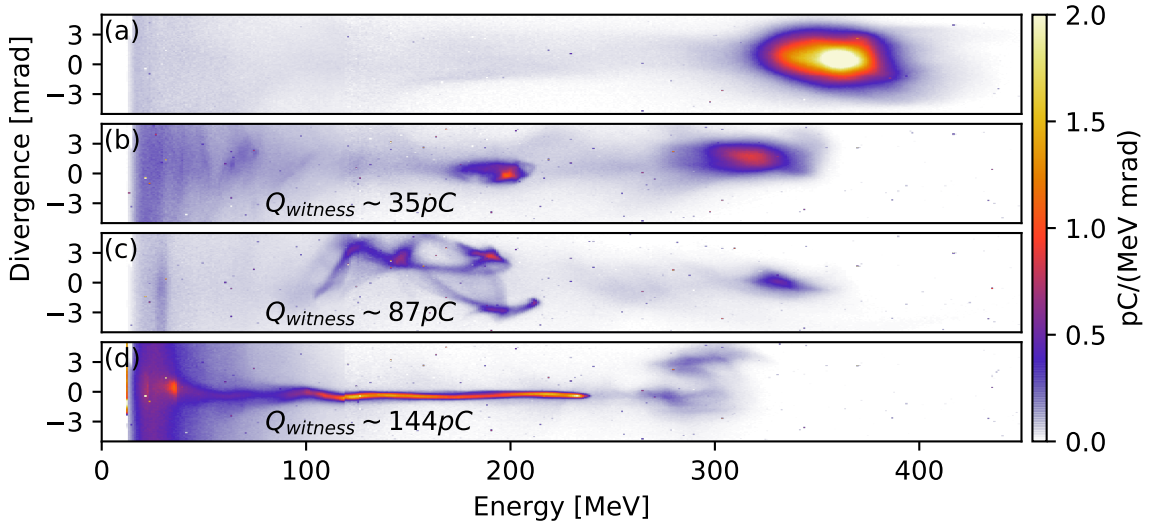

Figure 5.3: ***Influence of a pre-ionized PWFA target on the witness beam.*** *(a) Spectrum of a drive beam with laser blocker tape in position, but PWFA switched off. (b) Spectrum after the PWFA stage with tape, but without pre-ionization. (c) Spectrum after the PWFA stage with tape, with pre-ionization of PWFA target. (d) Spectrum after the PWFA stage without tape. The plasma density in the PWFA and the injection position are identical for (b)-(d). All shots are representative of their respective conditions.*

The initial state of the PWFA target dramatically influences the properties of the injected witness bunch. Figure 5.3 compares the spectra of three different witness beams obtained under different ionization states of the PWFA target. The spectra in (b) and (c) are obtained with laser blocker tape between both jets, once without pre-ionization (b) and once with the PWFA pre-ionized by an auxiliary beam (c). The transverse properties are more favorable without pre-ionization, as the beams show much smaller amplitude signatures of betatron oscillations. However, as seen before in Section 3.3 (*Scan of injection position*), also the deceleration of the driver is less efficient, and the accelerating gradients are generally lower without pre-ionization. The highest quality bunches in terms of divergence and maximum energy are achieved without laser blocker tape (d), i.e., with a stronger driver and very homogeneously pre-ionized PWFA. The reasons for the very different quality of the electron bunches will be discussed in a moment.

In previous work, a pre-ionized target proved to be crucial. It is required to void the volume behind the driver of electrons completely and to ensure defined trajectories of the expelled plasma electrons around the sheath in the bubble regime [42, 43, 65]. This is a prerequisite for developing a strong blowout with linear focusing fields. Furthermore, any transverse asymmetries have been identified to have a detrimental effect on the wakefield's symmetry and increase the betatron radiation yield. These asymmetries can originate from asymmetric drivers. Among others, this asymmetry can be due to either pulse front tilt in LWFA [87, 109], the CEP phase of few-cycle drive lasers [110], or asymmetric drive bunches in PWFA [111]. In addition, asymmetries can also stem from the plasma target, either in the form of transverse density gradients [112] or a transversely varying degree of ionization, as was likely present in this experiment.

In experiments without a laser blocker between both jets, pre-ionization is trivial, as the collinearly propagating spent LWFA driver homogeneously ionizes a wide column around the wakefield axis. For some experiments, this configuration without laser blocker tape might be undesirable. In that case, an auxiliary laser beam picked out from the main beam can be used as a pre-ionizer. The pre-ionizer beam is timed to arrive a few ps before the drive beam. This timing ensures that the target is pre-ionized over its full length, but on the other hand, the delay is short enough that no strong density fluctuations develop due to a locally expanding plasma (compare Section 1.4.1). However, spatially overlapping the wakefield axis with the pre-ionizer beam over a longitudinal extent of a few mm to cm is non-trivial. The pre-ionizer must be sent from the downstream side because the tape blocks the other side. A long-focal-length optic is needed for the pre-ionizer to achieve an ionization region with a much larger transverse extent (10s of Micrometer) than the wakefield. At the same time, to not disturb the electron beam on its way to the diagnostic, the final steering optic was placed off-axis resulting in an interception angle of $\sim 2°$ (A line focused beam and a holed mirror on-axis were not available during the experiment). This geometry makes it difficult to achieve high enough intensity in a cm-long and 10s of micrometer wide channel overlapping on its full length with the wakefield. Therefore, the geometry in the experiments presented here likely resulted in an inhomogeneously ionized plasma distribution with the disadvantages for the witness beams' quality outlined in the previous paragraph.

5.3 Increasing spectral charge density

The last sections discussed the transverse witness properties only. As such, these witness bunches might not be desirable for applications because their very large energy spread disqualifies them for emittance-preserving beam transport. The PIC simulations in the previous chapter showed that beam loading in the PWFA can help decrease the witness beam's energy spread. An almost flat longitudinal phase space after acceleration was observed when injecting the right amount of charge, which was on the order of a few 10 pC for the specific set of parameters. On the one hand, the amount of injected charge is determined by the properties of the density down ramp, in particular by its

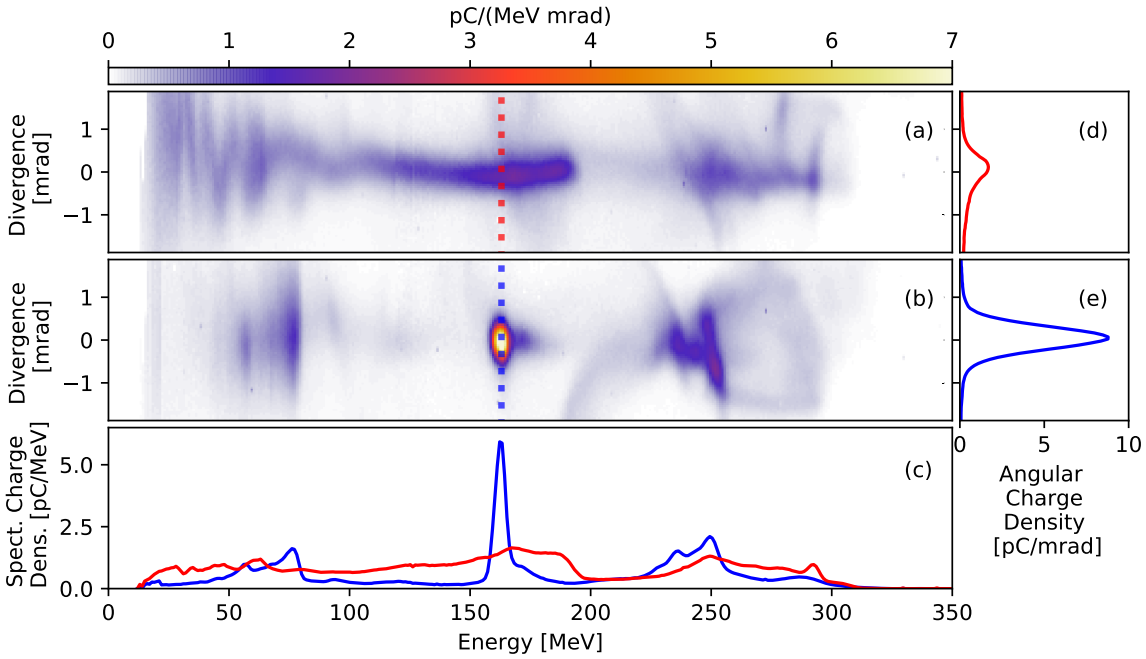

Figure 5.4: ***Increasing the spectral charge density.*** *Panel (a) shows a broadband witness with high charge (≈ 100 pC) but low spectral charge density. Panel (b) shows a witness with its charge (≈ 30 pC) optimized for a low energy spread of 1.5% (RMS-width of Gaussian fit). Panel (c) compares the spectra for both cases. Panel (d) and (e) show the sub-Milliradian divergence of both beams at the indicated energy slice.*

gradient. On the other hand, it depends on the longitudinal momentum of the plasma electrons, which is determined by the strength of the wakefield at the time of injection.

For the next experiment, the strength of the wakefield is varied. The distance between LWFA and PWFA defines the transverse size of the drive beam as it enters the PWFA and therefore determines its further evolution in the PWFA. For this reason, the wakefield strength at the time of injection can be adjusted by setting the stage separation.

By increasing the vacuum gap between both stages from 10 mm to 19 mm, the injected charge decreases from more than 100 pC to as little as 10 pC. For an injected charge of ≈ 30 pC the lowest energy spread is achieved, which is 5.6 MeV FWHM (2.4 MeV RMS, from Gaussian fit to spectrum), see Figure 5.4 (b). The energy spread approaches the energy resolution of the non-imaging dipole spectrometer in our implementation, where a monoenergetic electron bunch at 162 MeV with an FWHM divergence of 0.6 mrad appears to have an energy spread of 3.5 MeV (FWHM). The relative energy spread of these witness beams is as low as 3.5 %. This is five times less than the relative energy spread of the driver (18 %) in this experiment, as seen in Figure 5.2 (a). The decrease in spectral bandwidth coincides with an increase in the spectral charge density of the witness. It is three times higher than in the case of the higher charge but broadband beams (see Fig. 5.4 c). The correct witness charge to minimize the energy spread is relatively low, at around 30 pC. This low charge brings

with it some disadvantages for the stability of the witness electrons. Fluctuations of a few 10 pC have a modest effect on the witness stability at the 100 pC-level. However, at 30 pC, we observe fluctuations between no witness injection at all and the broad-band regime described earlier. The narrow bandwidth shots, as seen in Figure 5.4 (b), are only achieved on a few percent of the total number of shots.

For many experiments, a high phase space density is important. To account for this, the following section investigates the simultaneous optimization of the previously discussed spatial and spectral properties.

5.4 Increasing angular spectral charge density

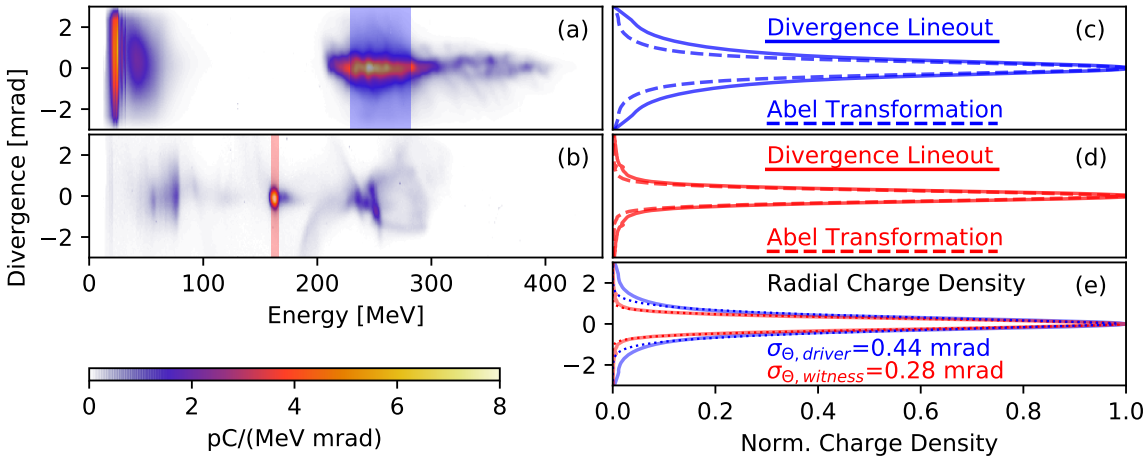

Figure 5.5: ***Radial charge density of driver and witness****. Panel (a) shows the pointing aligned average spectrum of 10 low-divergence drive beams from LWFA. Panel (b) shows the spectrum after the PWFA stage with the charge of the witness optimized for high charge density. Panel (c) and (d) show the divergence lineout and radial charge distribution of the beams from (a) and (b) calculated via an Abel transformation. The radial charge density is evaluated in the shaded energy intervals (spectral FWHM) from (a) and (b). While the drive beam exhibits a narrow-width core and high-divergence wings, the charge of the witness beam is almost fully concentrated in one low-divergence feature. The thin dotted lines in (e) are super-Gaussian fits of the angular charge distributions to deduce the RMS divergence.*

[1] The 6D brightness (charge density in 6D phase space, see Equation 5.1) is a helpful concept for evaluating the usability of electron bunches for applications. Unfortunately, it is difficult to measure because some of the properties of the electron bunch, such as its length and its two transverse emittances, cannot be directly determined with the diagnostics used in the experiment. Such diagnostics for bunch length and emittance exist and have been implemented in the past [25, 113]. However, these diagnostics are generally invasive, as the electron beam must pass through a radiator foil or focusing quadrupole magnets, respectively. Also, due to their complexity, they were not set up

[1] This section closely follows section IV of the authors' publication: Foerster et al. PRX (2022) [68].

during the experiments discussed in this thesis. Due to these limitations, the electron quality is summarized with a new figure of merit, the angular-spectral charge density, based only on experimentally accessible quantities. It describes the spectrally resolved charge density within the RMS divergence, divided by the solid angle corresponding to this divergence. Combining the information on the electron bunch's charge, divergence, and energy spread this new figure of merit characterizes the usability of the beams for applications (see Section 5.6).

Calculating the angular-spectral charge density

Spectra obtained with a dipole spectrometer (as in Fig. 5.5(a)+(b)) are spectrally resolved projections of the electron distribution along one transverse spatial dimension. The radial charge distribution of the electron bunches can be obtained using an inverse Abel transformation (Fig. 5.5(c)+(d)). By that, radial symmetry of the bunches is assumed. The divergence of the beams can then be deduced from the radial charge distribution. Since the standard deviation of a distribution is very susceptible to noise, the data were fitted with a super-Gaussian function (Fig. 5.5(e)). The fitting function is $f(x) \sim \exp\left([-x^2/(2\sigma^2)]^p\right)$, with $p < 1$. Note that a super-Gaussian fitting function models the transverse charge distribution more accurately than a Gaussian one. The LWFA-generated drive beams in this experiment are characterized by low-divergent (sub-Millirad) features on top of a lower density and more divergent (few mrad FWHM) charge distribution. These "wings" are not well modeled by Gaussian functions. However, as seen in Figure 5.5(e) (blue lines), even a super-Gaussian function (dashed) is not able to fully fit the low-density background.

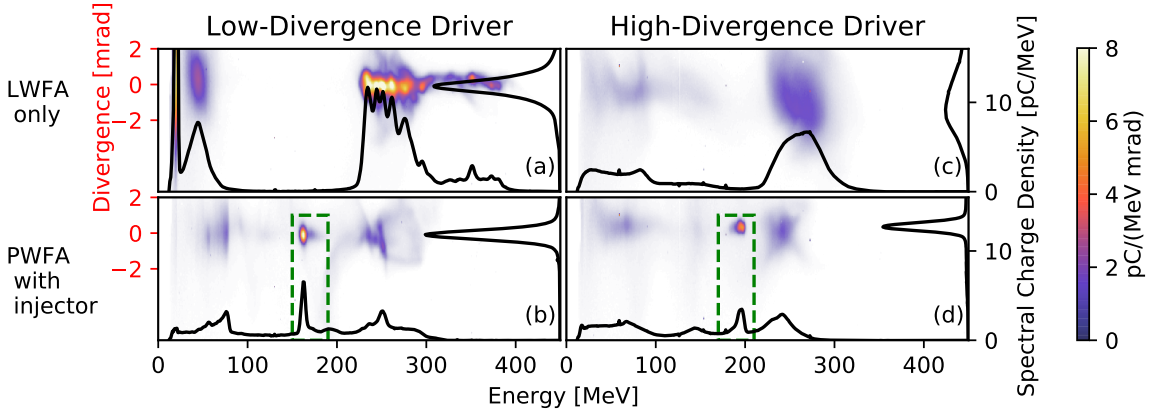

Figure 5.6: ***High-quality witness bunches with low- and high-divergence drivers.*** *The figure shows the driver and witness beams for the two cases of low-divergence (a+b) and high-divergence drivers (c+d). The angularly resolved spectra are plotted together with their respective spectral and angular lineouts.*

Figure 5.6(a) shows a representative drive bunch with a charge of 640 pC in the high-energy feature at 250 MeV. The average charge in this set (compare Fig. 5.5(a)) is (657 ± 61) pC (SD). The shot shown in Figure 5.6(a) has a divergence of 0.41 mrad

(RMS of super-Gaussian fit, average in the blue shaded region). The angular-spectral charge density is 5 pC/(MeV µsr). The respective values for the set-averaged driver are 0.44 mrad and 3.5 pC/(MeV µsr).

The low-divergence (0.28 mrad, RMS of super-Gaussian fit), low energy-spread (3.5%, FWHM) witness bunch (Fig. 5.6(b)) has a charge of 30 pC, which yields an angular-spectral charge density of 7 pC/(MeV µsr). Hence, the witness is approximately 40% denser than the selected drive beam and 100% denser than the averaged drive beam.

Comparing low- and high-divergence drive beams

The production of dense, low-divergence witness beams is not limited to highly optimized, sub-mrad drive beams such as the one shown in Figure 5.6(a). It is also observed in experiments with significantly more divergent LWFA beams as drivers. Figure 5.6(c) shows a representative shot from a different data set. Here, the 400 pC drive bunch has a divergence of 1.2 mrad (RMS of super-Gaussian fit). The angular-spectral charge density is much lower at a value of 0.4 pC/(MeV µsr) at 270 MeV. These drive beams can still refocus when entering the PWFA and drive strong wakefields. As shown in Figure 5.6(d) the witness bunch has a similarly small divergence of 0.22 mrad (RMS of super-Gaussian fit) and 5% (FWHM) energy spread as the beam in Figure 5.6(b). At a charge of 20 pC the angular-spectral charge density of this witness bunch is 6 pC/(MeV µsr) at 195 MeV. Hence, this witness beam is more than an order of magnitude denser than its driver.

The comparison of the two different driver regimes shows that the witness charge density is largely insensitive to the driver divergence in an interval of more than one order of magnitude. This finding is consistent with the simulations in which the influence of driver divergence and emittance on wakefield generation is analyzed (Section 4.4.1: *Scan of driver emittance*). Based on the available experimental data, simulations, and theoretical considerations, reasonable bounds for the emittance and brightness of these witness beams are deduced. They are presented in the next section and conclude this chapter on the quality of the witness beams.

TAKE-HOME MESSAGE

A staged L-PWFA can produce electron bunches with lower divergence and higher spectral charge density than the drive beams used. The angular-spectral charge density is introduced as a figure of merit for electron quality, including only parameters observed in the experiment. This number reaches higher values for the witness than for the driver.

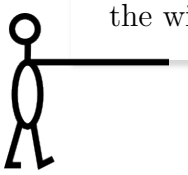

5.5 Emittance and Brightness of the beams

[2] The normalized emittance of the witness beams cannot be derived directly from the diagnostics used during the experiment. Nevertheless, in order to determine the correct order of magnitude, different approaches are compared: On the one hand, witness spectra from PIC simulations are analyzed, and on the other hand, conclusions are drawn from measured data based on the simplified electrostatic model of the bubble (see Section 1.3.3).

5.5.1 Witness emittance in PIC simulations

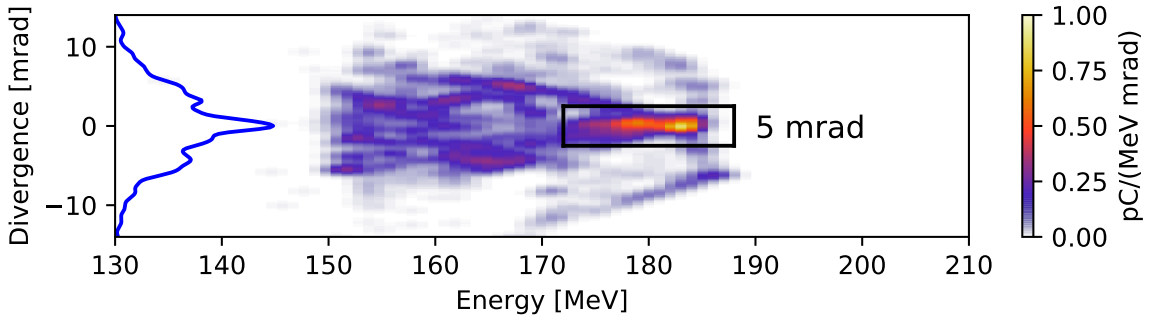

Figure 5.7: ***Simulated example of a witness spectrum as observed in a dipole spectrometer.*** *The beam has a FWHM divergence of* 1.5 mrad. *In addition to the narrow divergence feature, there is a high divergence background that is not observed in the experiment. Evaluating the normalized emittance of electrons in a cone with an opening angle of* 5 mrad *as indicated by the black box yields* $\epsilon_{n,x} = 0.28\,\text{mm mrad}$ *and* $\epsilon_{n,y} = 0.26\,\text{mm mrad}$.

The PIC simulations presented in Section 4.3 can also be used to deduce the transverse properties of the witness beam. However, the validity of the simulations for the transverse properties of the witness should be considered with caution. The predicted beam distribution does not fully agree with the experimental observations. In the experiments, the entire witness charge resolved in the dipole spectrometer is contained in a feature with an FWHM divergence of a few mrad (with laser blocker tape) or well below one mrad (without laser blocker tape). In simulations, there is a high-density feature with a small FWHM divergence of 1.5 mrad, but there is also a much wider low charge density distribution with a divergence of more than 10 mrad (see Fig. 5.7). The imperfect agreement between simulations and experiments is likely due to the choice of a simplified density profile in the simulations. In particular, the plasma diagnostic in the experiment can only insufficiently characterize the exact height and shape of the density down ramp, which can be responsible for an adiabatic focusing of the beam when exiting the plasma [114–116].

[2] This section closely follows section IV and the supplemental material of the authors' publication: Foerster et al. PRX (2022) [68].

The evaluation of the normalized emittance of only the beam core (the low divergence feature of the witness spectrum) yields a value of a few 0.1 mm mrad (e.g., 0.25 mm mrad if analyzing all electrons within an opening angle of 5 mrad, black box in Fig. 5.7). For the full witness species from the PIC simulation, this value increases to above 1 mm mrad.

5.5.2 Estimating emittance from the analytical model

Different estimates for the witness beam emittance can be made from the simplified model for the bubble size. The first calculation starts from the transverse momentum of the electrons at the time of injection. A second calculation looks at the matter from the end. It starts from the measured divergence of the witness beam and relates it to the betatron orbits that result in such divergence.

Starting from Injection

From the simplified electrostatic model (see Section 1.3.3), a maximum transverse excursion of the sheath electrons, the bubble radius, can be calculated. The electrons have been displaced by the drive beam against the Coulomb force F_{ion} of the ion background (Pos. (1) in Fig. 5.8). When falling back onto the axis (Pos. (2) in Fig. 5.8), their potential energy is converted into kinetic energy. At the time of injection, the electrons are assumed to carry the transverse momentum equivalent to this kinetic energy. According to the simplified model, the potential energy V of sheath electrons (Fig. 5.8) in the field of the ion-bubble at maximum transverse displacement $r_b \simeq \sqrt{I_0/\pi e c n_0}$ (Eq. 1.23) is

$$\begin{aligned} V &= \int_0^{r_b} F_{\mathrm{ion}}(r)dr \\ &= e^2 n_0/4\epsilon_0 \int_0^{r_b} r dr \\ &= 30\,\mathrm{eV} \times I_0[\mathrm{A}]. \end{aligned}$$

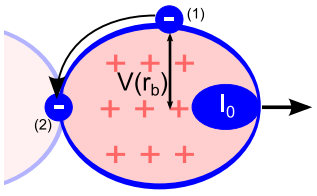

Figure 5.8: ***Potential energy of sheath electrons.***

Hence, the maximum potential energy of a sheath electron only depends on the driver current I_0. For the following rough estimate of the transverse momentum of the sheath electrons, it is neglected that they also acquire substantial velocities in longitudinal direction, breaking the assumption of the electrostatic model. In particular, transverse momentum can be transferred to longitudinal via the B-field.

Assuming the potential energy is fully transferred into kinetic energy by falling back on the axis (Fig. 5.8 (2)), we calculate the corresponding transverse momentum and beam divergence. From the sum of energies

$$V + m_0c^2 = \sqrt{c^2p_\perp^2 + (m_0c^2)^2}, \tag{5.3}$$

a transverse momentum of

$$p_\perp = mc\sqrt{(V/mc^2+1)^2-1} \tag{5.4}$$

is calculated. Electrons carrying the full transverse momentum can be assumed to be the most divergent after exiting the plasma. Assuming a uniform continuous distribution of the transverse momenta among the bunch-electrons, the RMS-momentum of $p_{\perp,RMS} = p_\perp/\sqrt{3}$ can be calculated. At the end of the longitudinal acceleration, the RMS divergence angle is

$$\sigma_\theta = p_{\perp,\mathrm{RMS}}/p_\parallel = p_{\perp,\mathrm{RMS}}/(300mc) = 6\times10^{-3}, \tag{5.5}$$

where we set $\gamma = 300$ as in the experiment presented in Fig. 5.5b and a driver current of $I_0 \approx \frac{400\,\mathrm{pC}}{10\,\mathrm{fs}} = 40\,\mathrm{kA}$. Inside the bubble, the transverse motion of an electron of the witness bunch is a harmonic oscillation. Still applying the electrostatic approximation, its frequency is the betatron-frequency $\omega_\beta = \omega_p/\sqrt{2\gamma}$. The single electron trajectory is fully determined by the particles' transverse momentum at the time of injection. According to the theory of a harmonic oscillator, the oscillation amplitude is

$$r_{\mathrm{betatron,RMS}} = \sigma_x = \sigma_\theta c\sqrt{2\gamma}/\omega_p. \tag{5.6}$$

For $\gamma = 300$ and $n_0 = 1\times10^{18}\,\mathrm{cm}^{-3}$ the RMS betatron radius is 800 nm. Electrons on the RMS betatron trajectory are moving on the phase space orbit that defines the contour of the phase space ellipse. It follows an upper limit for the normalized emittance of

$$\epsilon_{\mathrm{n,max}} = \gamma\sigma_\theta\sigma_x = 300\times6\,\mathrm{mrad}\,0.8\,\mu\mathrm{m} = 1.4\,\mathrm{mm\,mrad}. \tag{5.7}$$

In the experiment, the measured divergence of the witness electrons is about a factor of 10 smaller than this estimate predicts. In addition, the electrons have a continuous angular distribution and, therefore, not just one defined transverse momentum. Both observations hint at a reduced transverse momentum of (some) electrons at the position and time of injection. Depending on the electrons' exact trajectory around the bubble, their momentum when falling back onto the axis can be partially damped by the transverse defocusing field of the on-axis density spike at the rear end of the bubble [105]. Also, the space-charge field of the injected electrons themselves effectively lowers the focusing fields inside the bubble while being injected [69].

Starting from measured divergence

Using the same equations as above, from the measured free-space divergence, a lower limit for the betatron amplitude and the normalized emittance can be calculated

$$\epsilon_n > \gamma\sigma_\theta^{\mathrm{min}}\sigma_x^{\mathrm{min}} = 0.004\,\mathrm{mm\,mrad}, \tag{5.8}$$

where we again assume an energy $\gamma = 300$. $\sigma_\theta^{\mathrm{min}} = 0.3\,\mathrm{mrad}$ is the measured free-space RMS-divergence and $\sigma_x^{\mathrm{min}} = 0.04\,\mu\mathrm{m}$ is the source size at the exit of the plasma

calculated from the betatron trajectory corresponding to this divergence. The main uncertainty in this calculation comes from the source size, which is more than an order of magnitude smaller than reported from LWFA experiments [27, 28], and most likely underestimated in Eq. 5.8. Adiabatic matching of the witness beam divergence can occur in the density down ramp of the jet or in a possible transition from a blowout to a linear wakefield at the end of the acceleration process [114–116]. During this process, the ratio of the two semi-axes of the phase space ellipse changes without increasing its area. In other words, the measured free-space divergence should not be taken as an indicator of the transverse momentum inside the bubble. This means that the equation 5.8 most likely underestimates the emittance.

In conclusion, the divergence of the witness is lower than in other LWFA or PWFA experiments in the energy range of $\sim 100\,\mathrm{MeV}$. Estimates based on the available experimental and simulation data indicate an excellent normalized witness beam emittance of well below $1\,\mathrm{mm} \times \mathrm{mrad}$. However, in future experiments, additional diagnostics [113] and measurements will be required to determine the actual emittance values.

5.5.3 Brightness

The 6D brightness (Equation 5.1) is commonly defined as the beam current divided by its two transverse emittances and its energy spread (in units of 0.1%).

$$B_{6D} = \frac{I[A]}{\epsilon_{n,x}[m]\epsilon_{n,y}[m]\sigma_\delta[0.1\%]}$$

Only a rough estimate of the brightness can be made for the beams presented in this work. This is because neither the emittance nor the bunch length of the witness was measured. A lower and an upper limit of B_{6D} is calculated by varying both the emittance and bunch length between realistic maximum and minimum values

$$B_{6D,min} = \frac{30\,\mathrm{pC}/15\,\mathrm{fs}}{1\,\mathrm{mm} \times \mathrm{mrad} \times 1\,\mathrm{mm} \times \mathrm{mrad} \times 15} = 1.3 \times 10^{14}\,\mathrm{A/m^2}/0.1\%,$$
$$B_{6D,max} = \frac{30\,\mathrm{pC}/2\,\mathrm{fs}}{0.1\,\mathrm{mm} \times \mathrm{mrad} \times 0.1\,\mathrm{mm} \times \mathrm{mrad} \times 15} = 1 \times 10^{17}\,\mathrm{A/m^2}/0.1\%.$$

In these calculations, the upper and lower limit for the emittance is based on the discussion in the previous section. The lower limit for the bunch length is 2 fs, which corresponds to the length of 30 pC-bunches in the PIC simulations. The upper limit was set to 15 fs based on the longitudinal extent of the accelerating phase and corresponding to the upper limit of measurements performed at LWFA-beams [25, 26].

Due to the large uncertainty related to these input quantities, the margin for the brightness varies by three orders of magnitude. Clearly, no final conclusion can be drawn on the brightness achieved in this work. Note that the same problem holds true for brightness values quoted in published literature. Ke et al. [108] provide the most optimistic values so far for beams from a plasma accelerator. They produce beams of similar divergence and charge as found in this work, but at about five times higher

energy. For their beams, they quote a brightness of $\sim 1 \times 10^{16}\,\mathrm{A/m^2/0\,1\%}$. Their confident brightness estimate is based on a normalized emittance of 0.1 mm × mrad and a bunch length of 2 fs, both based on typical LWFA parameters but assumed without further justification.

The comparison between conventional and plasma-based accelerators is inherently challenging due to their different operating parameters. We take as an example the FLASH accelerator at DESY which serves as a driver for an X-ray free-electron laser and as a driver for a PWFA stage in the FLASH-Forward experiment [36]. FLASH generates electron bunches with charges ranging from hundreds of pC to 1 nC and a minimum bunch length of approximately 100 fs, limiting peak currents to a few kA. On the other hand, the spread of electron energy is only ∼0.1%, with a peak energy of ∼1 GeV. The normalized transverse emittances of the FLASH beam are of the order of 1 mm × mrad [74, 117, 118].

In summary, the 6D brightness yields similar numbers $\sim 1 \times 10^{15}\,\mathrm{A/m^2/0.1\%}$, although the individual variables included in it differ greatly in some cases – at a similar emittance, the FLASH beams have a 10 times lower current which is balanced by a 10 times lower energy spread. For the sake of completeness, it should be mentioned that conventional accelerators usually accelerate an entire pulse train, so that significantly higher repetition rates are achieved, from which most applications benefit.

5.6 Summary and significance

The most important result of this chapter is the generation of witness beams with high phase space density. They are spectrally and spatially denser than their respective driving beams and beams from LWFA in a similar energy range.

The emittance estimates of these beams are rather imprecise, as the experiment had no special emittance diagnostic. The PIC simulations are in qualitative agreement with the experimental results. However, they were created as large-scale parameter scans and not as a digital twin of the experiment. Therefore, the emittance of well below 1 mm mrad obtained from the simulations can only be used to estimate the correct order of magnitude.

The divergence of < 0.3 mrad (RMS) is unprecedented for beams in the range of a few 100 MeV. This small divergence may be partly due to an adiabatic phase-space matching between the accelerator and the vacuum. Therefore, the low divergence alone is not suited as a measure for the beam quality. However, there is further evidence for low emittance. The witness spectra with wide energy spread can be understood as a probe for the longitudinal phase space. Beams as in Figure 5.3(d) not only have a very small divergence of ~ 0.3 mrad (RMS), but they also show almost no modulation of the beam divergence along their continuous spectrum. This can be explained by a very small amplitude of the betatron oscillations; otherwise, a situation like in Figure 5.3(c) is to be expected. Here, the envelope of the mismatched phase-space distribution rotates as the betatron phase advances. This rotation depends on the local betatron frequency, i.e., the electron energy and the local plasma density. As a consequence, the varying betatron phase advance is visible as a modulation of the divergence along the

spectrum of the electron bunch.

For applications, the combination of the low divergence after extraction of well below 1 mrad and the energy bandwidth on the ∼1%-level is particularly advantageous. The degradation of the beam due to chromatic beam transport can also be described as an increase in normalized emittance during propagation in free space. Following the description of [119], the evolution of the normalized emittance of a beam with energy spread and divergence is given by $\epsilon_{\mathrm{n,RMS}} = \gamma\sqrt{\sigma_\gamma^2\sigma_{x'}^4(z-z_0)^2 + \epsilon_{\mathrm{RMS}}}$. As the beam divergence has the highest exponent in this equation, it is of particular concern for quality-preserving beam transport. Due to our favorable beam parameters, the emittance growth is only 0.30 mm mrad per 1 m of propagation in free space.

Experiments with low- and high-divergence drivers provide witness beams of comparably high quality. This comparison leads us to expect that the witness quality in our case is limited by the injection process and not by the driver. If necessary for applications, the hybrid scheme promises even higher quality beams when using advanced injection schemes like wakefield-induced ionization injection [47] or a plasma photocathode [45]. In future experiments, an emittance diagnostic should be implemented to clearly determine the actual beam quality. Using the (small but existent) energy spread of the witness, a single-shot measurement using a set of quadrupole magnets is possible [113]. The emittance can be calculated from the energy-dependent focusing of the beam in the dipole spectrometer.

6 Conclusion and Perspectives

6.1 Results of the thesis

Conventional particle accelerators are crucial for scientific progress but are often limited by their size and high costs. Plasma-based acceleration offers a compact and potentially more cost-effective alternative and features two main methods: laser-driven (LWFA) and particle beam-driven plasma wakefield accelerators (PWFA), each with specific limitations and strengths. This dissertation explores a hybrid plasma wakefield accelerator that uses high-current electron bunches from an LWFA to drive a PWFA. This way, the strengths of both types are combined to mitigate their individual limitations and improve the quality of the electron beams generated compared to those from LWFA alone.

LWFA offers unique opportunities for generating high-current drive beams for PWFA in a compact setup. In the scope of this dissertation, high-charge electron bunches are reliably generated via LWFA, with a typical charge of a few 100 pC at energies around 300 MeV. While in previous experiments the controlled internal injection of electrons into PWFA has been a key challenge in hybrid acceleration [29, 40, 42, 43], this work demonstrates two reliable and tunable injection schemes. Initially we employ wire-generated shocks and subsequently enhance the reproducibility of injection by using optically-generated density down ramps, decoupling the properties of the accelerator (plasma target) and the injector. Internal injection into the PWFA is crucial to exploit the full potential of the PWFA in terms of stability and electron bunch quality. The electron beams generated in this work show remarkable improvements over those generated with pure LWFA, as highlighted below.

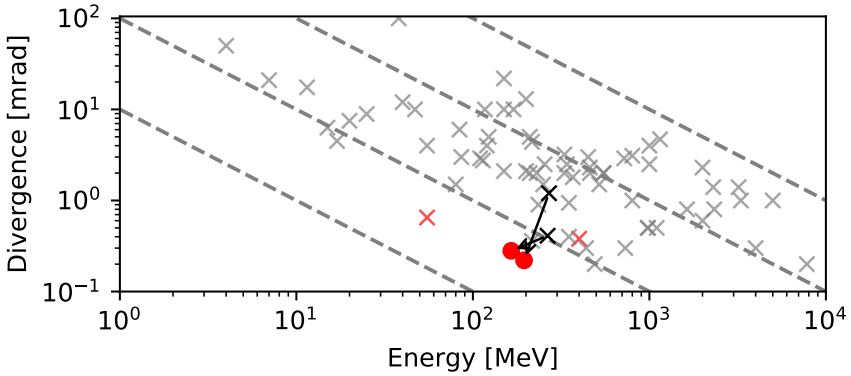

Figure 6.1: ***Divergence of electron beams from plasma accelerators.*** *The plot relates the divergence and energy reported from a large number of LWFA experiments (gray crosses) and PWFA experiments with internal injection (red crosses). The data clusters around lines of constant transverse momentum (gray dashed). The LWFA-generated beams in this work (black crosses) generate witness bunches (red dots) of exceptionally low transverse momentum.*

The stable optical injection scheme and the resilience of PWFA to driver fluctuations result in the production of a **high stability** witness beam, comparably stable

as those from PWFA driven by conventional accelerators [91, 92]. Predictive Particle-in-Cell (PIC) simulations suggest potential for further stability improvements through optimal beam loading. The experimental setup without laser blocker tape achieves exceptionally **low beam divergence**. Figure 6.1 places our hybrid L-PWFA witness beam in the context of other LWFA and PWFA experiments with internal injection and indicates lower transverse momentum and hence superior beam quality. Effective control over the witness charge facilitates reduced energy spread and a **high spectral charge density**, leading to a significantly **enhanced angular spectral charge density** that surpassed that of the drive beam. In this sense, a hybrid L-PWFA can be a quality transformer for applications that demand these electron properties.

The overall energy transfer efficiency from the driver to the witness beam reaches up to 10%, a figure that, to the author's knowledge, represents the highest observed value for PWFA to date. This **high efficiency** is enabled by a high degree of driver depletion observed at an acceleration gradient of up to 157 GV/m. Despite these achievements, the energy gain in the witness beam remains constrained to energies lower than the drivers' energy. Overcoming this limitation and further enhancing the witness beam energy presents an exciting challenge, with several promising research avenues under exploration.

6.2 Future developments

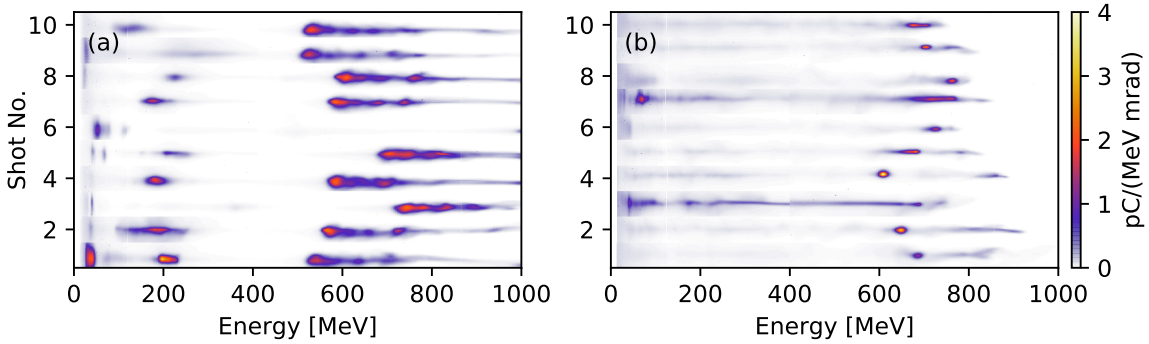

Figure 6.2: ***GeV-class witness acceleration.*** *Using a GeV-class drive beam from LWFA, witness energies of up to* 750 MeV *are generated. Panel (a) shows 10 consecutive LWFA-beams as a driver reference. Panel (b) shows a collection of 10 particularly high-energy witness beams with energies between* 600 *and* 750 MeV*.*

6.2.1 Hybrid with GeV-class drive beams

Following the experiments described so far, another campaign was carried out to show the scalability of the setup. Figure 6.2 shows preliminary results of a PWFA using a GeV-class drive beam from LWFA with a charge of (600 ± 90) pC. In this experiment, the PWFA delivers witness energies of up to 750 MeV using a 13 mm-long gas jet at

a density of approximately $5 \times 10^{18}\,\mathrm{cm}^{-3}$. Please note that, unlike the data presented previously, a Lanex pointing screen was used in this experiment. Therefore, the divergence of these beams cannot be easily compared with the high-quality beams presented in Chapter 5 and summarized in Figure 6.1. In this experiment, the witness energy surpasses the driver's mean peak energy but still remains below its high-energy cut-off. To address this limitation approaches to further boost the witness energy are discussed next.

6.2.2 Higher witness energy gain in PWFA

The hybrid method would be even more promising if the high-quality witness electrons had higher energy than the driver [48]. In particular, this would allow a better separation of the witness beam and the background of the decelerated driver. This goal was almost achieved in the data set shown in the last paragraph and does not appear to be a real obstacle in simulations. However, we assume that some important prerequisites for the highest energy gain have not yet been met, but in the following we outline how this can be achieved in the future.

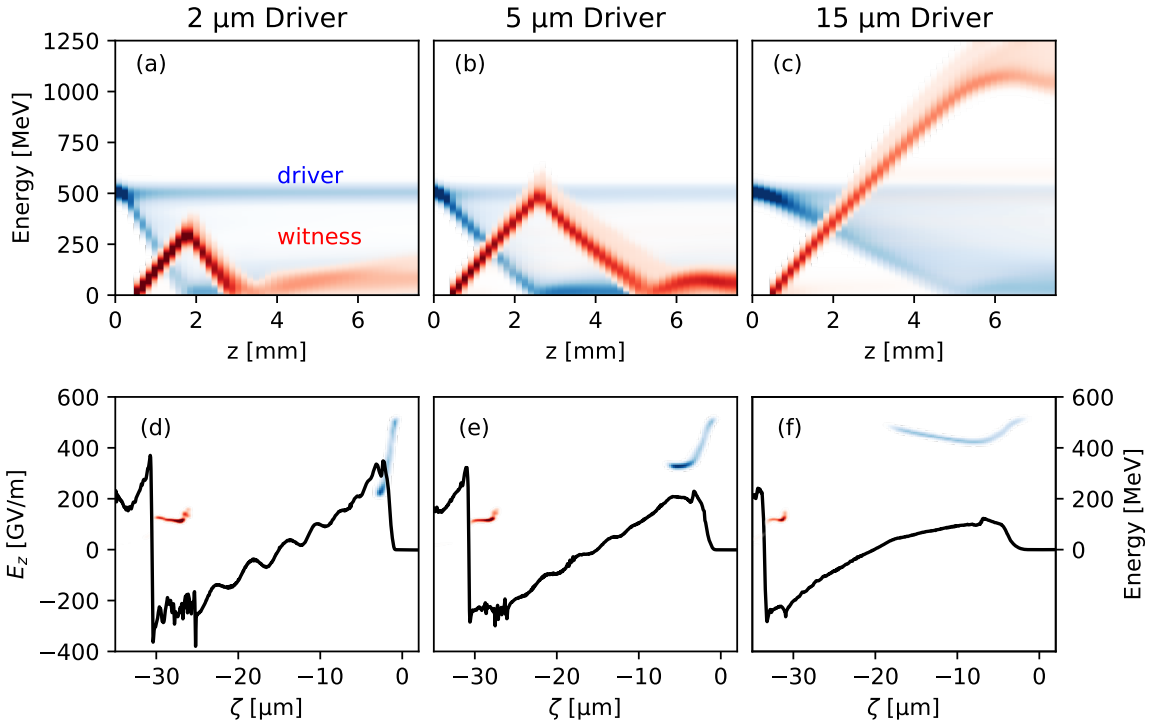

Figure 6.3: ***Different driver length in PWFA*** *Panels (a) to (c) show the evolution of driver and witness spectra for a set of 3 PIC simulations. All drive beams have equal charge of* 500 pC *but different lengths, as indicated. Witness beams are injected at a density down ramp. The background density is* $2.5 \times 10^{18}\,\mathrm{cm}^{-3}$. *Panels (d) to (f) show the longitudinal wakefield and the phase space of the driver and witness. These are snapshots at z=1 mm of the simulations above.*[1]

The influence of the driver current

The space-charge field of the driver and, therefore, the wakefield excitation depends on its current (see also the model in Section 1.3.3). To analyze this dependence, a set of PIC simulations with different driver currents under otherwise identical conditions was performed (see Fig. 6.3). All drive beams have a rectangular current profile and an integrated bunch charge of 500 pC. They only differ in terms of their bunch length. While the acceleration fields in the back half of the bubble are almost independent of the driver current, the amplitude and the slope of the decelerating field seen by the driver vary depending on the bunch length. For a bunch filling approximately half of the bubble, the lowest positive field amplitude and the flattest field distribution over the length of the driver are obtained (Fig. 6.3f). In this case, the wakefield can be driven for a longer distance. Consequently, the witness reaches the highest energy (Fig. 6.3c). In this simulation, it approximately doubles the driver energy.

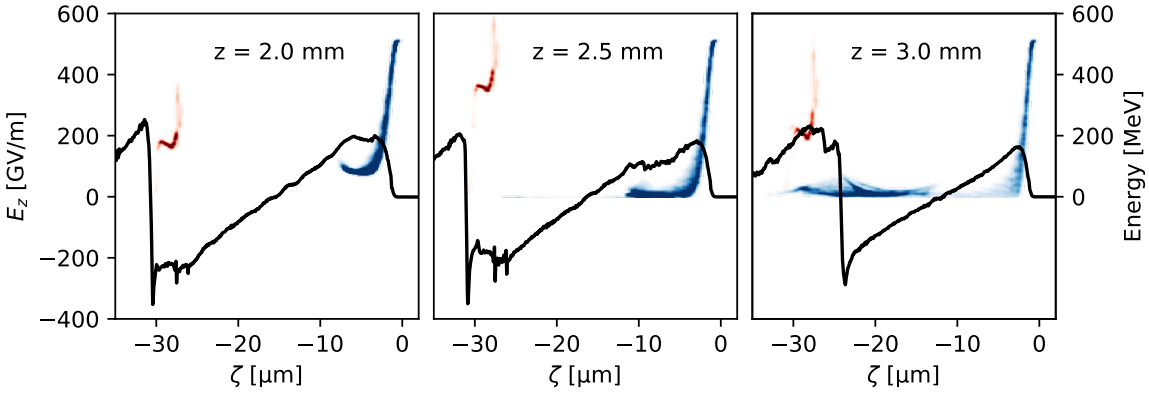

Figure 6.4: ***Witness slipping out of the first bubble.*** *The longitudinal wakefield is plotted together with the phase space of the driver and witness for different time steps from Fig. 6.3(b). When the driver bunch breaks up due to deceleration, the witness slips into the decelerating phase of the second bubble.*[1]

In contrast, for a shorter driver, a small longitudinal portion of the driver sees the highest decelerating field. Some electrons will fall back as soon as this part of the beam is fully decelerated. From this point onward, the driver will set up a weaker wakefield. Moreover, even worse, the decelerated driver electrons load the accelerating part of the bubble and further decrease the fields seen by the actual witness (see Fig. 6.4). While the driver breaks up, the length of the first cavity shrinks. Eventually, the witness even slips out of the first bubble and ends up in the decelerating phase of the second bubble.

The length of an LWFA-generated electron bunch depends on the plasma density and the injection method. For a given experimental setup, it is not easily varied. However, the excitation of the PWFA depends on the bunch length relative to the bubble size. This ratio can be easily adjusted by changing the density in the PWFA. As higher densities also entail higher decelerating gradients, the length of the target

[1]These PIC simulations are reproduced by kind permission of Dr. Johannes Zirkelbach.

needs to be shortened accordingly. Also, the injected charge will likely increase with increasing plasma density, limiting the achievable energy gain. Therefore, a multi-dimensional optimization of plasma density, target length, and down ramp for injection will be necessary to obtain the highest possible witness energy.

In simulations, more advanced current shapes can be found to optimize the energy gain of the witness [120]. Unfortunately, the experimental generation of such current profiles is non-trivial. Variations of the density down ramp height and length in an LWFA stage proved to influence the current of the injected beam in simulations [104]. However, further extensive studies, both experimentally and in simulations, are necessary to optimize the driver current for the highest energy gain in PWFA and to propose a viable scheme for generating these drivers.

A plasma lens between LWFA and PWFA

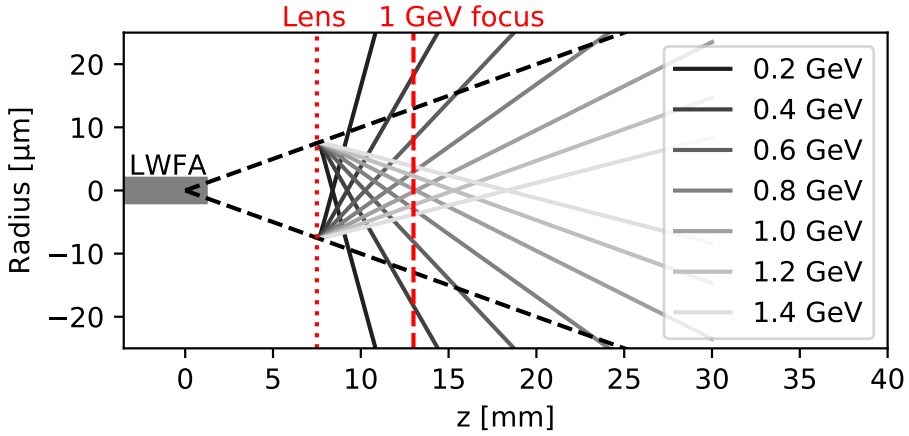

Figure 6.5: ***Schematic of the energy-dependent focusing of a plasma lens for LWFA-generated electrons.*** *Electrons diverge at an angle of 1 mrad from the LWFA source. 7.5 mm downstream a* $300\,\mu$m*-wide plasma lens at a density of* $1 \times 10^{17}\,\mathrm{cm}^{-3}$ *refocuses the electrons. The calculation assumes the focusing force of a homogeneous ion column.*

Another approach to increase witness energy gain could be to use a plasma lens between LWFA and PWFA. As seen in Section 4.4.1, the drive beam's transverse phase space is not matched to the local betatron trajectories when entering the PWFA stage, and its full potential to drive a strong wakefield is not used. A plasma lens between both acceleration stages can refocus the diverging drive beam and mitigate the emittance growth resulting from driver mismatch.

A further benefit of a plasma lens is its chromaticity. The lens focuses electrons at the target energy and, at the same time, defocuses the low-energy part of the driver spectrum (see Fig. 6.5). As discussed before, early depletion of parts of the driver limits the achievable witness energy. A plasma lens can mitigate the problem of early depletion if low-energy electrons are defocused strongly and are not captured in the PWFA.

6.2.3 Better diagnostics

In the course of our experiments, the characterization of electron bunches was predominantly reliant on data acquired from the dipole spectrometer. However, this method offers only a partial glimpse into the complex 6-dimensional phase space of electrons, leaving crucial aspects of the beam quality unexplored. Furthermore, the absence of comprehensive information regarding the driver's phase space poses a significant challenge for running realistic Particle-In-Cell simulations. Critical parameters such as the driver's current profile and transverse emittance remain elusive, impeding the fidelity of our simulations and limiting our ability to accurately model experimental outcomes. Diagnostics for the beam's current and emittance, which are briefly presented below, have been implemented in the past [25, 113] and should be included in future hybrid L-PWFA experiments.

The temporal bunch profile and, in particular, its pulse length τ_p can be reconstructed from the spectrum of transition radiation (TR). TR is produced when the electron bunch passes through the boundary of media with different dielectric indices. Spectral portions of wavelength λ_{TR}, for which $\lambda_{TR}/c > \tau_p$ are radiated coherently (CTR) and the associated increase in spectral intensity can be measured. Meanwhile, a CTR diagnostic setup was rebuilt in ETTF. It consists of a steel tape a few cm behind the target used as a radiator, imaging optics, and three spectrometers covering the complete spectral range from the visible to the mid-infrared.

For measuring the beam emittance, one can use the non-negligible energy spread of the electron bunches. A set of miniature quadrupole magnets focuses the beam into the plane of the dipole spectrometer. As the magnets are chromatic, only one energy will be perfectly focused. The emittance of the bunches can be retrieved from the energy-resolved transverse envelope measured in the dipole spectrometer. Emittance measurements would be particularly interesting in combination with Trojan horse injection [45], which promises unprecedented low emittance. For Trojan horse injection, however, the drive and injector beams must be overlapped with μm spatial and fs temporal precision. The ATLAS3000 laser system's current level of pointing jitter does not meet these requirements and calls for active beam stabilization for future experiments. As part of the Hybrid-collaboration, Trojan horse injection experiments have been successfully carried out at HZDR [unpublished]. In contrast to the theoretical proposal [45], however, a transverse injection beam with a wide focus (larger than the diameter of the wakefield) is used in these experiments, which reduces the requirements on the pointing stability of the laser, but at the price of a higher expected beam emittance.

6.3 Applications for beams from hybrid L-PWFA

The witness beams from hybrid L-PWFA, as presented in this dissertation, exhibit a unique combination of high energy stability, low energy spread, and low divergence, making them particularly well-suited for light source applications. Below, we briefly discuss experiments that leverage these exceptional properties.

Using a part of the Ti:Sa laser as a beam for scattering, quasi-monochromatic hard x-rays can be produced via Thomson-scattering [121]. The tunability of the witness energy between several tens and hundreds MeV enables the generation of adjustable x-ray energies in the hundred keV range, which is relevant for medical imaging applications.

For free electron lasers (FELs), the electron beam must overlap spatially and temporally with the light field in the undulator. For this reason, the low-emittance, low-energy spread beams from the hybrid L-PWFA can be helpful. Breakthroughs in driving FELs with LWFA-generated beams have recently been reported [122, 123]. These results, as well as theoretical work [124–127], showed that already minor improvements beyond the performance of current plasma-based accelerators could be very beneficial. In particular, FEL applications typically require beam transport between the accelerator stage and the undulator. Here the unprecedentedly low divergence of the witness beam at moderate energies of $\sim 100\,\mathrm{MeV}$ becomes essential. These beams can be transported in a magnetic quadrupole beam line with minimal emittance degradation [114, 119]. Thus, they promise shorter gain lengths and higher saturation power than typical beams from pure LWFA.

In the long term, hybrid L-PWFA might also apply to high-energy plasma accelerators. Proposed schemes usually require many acceleration stages to reach energies in the range of tens to hundreds of GeV [128]. At the same time, the coupling of the electrons between consecutive stages is likely connected to a decrease in beam quality [129]. The problem of beam degradation can be mitigated by a final PWFA stage with internal witness injection after a multi-stage LWFA. In this scheme, the energy of the electron beam is continuously increased in the LWFA stages, while the quality of the witness electron bunch will be determined by the injection and acceleration in the final PWFA stage only. This work's high energy transfer efficiency of the PWFA stage encourages further research in this direction.

Appendix A

Parameter sets for PIC simulations

A.1 Input parameters of PIC simulations

The simulations used a lab-frame resolution of $\Delta z = 50\,\mathrm{nm}$, $\Delta r = 200\,\mathrm{nm}$, $m = 3$ modes, a boosted frame [130] with $\gamma_{boost} = 10$ and a particle density of $n_z \times n_r \times n_\theta = 10 \times 4 \times 16$ within the injection region. The drive beam and plasma electrons making up the witness beam were initiated as two distinct species and could thus be separated in post-processing. The electron beam had a normally-distributed phase space, with a bunch length $c\sigma_t = 3.5\,\mu\mathrm{m}$, a radius $\sigma_r = 5\,\mu\mathrm{m}$ and a normalized emittance of $\epsilon_n = 1\,\mathrm{mm\,mrad}$. For our reference case, the central beam-energy was $E_0 = 287\,\mathrm{MeV}$, the energy spread $\sigma_E/E_0 = 10\%$, and the beam-charge $Q_0 = 340\,\mathrm{pC}$. For the results presented in Section 4.3, these parameters were varied according to the charge and energy fluctuations from the experiment by sampling a normal distribution centered around Q_0 and E_0, respectively. The density profile used for the PIC simulations is shown and discussed in detail in Figure 4.3.

A.2 Example input deck for PIC simulation

In the following, a complete FBPIC input file for simulating the PWFA stage is given. Short explanations of the key parameters are given as comments directly in the Python code.

```
#--------
# imports
#--------

import matplotlib.pyplot as plt
from openpmd_viewer import *
from openpmd_viewer.addons import LpaDiagnostics
from scipy.ndimage.filters import gaussian_filter
import numpy as np
from numpy import sqrt

#------------------------
# definition of a function used to run PIC simulations for varying
    driver energy and charge
#------------------------
def PIC(energy,charge):
    # -------
    # Imports
    # -------
    from scipy.constants import c, e, m_e, m_p

```

```
21  # Import the relevant structures in FBPIC
22  from fbpic.main import Simulation
23  from fbpic.lpa_utils.bunch import add_particle_bunch_gaussian
24  from fbpic.openpmd_diag import FieldDiagnostic,
    ParticleDiagnostic, set_periodic_checkpoint,
    restart_from_checkpoint
25  from fbpic.lpa_utils.boosted_frame import BoostConverter
26  from fbpic.openpmd_diag import FieldDiagnostic,
    ParticleDiagnostic, BackTransformedFieldDiagnostic,
    BackTransformedParticleDiagnostic
27  import numpy as np
28  import scipy
29  import scipy.io as sio
30  import scipy.constants as const
31  import scipy.interpolate as interpolate
32
33
34  # -------
35  # Target Scan Parameters
36  # -------
37
38  n_e = 2e24 #the peak density of the PWFA target
39
40  # -------
41  # Basic functions and parameters
42  # -------
43
44  def lambda_p(n_e):
45      return(2*np.pi*const.c*np.sqrt(const.m_e*const.epsilon_0/(
    const.e**2*n_e)))
46
47  def k_p(n_e):
48      return(1./(const.c*np.sqrt(const.m_e*const.epsilon_0/(const.e
    **2*n_e))))
49
50  def n_elec(lambda_p):
51      return((2*np.pi*const.c/lambda_p)**2*(const.m_e*const.
    epsilon_0/(const.e**2)))
52
53  n_c = n_elec(0.8e-6)
54
55  # ----------
56  # Parameters
57  # ----------
58
59  # Whether to use the GPU
60  use_cuda = True
61  n_order = -1
62
63  # The simulation box
64  zmax = 0.e-6      # Right end of the simulation box (meters)
65  zmin = -45e-6     # Left end of the simulation box (meters)
66  dz = 50e-9        # lab-frame resolution in z
67  Nz = int(np.abs(zmin)/dz)
```

```
68      rmax = 30e-6
69      dr0 = 200e-9      # lab-frame resolution in r
70      Nr = int(rmax/dr0)  # Number of gridpoints along r
71      dr = rmax/Nr
72      Nm = 3            # Number of modes used
73
74      # The particles
75      p_zmin = 0.e-6    # Position of the beginning of the plasma (
        meters)
76      p_zmax = 4e-3     # Position of the end of the plasma (meters)
77      p_rmin = 0.       # Minimal radial position of the plasma (meters)
78      p_rmax = rmax     # Maximal radial position of the plasma (meters)
79      p_nz = 4          # Number of particles per cell along z
80      p_nr = 2          # Number of particles per cell along r
81      p_nt = 12         # Number of particles per cell along theta
82                        # Resolution in injec. region will be redefined
83
84      # Boosted frame
85      l_window = zmax-zmin
86      l_sim = p_zmax-p_zmin
87      gamma_boost = np.floor(np.sqrt(l_sim/l_window))
88      if gamma_boost > (np.sqrt(n_c/n_e)/3):
89          gamma_boost = (np.sqrt(n_c/n_e)/3)
90      print(gamma_boost)
91
92      # Boosted frame converter
93      boost = BoostConverter(gamma_boost)
94
95      # The simulation timestep
96      # (See the section Advanced use > Running boosted-frame
        simulation
97      # of the FBPIC documentation for an explanation of the
        calculation of dt)
98      dt = min( rmax/(2*boost.gamma0*Nr)/c, (zmax-zmin)/Nz/c )  #
        Timestep (seconds)
99
100     # ----------
101     # The Beam
102     # ----------
103
104     # The bunch
105     sig_r = 5e-6 #rms radius of drive beam [m]
106     sig_z = 3.5e-6 #rms length of drive beam [m]
107     n_emit= 1e-6 #norm. emittance of beam [m]
108     print(energy)
109     gamma0 = energy/0.511
110
111     sig_gamma = 0.1*gamma0 #10% energy spread of drive beam
112     n_physical_particles = charge*1e-12/e
113     n_macroparticles = 50000
114
115
116
117
```

```
118     # ----------
119     # The Density Profile
120     # ----------
121
122     z_inj = 1500e-6
123
124     # jet: definition of the trapezoidal density profile
125     z_long_profile = [0,50e-6,1.8e-3,2.2e-3,4e-3]
126     n_long_profile = [0,0   ,1. ,1   ,0.]
127     # adjust length scales
128     z_long_profile = boost.static_length( z_long_profile )
129     g = interpolate.interp1d(z_long_profile, n_long_profile ,
        bounds_error=False)
130
131
132     #definition of the M-shaped density perturbation
133     z_shock_profile = [0,50e-6,100e-6,z_inj,z_inj+50e-6, z_inj+100e
        -6,z_inj+150e-6,z_inj+200e-6,3.4e-3,5e-3]
134     n_shock_profile = [0,0,0,0,0.5,-0.5,0.5,0,0,0]
135     # adjust length scales
136     z_shock_profile = boost.static_length( z_shock_profile )
137     h = interpolate.interp1d(z_shock_profile, n_shock_profile ,
        bounds_error=False)
138
139     zz = np.linspace(0,5e-3,5000)# Sum of unperturbed density and
        shock
140     f = interpolate.interp1d(zz, g(zz)+h(zz) ,bounds_error=False)
141
142     #Next distinct zones in radial and longitudinal coordinates are
        defined. This is used to later initialize the plasma in the
        injection region with higher resolution.
143     position_transv = [0, 18.0e-6, 19.0e-6, 1]
144     dens_trans = [1,1,0,0.]
145     f_transv = interpolate.interp1d(position_transv, dens_trans,
        bounds_error=False)
146
147     position_transv2 = [0, 32e-6, 35.0e-6, 1]
148     dens_trans2 = [1,1,0,0.]
149     f_transv2 = interpolate.interp1d(position_transv2, dens_trans2,
        bounds_error=False)
150     position_inj = [0, z_inj-gamma_boost*1e-6, z_inj, z_inj+300e-6,
        z_inj+300e-6+gamma_boost*1e-6, 1]
151
152     position_inj = boost.static_length(position_inj)
153
154     dens_inj = [0,0,1,1,0,0]
155     f_inj = interpolate.interp1d(position_inj, dens_inj,bounds_error=
        False)
156
157     # density functions for individual macro particle species
158
159     def dens_func_inner( z, r ) :
160         n=f(z)*f_transv(r)*f_transv2(r)
161         return(n)
```

```
162
163     def dens_func_outer( z, r ) :
164         n=f(z)*(1-f_transv(r))*f_transv2(r)
165         return(n)
166
167     def dens_func_injection( z, r ) :
168         n=dens_func_inner(z,r)*f_inj(z)
169         return(n)
170
171     def dens_func_no_injection( z, r ) :
172         n=dens_func_inner(z,r)*(1-f_inj(z))
173         return(n)
174
175
176     # The moving window (moves with the group velocity in a plasma)
177     v_window = c*( 1 - 0.5*n_e/n_c )
178
179     # Velocity of the Galilean frame (for suppression of the NCI)
180     v_comoving = - c * np.sqrt( 1. - 1./boost.gamma0**2 )
181
182
183     # The interaction length of the simulation, in the lab frame (
    meters)
184     L_interact = (p_zmax-p_zmin) # the plasma length
185     # Interaction time, in the boosted frame (seconds)
186     T_interact = boost.interaction_time( L_interact, (zmax-zmin),
    v_window )
187     # (i.e. the time it takes for the moving window to slide across
    the plasma)
188
189     ## The diagnostics
190
191     # Number of discrete diagnostic snapshots, for the diagnostics in
     the
192     # boosted frame (i.e. simulation frame) and in the lab frame
193     # (i.e. back-transformed from the simulation frame to the lab
    frame)
194     N_boosted_diag = 1+1
195     N_field_diag = 10+1
196     N_lab_diag = 120+1
197     # Time interval between diagnostic snapshots *in the lab frame*
198     # (first at t=0, last at t=T_interact)
199     dt_lab_diag_period = (L_interact + (zmax-zmin)) / v_window / (
    N_lab_diag - 1)
200     dt_lab_diag_period_fields = (L_interact + (zmax-zmin)) / v_window
     / (N_field_diag - 1)
201
202     # Time interval between diagnostic snapshots *in the boosted
    frame*
203     dt_boosted_diag_period = T_interact / (N_boosted_diag - 1)
204
205     # Whether to tag and track the particles of the bunch
206     track_bunch = False
207
```

```
208     # ---------------------------
209     # Carrying out the simulation
210     # ---------------------------
211
212     # NB: The code below is only executed when running the script,
213     # (`python -i lpa_sim.py`), but not when importing it (`import
        lpa_sim`).
214     if __name__ == '__main__':
215
216         # Initialize the simulation object
217         sim = Simulation( Nz, zmax, Nr, rmax, Nm, dt, zmin=zmin,
218             v_comoving=v_comoving, gamma_boost=boost.gamma0,
219             n_order=n_order, use_cuda=use_cuda,
220             boundaries={'z':'open', 'r':'open'})
221
222         #Adding different electron species
223         elec        = sim.add_new_species( q=-e, m=m_e, n=n_e,
224                                            dens_func=
        dens_func_injection,
225                                            p_nz=int(np.ceil(
        gamma_boost)), p_nr=4, p_nt=16)
226             #These are the electrons in the injection region with
        higher particle density
227
228
229         elec_no_inj = sim.add_new_species( q=-e, m=m_e, n=n_e,
230                                            dens_func=
        dens_func_no_injection,
231                                            p_nz=1, p_nr=2, p_nt=16)
232
233         elec_out    = sim.add_new_species( q=-e, m=m_e, n=n_e,
234                                            dens_func=dens_func_outer,
235                                            p_nz=1, p_nr=1, p_nt=16)
236
237         plasma_ions_inner = sim.add_new_species( q=e, m=m_p, n=n_e,
238         dens_func=dens_func_injection,
239                         p_zmin=p_zmin, p_nz=int(np.ceil(gamma_boost))
        , p_nr=4, p_nt=16)
240
241         plasma_no_inj     = sim.add_new_species( q=e, m=m_p, n=n_e,
242         dens_func=dens_func_no_injection,
243                         p_nz=1, p_nr=2, p_nt=16, p_zmin=p_zmin)
244
245
246         plasma_ions_outer = sim.add_new_species( q=e, m=m_p, n=n_e,
        dens_func=dens_func_outer, p_zmin=p_zmin, p_nz=1, p_nr=1, p_nt=16)
247
248
249         driver = add_particle_bunch_gaussian( sim,-e, m_e, sig_r,
        sig_z, n_emit, gamma0, sig_gamma, n_physical_particles,
        n_macroparticles, boost=boost, tf=0, zf=-12e-6)
250
251
252
```

```
253         # Convert parameter to boosted frame
254         v_window_boosted, = boost.velocity( [ v_window ] )
255         # Configure the moving window
256         sim.set_moving_window( v=v_window_boosted )
257
258         N_step = int(T_interact/sim.dt)+1
259         write_period = int(np.floor(T_interact/sim.dt/20))
260
261         #define path name for saving
262         write_dir          = "{:.3f}".format(energy)+'_'+"{:.3f}".
    format(charge)
263         write_dir_particle = 'particle_diags_' + write_dir
264         write_dir_field    = 'field_diags_'    + write_dir
265
266         sim.diags = [BackTransformedFieldDiagnostic( zmin, zmax,
    v_window,
267                         dt_lab_diag_period_fields, N_field_diag,
    boost.gamma0,
268                         fieldtypes=['rho','E'], period=write_period,
269                         write_dir=write_dir_field, fldobject=sim.fld,
     comm=sim.comm ),
270                       BackTransformedParticleDiagnostic( zmin, zmax,
    v_window,
271                         dt_lab_diag_period, N_lab_diag, boost.gamma0,
272                         write_period, sim.fld, select={'uz':[10.,None
    ]},
273                         species={'electrons':elec,'other':elec_no_inj
    , 'driver':driver},
274                         comm=sim.comm ,write_dir=write_dir_particle)]
275
276         ### Run the simulation
277         sim.step( N_step )
278
279     particle_path = write_dir_particle +'/hdf5/'   # defines where to
     write particle diag.
280     field_path = write_dir_field +'/hdf5/'         # defines where to
     write field diag.
281     return(particle_path,field_path)
282
283 PIC(287,340)    # This command runs the function defined above for a
    driver with a peak energy of 287 MeV, and a charge of 240 pC
```

Appendix B

Calibration of the dipole spectrometer

TAKE-HOME MESSAGE

When I started analyzing electron data, there were several issues with the charge calibration used in ETTF. This appendix documents my efforts to optimize the charge calibration of the electron spectrometer. This summary is also a concise tutorial for future generations. However, it neither covers the entire theory of charge calibration (see paper, e.g., [94, 95]) nor is it the final answer to everything. Everyone analyzing data from the dipole spectrometer is highly encouraged to go through the calibration process on their own.

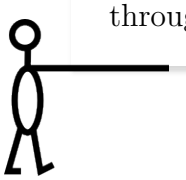

B.1 Charge calibration procedure

Let me first remind you of the charge calibration protocol. It is a multi-step process:

1. The Dresden Master light source (MLS) was once calibrated using the ELBE accelerator. The brightness of different Lanex screens and the MLS, imaged with the same imaging system, was compared. From this measurement, a proportionality between the brightness of the MLS and the known amount of charge impinging onto the Lanex screen was derived.

2. The Munich MLS is cross-calibrated with the Dresden MLS. Both MLSs are imaged using the same imaging system. The integrated intensity is divided by each other. This factor is multiplied by the numbers derived in step 1.

3. The Munich gaseous Tritium light source (GTLS) is cross-calibrated with the Munich MLS. Both MLS and GTLS are imaged using the same imaging system. A proportionality between the specific GTLS and the charge impinging onto the Lanex (see step 1) is derived from this.

4. In the experiment, we compare the brightness of one specific GTLS with the Lanex used in the experiment. Therefore, we can indirectly compare the charge impinging onto our Lanex with the known charge from the ELBE accelerator (see step 1).

5. Some correction factors are applied to the light yield of the Lanex to account for the non-perpendicular intersection of the electron beam, observation angle, and variation of observation distance.

All calculations in the above steps are related to some uncertainty. Most of the points above were also subject to systematic errors, which were partly ruled out during the scope of this thesis. The results of the analysis are presented in the following.

B.2 Recalibration of MLS

The concept and setup of the MLS can be found in Kurz's Master thesis [96][available on AG Karsch network drive].

Due to significant concerns regarding the accuracy of the charge calibration procedures previously employed in Munich, I undertook a trip to Dresden in August 2021 to perform a comparative cross-calibration of our MLS with the system operated by the Dresden team. This recalibration effort assumes a correct calibration of the Dresden MLS, i.e., the correctness of the numbers from step 1 above. During the course of this visit, both MLS systems were imaged under identical conditions to ensure comparability. An area of interest around the aperture of the integrating spheres was defined and the respective px-counts were integrated and divided by each other. This calculated ratio was then utilized as a conversion factor to use the Dresden calibration for our MLS, aiming to enhance the precision of charge calibration across both locations.

The new calibration values are found below in this appendix's last section.

B.2.1 Issues with Munich MLS: Inhomogeneous source.

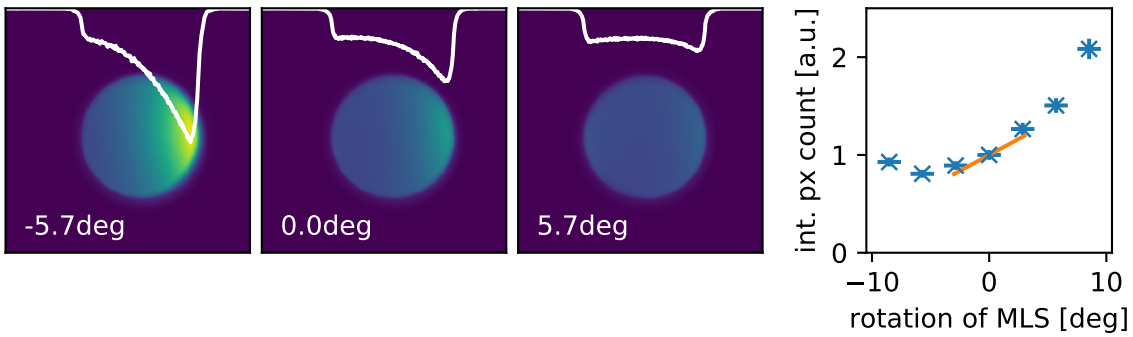

Figure B.1: ***MLS under varying observation angles.*** *The MLS only insufficiently diffuses the light of the internal LED. Both the emission shape and the integrated signal vary with the observation angle.*

Figure B.1 shows the Munich MLS imaged from 20 cm away. The MLS was rotated in the range of a few degrees. It is visible that the gradient among the aperture of the light source strongly depends on the angle. The white lineout is a section through the center of the aperture. Also, the integrated pixel count strongly varies with the angle, as seen in the right subplot.

The linear fit at the nominal position of 0° tells us that 1 degree misalignment corresponds to a deviation in pixel count of 6%. The actual error during the calibration of the Munich MLS should be below this value of 6% because a misalignment of 1 degree is already quite well visible in terms of the steepness of the gradient and can be avoided. Therefore, I expect an uncertainty of a few percent to be added in this step.

B.2.2 Issue: Diffuser plate for Munich MLS

The insufficient ability of the Ulbricht sphere used in the Munich MLS to create diffuse radiation was noticed before. People started using an external diffuser plate in front of the MLS. The diffuser helps to make the radiation less angle-dependent, but it adds new problems. In the case with diffuser glass, the source area is not very easy to determine since the whole glass plate is faintly glowing. This behavior contrasts to the Ulbricht sphere alone, where only the well-defined aperture sends out light. In perspective, I suggest building a proper integrating sphere (maybe using Dresden design) and redoing the cross-calibration.

B.2.3 Crosscalibration of MLS and GTLS

For practical reasons, I replaced the camera in the black MLS/GTLS calibration box with a Basler cam (ac750) in Autumn 2021. The previously used Point Grey Grasshopper always had Ethernet connection problems, and even worse, it kept returning to its default values after each power cycle. In particular, this meant that gamma was enabled by default.

Exposure time issue

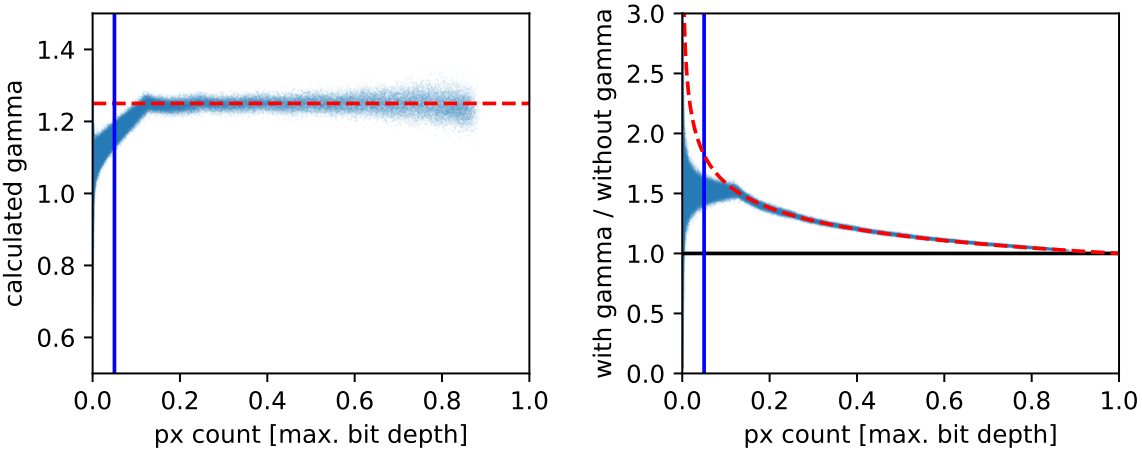

Figure B.2: ***Gamma correction of a Point Grey Grasshopper camera.*** *The same MLS was imaged both with and without gamma enabled. Afterward, a pixel-wise analysis was done. The left plot shows the actual gamma retrieved from the data as a function of the px count. The nominal gamma was 1.25 (red dashed line). The right plot shows the quotient of images with gamma and without gamma. The red dashed line corresponds to the case of a mathematical implementation of gamma of 1.25. In both plots, the blue vertical line corresponds to the pixel count of the tritium capsule in the old measurement protocol.*

In the past (until Autumn 2021), the calibration in Munich was done by imaging the MLS and the tritium capsule at the same time and thus with the same exposure time. The MLS is brighter by roughly two orders of magnitude, which leads to very

different px values for both sources. We must, therefore, assume perfect linearity of the CCD in order to compare the two numbers. Even though this assumption may be justified, things get complicated when gamma comes into play. For a long time it was not noticed that gamma correction was activated by default in the camera previously used. While this problem should now be solved with a different camera model, the gamma issue is briefly explained here for educational reasons.

In principle, the px values of an image with gamma can be corrected afterward. However, it seems that the gamma is not implemented as a mathematical operation on the data but happens before the pixels are read out and digitized. For pixel counts smaller than 10% of the maximum bit depth, the values deviate quite substantially from the expected scaling. For the data shown in Figure B.2, the same MLS was imaged both with and without gamma enabled. Afterward, a px-wise analysis was done. The left plot shows the actual gamma retrieved from the data as a function of the px count. The nominal gamma was 1.25, confirmed for px-counts larger than 0.1 * max. Bit depth. The right plot shows the quotient of images with gamma and without gamma. The red dashed line corresponds to the case of a mathematical implementation of a gamma of 1.25. In both plots, the blue vertical line corresponds to the px. count of the tritium capsule in the old measurement protocol. The severe deviation from the expected gamma scaling is apparent.

In any way, I recommend taking images of MLS and GTLSs in identical geometry, in close temporal proximity, but at different exposure times. Afterward, the data is normalized with the known exposure time. This procedure is beneficial in terms of signal-to-noise ratio and is also how they do it in Dresden.

B.2.4 Tritium capsule glow issue

As noticed during my calibration tests, the light yield from the GTLS's phosphor is influenced by its previous exposure to ambient light (torch light). There is a typical decay time on the order of minutes. Thus, one should wait a few minutes after putting the tritium capsule into the black box for calibration. The light yield changes by a few percent only and, therefore, by much less than the uncertainty of the charge calibration. However, it is worth to avoid this additional error source. I can not remember if this was done in the past.

B.3 Light yield of Lanex screens

How does the number of detected photons in the dipole spectrometer relate to the number of electrons impinging on the scintillating screen?

B.3.1 Radiation characteristic of the scintillating screen and observation angle

So far, no dedicated experiment to measure the radiation characteristic of a Lanex screen has been done in CALA. For now, it is approximated assuming a Lambertian

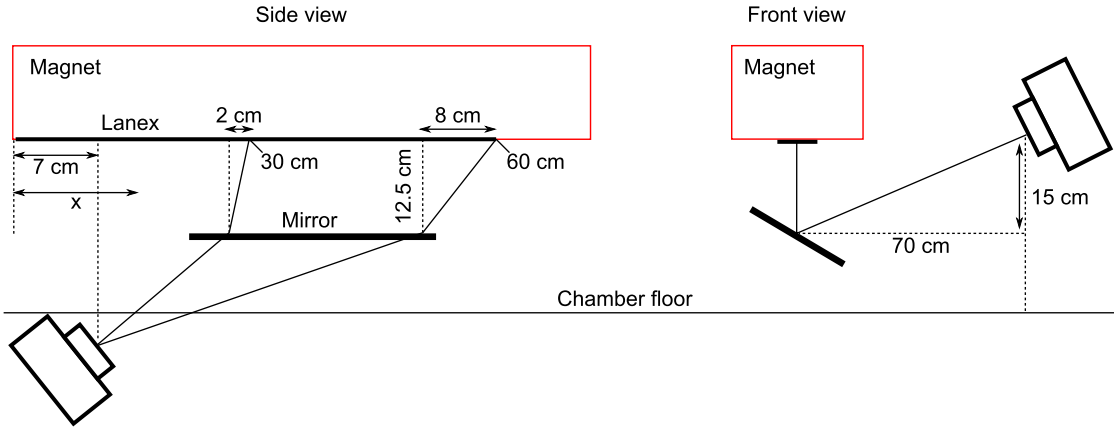

Figure B.3: ***Position of camera relative to scintillating screen.*** *The variation of observation angle and distance as a function of the position along the magnet can be deduced.*

radiation characteristic, as suggested by Kurz [94] and references therein [131, 132].

The influence of the angle-dependent radiation will be exemplified using the imaging geometry of the 100-400 MeV range of the dipole spectrometer in ETTF. The observation angle β relative to the surface normal of the lanex can be deduced from the imaging geometry shown in Figure B.3. From the observation angle, the relative number of photons per solid angle in the direction of the camera can be calculated for each position x along the Lanex screen.

$$\#\text{detected photons} \propto \cos(\beta) = \cos\left(\arctan\left(\frac{x - 7\,\text{cm}}{84\,\text{cm}}\right)\right) \tag{B.1}$$

B.3.2 Influence of varying distance between scintillating screen and camera aperture

The ETTF chamber dictates some geometrical constraints for arranging cameras looking onto the Lanex screen. Positions along the magnet imaged by one camera can not be assumed to be equidistant to the camera aperture. Thus, the variation in the captured solid angle must be considered. A quadratic drop of collected photons as a function of the distance D is assumed. The curve is normalized to the distance D_0 of the tritium capsule used for reference.

$$\#\text{detected photons} \propto \frac{D_0^2}{D^2} = \frac{D_0^2}{84\,\text{cm}^2 + (x - 7\,\text{cm})^2} \tag{B.2}$$

B.3.3 Influence of non-perpendicular intersection of electrons and scintillating screen

Figure B.4 shows a schematic sketch of an electron trajectory in and below the magnet. From geometric considerations, the intersection angle alpha is given as:

$$\alpha = 2 \cdot \arctan(11\,\text{cm}/x)\,, \tag{B.3}$$

where 11 cm is the beam height of the electrons relative to the magnet's lower face, and x is the position along the magnet as defined previously.

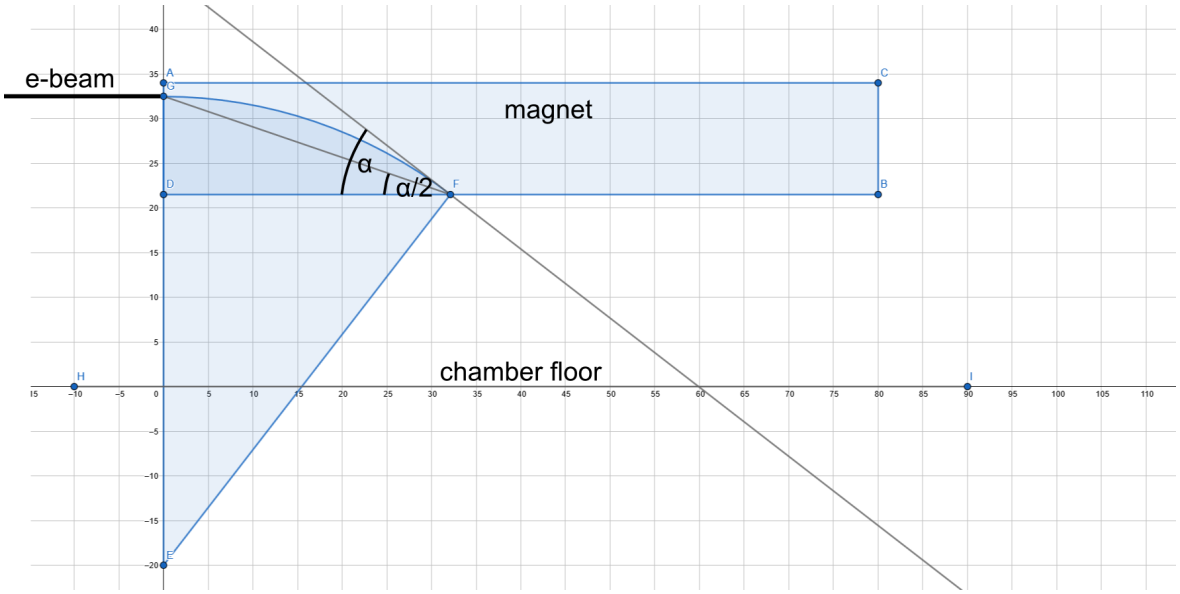

Figure B.4: ***Intersection angle of electron beam and scintillating screen.***

According to Kurz et al. Rev. Sci. Instrum. (2018) the light yield for a given charge scales as $1/\sin(\alpha)$, since the effective interaction length inside the active layer of the scintillator is elongated by this factor:

$$\#\text{detected photons} \propto 1/\sin(\alpha) = 1/\sin\left(2 \cdot \arctan\left(11\,\text{cm}/x\right)\right) \tag{B.4}$$

The three effects discussed previously can be summarized in one correction factor:

$$\begin{aligned}\text{correction factor} = \cos&\left(\arctan\left(\frac{x - 7\,\text{cm}}{84\,\text{cm}}\right)\right) \\ &+ \frac{D_0^2}{84\,\text{cm}^2 + (x - 7\,\text{cm})^2} \\ &+ 1/\sin\left(2 \cdot \arctan\left(11\,\text{cm}/x\right)\right),\end{aligned}$$

where the constants in this equation must be adjusted each time the imaging setup is changed. The following plot shows the expected enhancement of the light yield due to the effects described above as a function of the position along the magnet:

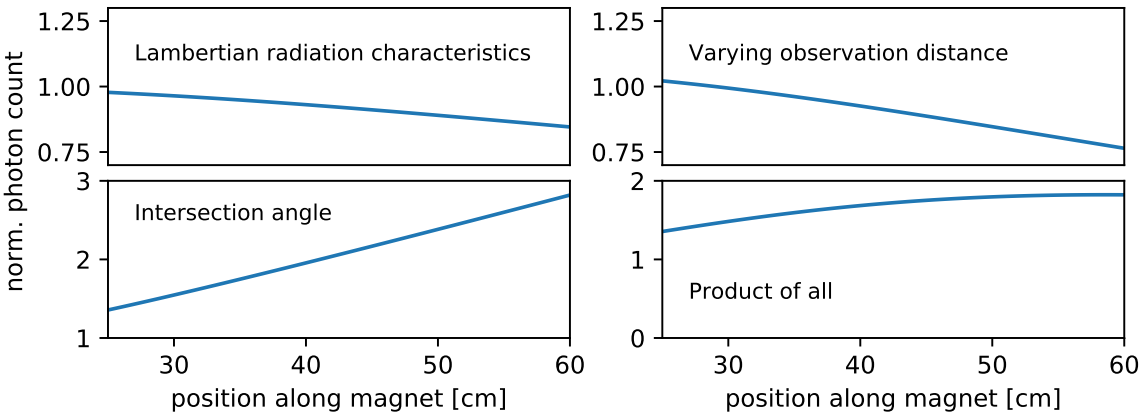

Figure B.5: ***Apparent change of scintillation light yield.*** *Corrections to the charge calibration due to different effects are given for the magnet geometry shown in Figure B.3 and B.4.*

This scaling suggests that we overestimate the charge by up to a factor of 1.85 at x=60 cm (400 MeV) without correction.

B.4 Implementation of the software for electron spectrum retrieval

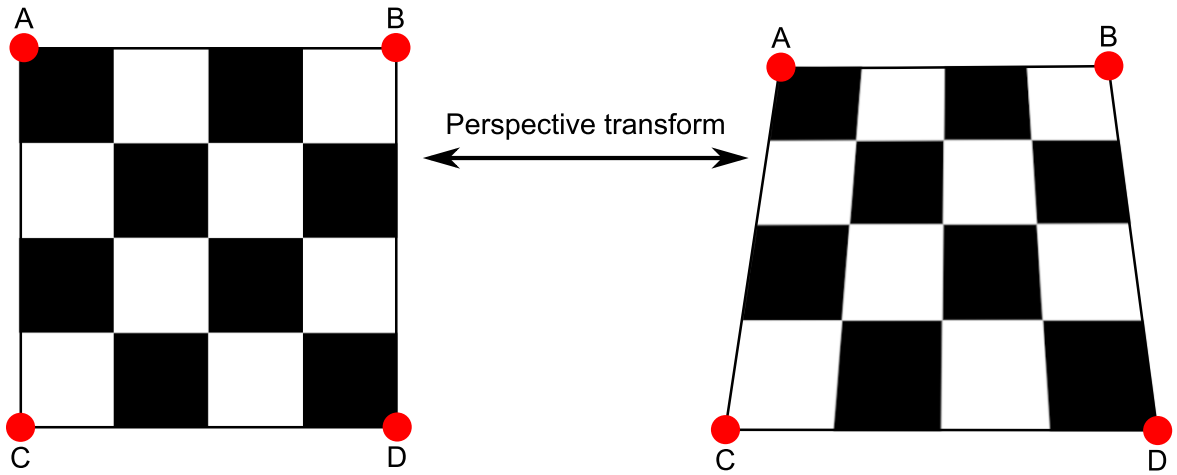

Figure B.6: ***Perspective transformation of a checkerboard.*** *Surface elements further away from the camera and imaged under shallower angles appear smaller.*

For the analysis of the dipole spectrometer data, raw images are processed in the following way:

1. Dark/background images are loaded.
2. Coordinates of the four edges of the rectangular Lanex screen are determined.
3. Perspective transformation matrix is calculated: edges of the screen are used to map the image of the screen onto a rectangular grid.
4. Sum over GTLS's region of interest yields value for calibration.
5. Data shots are loaded, background subtracted, and perspective transformation applied.
6. Data is divided by the calibration value of step 4.
7. Rectangular grid is mapped from distance to energy and divergence.

The complete code with more detailed comments is available online (see Chapter on data archiving).

The perspective transformation accounts for the varying distance to and Lambertian radiation characteristic of the Lanex screen. As seen in Figure B.6, surface elements further away from the camera and observed under shallower angles appear smaller. Under perspective transformation, their apparent size is increased. As the gray value is conserved under transformation, the transformation increases the integrated signal of these surface elements. The decrease of apparent area scales with the square of the distance to the observer. Furthermore, the surface elements appear foreshortened by the cosine of the observation angle relative to the surface normal. Therefore, the perspective transformation accounts for the issue of varying distance and observation angle, as discussed before. Please note that the images of the Lanex screen and GTLS need to be transformed in the same way before integrating over the respective areas of interest.

B.5 Estimating the uncertainty of the charge calibration

There is still a long list of factors influencing our charge calibration and adding up to the total uncertainty:

1. MLS calibration as explained above: +/- 20%
2. Lanex and Tritium imaging geometry: +/- 20%
3. Inconsistency in Thomas Kurz numbers for the different Lanex screens: +/- 10%
4. Tritium capsule afterglow: +/- 10%
5. incomplete bookkeeping of tritium capsule decay history: +/- 10%
6. potentially more stuff...

However, the good news is that whatever I have calculated so far, the number always ended up roughly in the same range. The potential errors added up favorably, compensating each other.

B.6 Hands on: How to get calibration value for a specific GTLS at a specific point in time

1. Take a few images of the MLS without diffuser (2 ms exposure time) and average.
2. Take a few background images under identical conditions and average.
3. Take a few images of GTLS at the same position as MLS (1s exposure time) and average.
4. Take a few background images under identical conditions and average.
5. Subtract respective backgrounds from data.
6. Devide both images by respective exposure time.
7. Choose the appropriate region of interest for both images.
8. Sum up all pixels in both ROIs.
9. Devide sum(MLS) by sum(GTLS).
10. Multiply this number by the correct value from the table below (depending on which Lanex you use).
11. For data analysis, sum the px count of the Lanex, divide it by the px count of the GTLS, and divide by the number you just derived. If the integration time is not 100 ms, multiply by the correct factor (e.g., factor 5 if the integration time was 500 ms).
12. Hint: In the experiment, it is wise to make a few shots without laser at a long exposure time (min. 500 ms) for the GTLS. Otherwise, the signal will be way too weak. For the experiment, reduce the exposure time to a few ms (this is still long enough to capture the full temporal extent of the scintillation signal) to enhance the signal-to-noise level and obtain much smaller image files (saves memory). Remember to take the shots for background subtraction using the same exposure time.

Table B.1: Calibration values of different Lanex materials. Valid for 100 ms integration time. Error margin: +/-30%.

Lanex	Munich MLS (no diffusor) $N_{Scint}/(N_{MLS} \cdot Q)$ [10^{-6}/pC]
Carestream Regular	2.03
Kodak Biomax MS	5.25
Konica Minolta OG400	2.45
CAWO OG 16B	3.91
CAWO OG 16F	2.42
Lanex Fine	0.62

Appendix C

Details on the target setup

TAKE-HOME MESSAGE

This appendix may tell the following generations how to set up and operate the hybrid target, including my home-built control circuit for the tape drive.

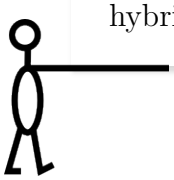

C.1 Description of the mechanical setup

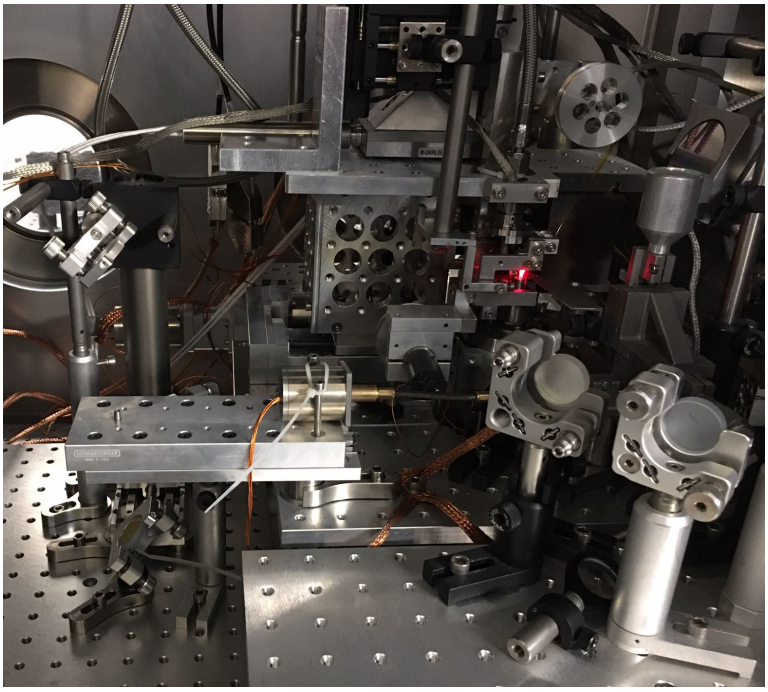

Figure C.1: ***Image of the new target holder in ETTF.*** *In addition to the elements labeled in Figure C.2, also two mirrors for the two probe beams (overview and few-cycle, see Section 2.3.3) are visible in the foreground.*

This appendix summarizes the layout and functionality of the target holder setup for the hybrid experiments, designed and built up by the author. An overview image of the setup in ETTF is shown in Figure C.1 and a schematic drawing in top and side view in Figure C.2. The setup consists of an elevated platform mounted on top of the existing hexapod stage for target alignment. While the first gas target (LWFA) is mounted directly to the hexapod, the second gas target (PWFA), setup for PWFA shock, and the tape drive holder are mounted to the elevated platform.

The new target holder fulfills the mechanical prerequisites for systematic scans of the key parameters: The distance between the two acceleration stages, the distance between the tape and both jets (see Section C.3), the positions of shocks for injection, and the density of both targets.

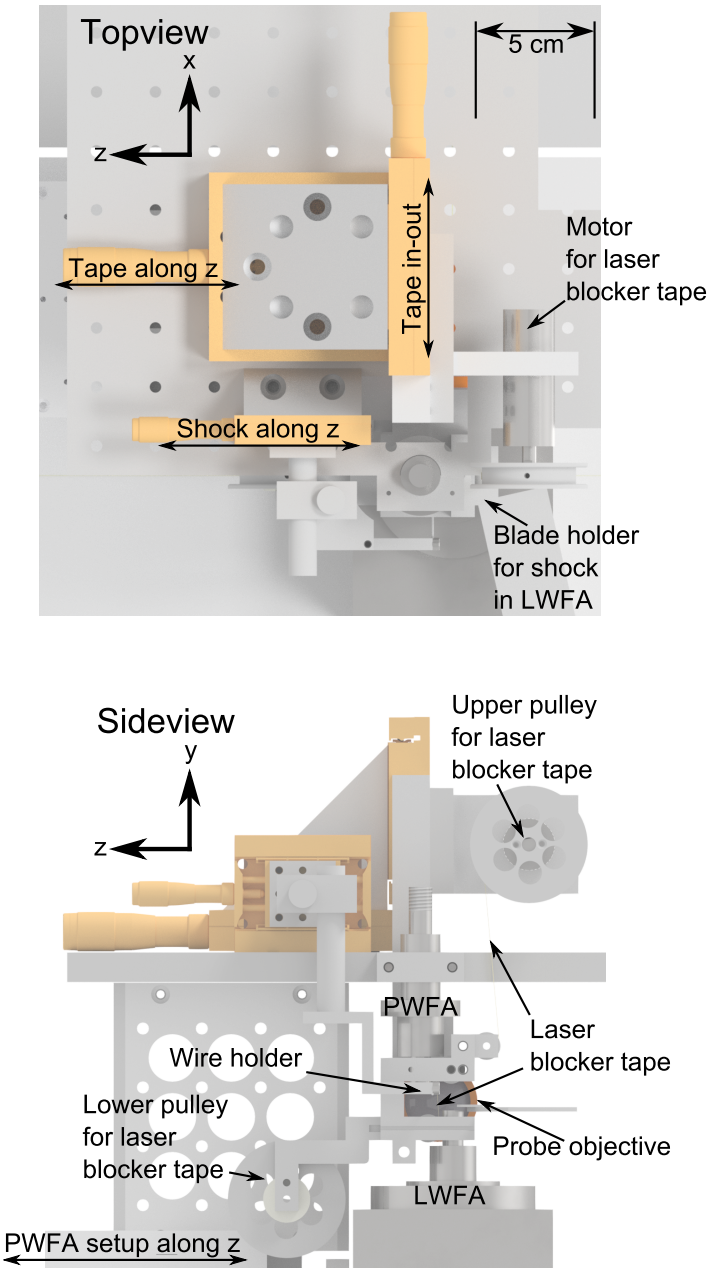

Figure C.2: ***CAD model of the setup for hybrid L-PWFA.*** *Top and side view of the new target holder in ETTF, showing the main elements and the mechanical degrees of freedom. The drive laser propagates along the positive z-axis. Micrometer screws on stages are replaced by motorized actuators in the actual setup. Note that this setup represents the implementation of the wire-generated shock in the PWFA. The setup for the optical injector is detailed in Figure C.7.*

The gas targets for the hybrid L-PWFA experiments were supersonic gas jets created from a variety of different nozzles (used ones listed below) connected to fast valves. The first jet can either be used with the electromagnetically actuated valve by Alameda Applied Sciences Corporation (AASC) or a solenoid valve by Parker (Series 9 Pulse Valve). The second gas jet needs to be operated with the more compact Parker valve due to space constraints. For the nozzles available in ETTF, the minimum distance between the nozzles is of the order of 5 mm, as there must be enough space between them for the laser blocker tape (see Section C.3).

C.2 Nozzles used in the experiment

The De Laval nozzle was invented by the Swedish engineer Gustaf de Laval for use in steam turbines. Due to their shape, they are also known as convergent-divergent nozzles and are used to accelerate a gas flow to supersonic speeds. The nozzle starts with a converging section. As the gas flows through this section, its velocity increases to preserve a constant mass flow. At the narrowest part of the nozzle, called the throat, the flow speed reaches the speed of sound ($Mach = 1$). After the throat, the nozzle widens in the diverging section, where the gas expands. During the expansion, the gas velocity further increases to supersonic speeds ($M > 1$) while the pressure and temperature drop. If the nozzle dimensions are chosen correctly, the supersonic flow is highly directed, and its density distribution is very homogeneous. While Laval nozzles are used in rockets to generate thrust, in plasma-based acceleration they are used to create gas targets with short up and down ramps and flat density profiles in between.

Laval nozzles are also useful when performing density down ramp or shock injection, as introducing an obstacle into the supersonic flow creates a density shock. In this work, this mechanism is used in the LWFA and in the wire-generated shock experiments in the PWFA (Section 3.2 and 3.3). The main characteristics of the nozzles used are summarized in Figure C.3. More details on the 5 mm LWFA nozzle, the 7 mm PWFA nozzle, and general considerations of nozzle design can be found in Hüthers Master thesis [133]. The generated density distributions are characterized via interferometry (Section 2.3.3) and are given in Figure 2.11.

Nozzle	d_o [mm]	d_t [mm]	h [mm]	opening angle
LWFA 5mm	5	0.61	18	7.4°
PWFA 4mm	4	1	22.5	3.8°
PWFA 7mm	7	0.86	18	9.6°

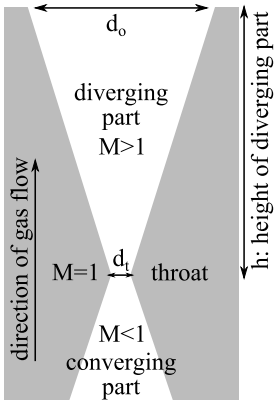

Figure C.3: ***Cross section of a Laval-type nozzle.*** *The table summarizes the dimensions of the different gas nozzles used in the experiments.*

C.3 Laser blocker tape

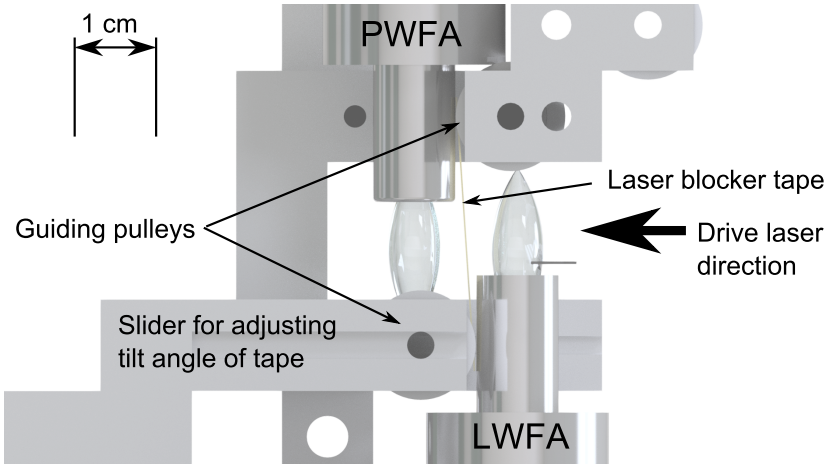

Figure C.4: ***Zoom-in on the CAD model of the laser blocker tape.*** *The* 25 μm*-thick Kapton tape is guided between both acceleration stages by an arrangement of pulleys.*

The position of the laser blocker tape can be scanned along the laser axis and moved transversely out of the beam path (see Figure C.2). The translational stages use geared stepper motors (Newport TRA25PPV6) and are integrated into the existing stepper motor control; therefore, their positions are archived per shot. Please note that this motor type is easily damaged when using too high drive currents. **Always limit the driver current per phase to 0.2 A!**

The tape drive consists of a few meters of tape on two spools connected to geared (196:1) DC-motors (Faulhaber 2232U024S R54 22GPT 196:1 KL3) and an arrangement of pulleys to guide the tape (see Figure C.4). The tape angle is chosen large enough to avoid a back reflex of the laser beam into the beam line. There are two versions of the setup: The initial implementation uses 7 mm-wide tape (used Kapton in the past), and the other uses 1/2" tape (used steel in the past). The second implementation of the laser blocker tape can also be used as the radiator for a transition radiation diagnostic (see Section 6.2.3).

C.4 Electrical installation of tape drive

After every laser shot, the laser blocker tape must be forwarded by a few millimeters. To this end, I implemented an analog motor control based on an H-bridge circuit to allow bidirectional drive control (see Fig. C.5). The motor control expects regular TTL trigger pulses as an input. The motor will move as long as the input is high. Therefore, the motor control can be connected to the trigger system in ETTF and will automatically forward the tape after every shot. The pulse length of the trigger should be on the order of 100 ms to advance the tape by a few mm. This number can be adjusted as needed. The motor control circuit proved to work precisely and reliably under experimental conditions. It is important to keep the tape under tension

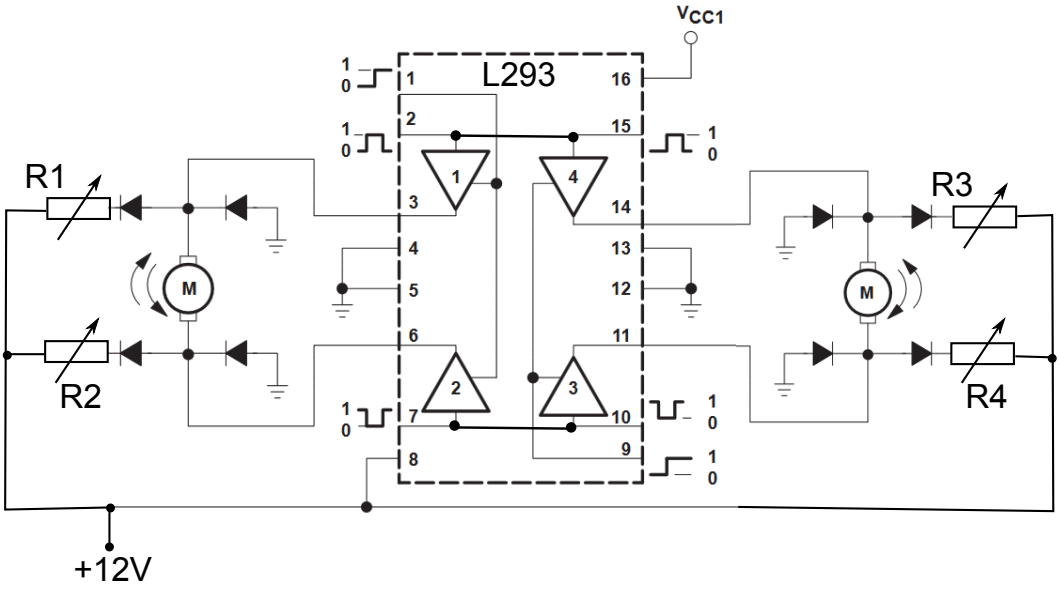

Figure C.5: ***Schematic of the DC motor control loop for the tape drive.***

at each time; therefore, the relative rotation speed of both tape spools needs to be set correctly. This adjustment is particularly important, as the tangential velocity will change with varying amounts of tape on the spools. To account for this, the motors are connected in series with potentiometers. With these resistors, the idle speed can be set slightly higher for the motor connected to the pulling spool. The tape then compensates for the movement of the spools; consequently remaining taut, and excess energy is dissipated via the ohmic resistance. The additional diodes in Figure C.5 are free-wheeling diodes and protect the circuit from induced voltage spikes. **Always plug in the motor control's power supply, trigger connection, and activate the respective trigger channel. If you miss one of these steps, equipment downstream of the tape will not be protected from laser damage.**

C.5 Performance of the laser blocker tape

While plasma mirrors proved their capabilities in a wide range of advanced applications, here the blocker tape is used to get rid of laser energy only. The energy on tape has been varied between 100mJ and 5J on target. A hole of approximately 1mm diameter is visible for Joule-level pulses after every shot. At 100 mJ the laser does not fully penetrate the tape in one go. An image of the used tape is shown in figure C.6.

A screen was placed 1.5 m downstream behind the target to monitor the transmitted beam. The plasma mirror acts as a spatial high-pass filter for the transmitted beam. While areas of homogeneous nearfield energy distribution are suppressed very efficiently, sharp edges become visible. The center part of the focus (low spatial frequencies and main part of energy) is reflected very well. In areas further off-axis (high spatial frequencies and little energy), the beam may not ignite a plasma efficiently and is consequently transmitted to a higher degree. The transmission for both cases, with

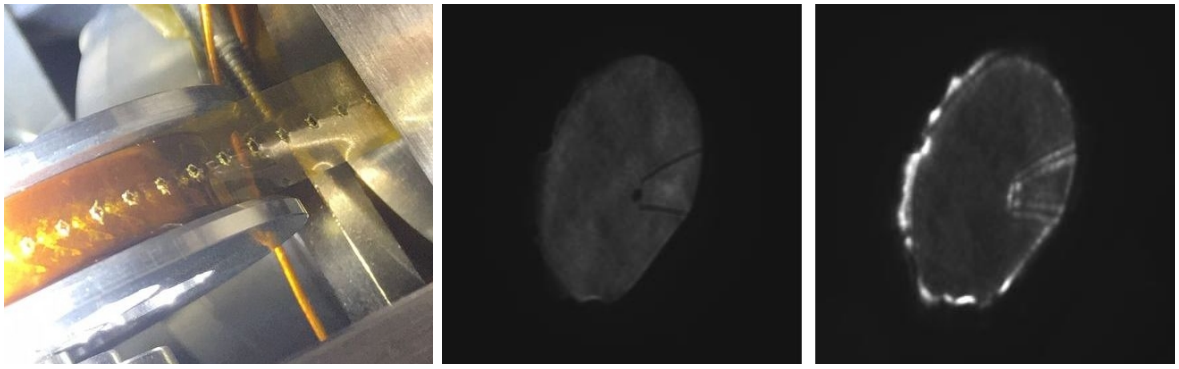

Figure C.6: ***The laser blocker tape.*** *Left: Blocker tape after interaction with the laser. A hole of approx. 1 mm diameter is caused by the interaction of the tape with a focused 100 TW class laser pulse. Middle and right: Beam profile on scattering screen 1.5 m downstream behind focus. Middle: Without tape. Right: Tape transmission and 13 x less filtering.*

and without tape, is depicted in figure C.6.

The transmission through the plasma mirror is estimated by comparing the beam's brightness on a scattering screen downstream of the tape. The transmission is on the order of a few percent. The exact value depends on the energy level and the tape's position relative to the focus. No ionization in the second jet is observed at the given transmission level.

C.6 Setup of the optical injector

The setup for the optical injector was introduced, and its main parameters were summarized in Section 1.4.1. In Figure C.7, an additional CAD model of the implementation is given for future reference. The steering mirrors for the optical injector are arranged to produce an astigmatic focus and to leave a clear line of sight for optical probing of the wakefield accelerator.

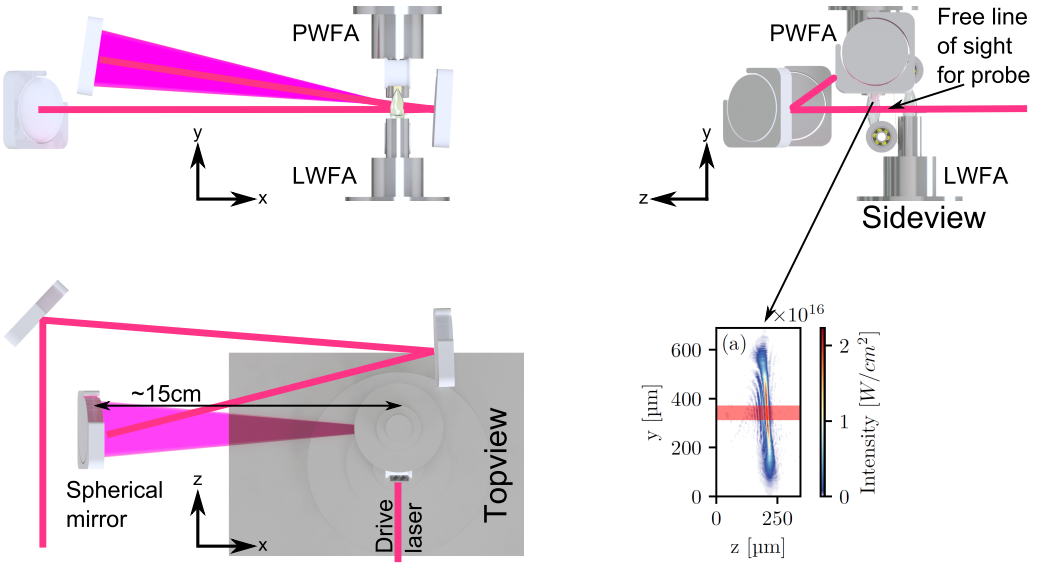

Figure C.7: ***CAD model of the setup of the optical injector.*** *Views of the optical injector setup from three different sides together with an image of the injector beam in the plane containing the wakefield axis. The injector beam has a strongly astigmatic focus due to the large angle of incidence on the spherical mirror.*

Data availability

The experimental raw data, the scripts for generating the simulations, and the associated evaluation and visualization routines are stored on the Data Archive Server of the Laboratory for Attosecond Physics at the Max Planck Institute of Quantum Optics.

The experimental raw data was typically saved as .png or .txt files. The input files to build the respective simulations are Python code (.py or .ipynb) and the simulation results were saved as .h5 files. All experimental and simulation raw data was processed using Python in Jupyter notebooks. Analyzed electron spectra were saved as .npy and can also be found in the archive alongside the raw data.

In addition to the data and scripts, the archive contains numerous readme.txt files that comment on the contents of the respective folder.

The following table summarizes figures that have been made from raw experimental and simulation data, together with the date and run of the data acquisition and a reference to the analysis script used (path relative to the archiving path given above).

Figures not listed in this table are vector graphics generated by the author. Relevant takeovers from other references are indicated in the respective captions.

Figure	Date and run	Analysis/plotting script
I.2	-	/documentation/plotting/1D_wakefield.ipynb
I.3	-	/documentation/plotting/div_survey/Div_survey.ipynb
1.1	-	/documentation/plotting/Easy_plotting.ipynb
1.2	-	/documentation/plotting/Easy_plotting.ipynb
1.3	-	/documentation/plotting/1D_wakefield.ipynb
1.4	-	/documentation/plotting/Theory_laser_and_beam_driven.ipynb
1.5	-	/documentation/plotting/beamloading_theory.ipynb
2.4	20210325	/documentation/plotting/Compression/Compression.ipynb
2.5	20201102	/documentation/plotting/Tundra/Tundra.ipynb
2.6	-	/documentation/plotting/attenuator/attenuator.ipynb
2.7	20210305	/documentation/plotting/Focus/focus.ipynb
2.9	-	/documentation/plotting/dipole_spectrometer.ipynb
2.11	-	/documentation/plotting/gas_density_final.ipynb

Figure	Date and run	Analysis/plotting script
3.1	20201212, 79-87,100-105	/documentation/plotting/Plotting_Spectra.ipynb
3.2	20201212, 74-78,88-94	/documentation/plotting/Plotting_Spectra.ipynb
3.3	20201212, 74-78,88-94	/documentation/plotting/Plotting_Spectra.ipynb
3.4	20201212, 63 + 84	/documentation/plotting/Plotting_Spectra.ipynb
3.5	20210222, 53	/documentation/plotting/Optical_injector.ipynb
3.6	20210222, 53	/documentation/plotting/Optical_injector.ipynb
3.7	20210222, 53	/documentation/plotting/Optical_injector.ipynb
3.8	20210222, 53	/documentation/plotting/Optical_injector.ipynb
3.9	20210222, 53	/documentation/plotting/Optical_injector.ipynb
	20210305, 41 + 42	
3.10	20201214, 76 + 79	/documentation/plotting/Optical_injector.ipynb
4.1	20210305, 29,44,63	/documentation/plotting/Plotting_Spectra.ipynb
4.2	20210305, 44	/documentation/plotting/Plotting_Spectra.ipynb
4.3	-	/documentation/plotting/PIC_plots_spectra.ipynb
4.4	-	/documentation/plotting/PIC_plots_spectra.ipynb
4.5	-	/documentation/plotting/PIC_plots_spectra.ipynb
4.6	-	/documentation/plotting/PIC_plots_spectra.ipynb
4.7	-	/documentation/plotting/PIC_plots_spectra.ipynb
4.8	-	/documentation/plotting/PIC_plots_spectra.ipynb
4.9	-	/documentation/plotting/Easy_plotting.ipynb
4.10	-	/documentation/plotting/PIC_plots_emittance.ipynb
4.11	-	/documentation/plotting/Phase_space_tutorial.ipynb
5.1	20210330	/documentation/plotting/Plasma_Waves.ipynb
5.2	20210325, 37,43,45,46,48	/documentation/plotting/Plotting_Spectra.ipynb
5.3	20201212, 66,75,87,89	/documentation/plotting/Plotting_Spectra.ipynb
5.4	20210325, 46 + 48	/documentation/plotting/Plotting_Spectra.ipynb
5.5	20210325, 37 + 48	/documentation/plotting/Plotting_Spectra.ipynb
5.6	20210325, 37 + 48	/documentation/plotting/Plotting_Spectra.ipynb
	20210324, 38 + 39	
5.7	-	/documentation/plotting/PIC_plots_emittance.ipynb
6.1	-	/documentation/plotting/div_survey/Div_survey.ipynb
6.2	20221017, 30 + 38	/documentation/plotting/HighE_shots.ipynb
6.3	-	/documentation/plotting/Simulations_outlook.ipynb
6.4	-	/documentation/plotting/Simulations_outlook.ipynb
6.5	-	/documentation/plotting/Plasmalens.ipynb

Previous publication of data and author contributions

The experimental data shown in this work were collected under the leadership of the author of this work and with the help of Prof. Karsch's entire working group.

The data analysis and interpretation presented in this thesis are original works by the author, some of which have already been published in: Foerster et al. PRX (2022) [68]. Footnotes in the individual sections provide information on the extent to which the individual results reproduce the previously published data.

The PIC simulations in the chapters on witness beam stability and quality were initialized, and input parameters were verified by Dr. Andreas Döpp for the joint publication [68]. The PIC simulations in the summary chapter were initialized, and input parameters were verified by Dr. Johannes Zirkelbach. The analysis of the simulations is original work by the author of this thesis.

Scientific Publications by the author

As first author

- **F. M. Foerster**, A. Döpp, F. Haberstroh, K. v. Grafenstein, D. Campbell, Y.-Y. Chang, S. Corde, J. P. Couperus Cabadağ, A. Debus, M. F. Gilljohann, A. F. Habib, T. Heinemann, B. Hidding, A. Irman, F. Irshad, A. Knetsch, O. Kononenko, A. Martinez de la Ossa, A. Nutter, R. Pausch, G. Schilling, A. Schletter, S. Schöbel, U. Schramm, E. Travac, P. Ufer, and S. Karsch. Stable and High-Quality Electron Beams from Staged Laser and Plasma Wakefield Accelerators. Phys. Rev. X 12, 041016 (2022).

As co-author

- Götzfried, J., Döpp, A., Gilljohann, M. F., **Foerster, F. M.**, Ding, H., Schindler,S., Schilling, G., Buck, A., Veisz, L. and Karsch, S.. Physics of High-Charge Electron Beams in Laser-Plasma Wakefields. Phys. Rev. X 10, 041015 (2020).

- Raj, G., Kononenko, O., Gilljohann, M. F., Doche, A., Davoine, X., Caizergues,C., Chang, Y.-Y., Couperus Cabadağ, J. P., Debus, A., Ding, H., **Foerster, M.**, Goddet, J.-P., Heinemann, T., Kluge, T., Kurz, T., Pausch, R., Rousseau, P., San Miguel Claveria, P., Schöbel, S., et al. Probing ultrafast magnetic-field generation by current filamentation instability in femtosecond relativistic laser-matter interactions. Phys. Rev. Res. 2, 1–7 (2020).

- Couperus Cabadağ, J. P., Pausch, R., Schöbel, S., Bussmann, M., Chang, Y.-Y., Corde, S., Debus, A., Ding, H., Döpp, A., **Foerster, F. M.**, Gilljohann, M., Haberstroh, F., Heinemann, T., Hidding, B., Karsch, S., Koehler, A., Kononenko, O., Knetsch, A., Kurz, T., et al. Gas-dynamic density downramp injection in a beam-driven plasma wakefield accelerator. Phys. Rev. Res. 3, L042005 (2021).

- S. Schöbel, R. Pausch, Y.-Y. Chang, S. Corde, J. Couperus Cabadağ, A. Debus, H. Ding, A. Döpp, **F. M. Foerster**, M. Gilljohann, F. Haberstroh, T. Heinemann, B. Hidding, S. Karsch, A. Köhler, O. Kononenko, T. Kurz, A. Nutter, K. Steiniger, P. Ufer, A. Martinez de la Ossa, U. Schramm and A. Irman. Effect of driver charge on wakefield characteristics in a plasma accelerator probed by femtosecond shadowgraphy. New J. Phys. 24, 083034 (2022).

- B. Hidding, R. Assmann, M. Bussmann, D. Campbell, Y-Y. Chang, S. Corde, J. Couperus Cabadağ, A. Debus, A. Döpp, M. Gilljohann, J. Götzfried, **F. M. Foerster**, F. Haberstroh, F. Habib, T. Heinemann, D. Hollatz, A. Irman, M. Kaluza, S. Karsch, O. Kononenko, A. Knetsch, T. Kurz, S. Kuschel, A. Köhler, A. Martinez de la Ossa, A. Nutter, R. Pausch, G. Raj, U. Schramm, S. Schöbel, A. Seidel, K. Steiniger, P. Ufer, M. Yeung, O. Zarini and M. Zepf. Progress in Hybrid Plasma Wakefield Acceleration. Photonics 10(2), 99 (2023).

- N. Weisse, J. Esslinger, S. Howard, **F. M. Foerster**, F. Haberstroh, L. Doyle, P. Norreys, J. Schreiber, S. Karsch, and A. Döpp, Measuring spatio-temporal couplings using modal spatio-spectral wavefront retrieval. Opt. Express 31, 19733-19745 (2023).

- K. v. Grafenstein, **F.M. Foerster**, F. Haberstroh, D. Campbell. F. Irshad, F.C. Salgado, G. Schilling, E. Travac, N. Weiße, M. Zepf, A. Döpp and S. Karsch. Laser-accelerated electron beams at 1 GeV using optically-induced shock injection. Sci Rep 13, 11680 (2023).

- F. Irshad, C. Eberle, **F. M. Foerster**, K. v. Grafenstein, F. Haberstroh, E. Travac, N. Weisse, S. Karsch, A. Döpp, Pareto Optimization and Tuning of a Laser Wakefield Accelerator. Phys. Rev. Lett. 133, 085001 (2024).

Bibliography

1. Emberley, E. *Ed Emberley's Drawing Book: Make a World* 1st rev. pbk. ed. ISBN: 978-0316789721 (Little, Brown and Co, New York, 2006) (cit. on p. 1).
2. Thomas, A. *in: Proceedings of the 2019 CERN–Accelerator–School course on High Gradient Wakefield Accelerators, Sesimbra, (Portugal), CERN 2020* https://cas.web.cern.ch/previous-schools (cit. on p. 1).
3. *Accelerators and Nobel Laureates* https://www.nobelprize.org/prizes/themes/accelerators-and-nobel-laureates/. Accessed: 2023-08-14 (cit. on p. 2).
4. Bird, D. J. *et al.* Detection of a Cosmic Ray with Measured Energy Well beyond the Expected Spectral Cutoff Due to Cosmic Microwave Radiation. *The Astrophysical Journal* **441,** 144 (1995) (cit. on p. 2).
5. Lawrence, E. O. & Edlefsen, N. E. On the production of high speed protons. *Science* **72,** 376 (1930) (cit. on p. 2).
6. Kerst, D. W. Acceleration of Electrons by Magnetic Induction. *Physical Review* **58,** 841–841 (1940) (cit. on pp. 2, 24).
7. Wideroee, R. Ueber ein neues Prinzip zur Herstellung hoher Spannungen. *Archiv fuer Elektrotechnik* **21,** 387–406. ISSN: 1432-0487 (1928) (cit. on pp. 2, 24).
8. McMillan, E. M. The Synchrotron—A Proposed High Energy Particle Accelerator. *Physical Review* **68,** 143–144 (1945) (cit. on p. 2).
9. Banks, M. Panel calls on physicists to 'shelve' notion of Japan hosting the International Linear Collider. *physicsworld.* Accessed: 2023-08-05 (2022) (cit. on p. 2).
10. Tajima, T. & Dawson, J. M. Laser Electron Accelerator. *Physical Review Letters* **43,** 267–270. ISSN: 0031-9007 (1979) (cit. on p. 4).
11. Strickland, D. & Mourou, G. Compression of Amplified Chirped Optical Pulses. *Optics Communications* **55,** 447–449. ISSN: 00304018 (1985) (cit. on pp. 4, 29).
12. Modena, A. *et al.* Electron Acceleration from the Breaking of Relativistic Plasma Waves. *Nature* **377,** 606–608. ISSN: 0028-0836, 1476-4687 (1995) (cit. on p. 4).
13. Pukhov, A., Gordienko, S., Kiselev, S. & Kostyukov, I. The Bubble Regime of Laser–Plasma Acceleration: Monoenergetic Electrons and the Scalability. *Plasma Physics and Controlled Fusion* **46,** B179–B186. ISSN: 0741-3335, 1361-6587 (2004) (cit. on pp. 4, 16).
14. Malka, V. *et al.* Electron Acceleration by a Wake Field Forced by an Intense Ultrashort Laser Pulse. *Science* **298,** 1596–1600. ISSN: 0036-8075, 1095-9203 (2002) (cit. on p. 4).
15. Faure, J. *et al.* A Laser–Plasma Accelerator Producing Monoenergetic Electron Beams. *Nature* **431,** 541–544. ISSN: 1476-4687 (2004) (cit. on p. 4).

16. Mangles, S. P. D. *et al.* Monoenergetic Beams of Relativistic Electrons from Intense Laser–Plasma Interactions. *Nature* **431,** 535–538. ISSN: 1476-4687 (2004) (cit. on p. 4).

17. Geddes, C. G. R. *et al.* High-Quality Electron Beams from a Laser Wakefield Accelerator Using Plasma-Channel Guiding. *Nature* **431,** 538–541. ISSN: 1476-4687 (2004) (cit. on p. 4).

18. Schmid, K. *et al.* Density-Transition Based Electron Injector for Laser Driven Wakefield Accelerators. *Physical Review Special Topics - Accelerators and Beams* **13,** 091301 (2010) (cit. on pp. 4, 25).

19. Buck, A. *et al.* Shock-Front Injector for High-Quality Laser-Plasma Acceleration. *Physical Review Letters* **110,** 185006. ISSN: 0031-9007, 1079-7114 (2013) (cit. on pp. 4, 25).

20. Faure, J., Rechatin, C., Lundh, O., Ammoura, L. & Malka, V. Injection and acceleration of quasimonoenergetic relativistic electron beams using density gradients at the edges of a plasma channel. *Physics of Plasmas* **17,** 083107 (2010) (cit. on pp. 4, 26).

21. Brijesh, P. *et al.* Tuning the electron energy by controlling the density perturbation position in laser plasma accelerators. *Physics of Plasmas* **19,** 063104–063104–6 (2012) (cit. on pp. 4, 26).

22. Fubiani, G., Esarey, E., Schroeder, C. B. & Leemans, W. P. Beat Wave Injection of Electrons into Plasma Waves Using Two Interfering Laser Pulses. *Physical Review E* **70,** 016402. ISSN: 1539-3755, 1550-2376 (2004) (cit. on p. 4).

23. Faure, J. *et al.* Controlled Injection and Acceleration of Electrons in Plasma Wakefields by Colliding Laser Pulses. *Nature* **444,** 737–739. ISSN: 0028-0836, 1476-4687 (2006) (cit. on p. 4).

24. Wenz, J. *et al.* Dual-energy electron beams from a compact laser-driven accelerator. *Nature Photonics* **13,** 263–269 (2019) (cit. on p. 4).

25. Heigoldt, M. *et al.* Temporal evolution of longitudinal bunch profile in a laser wakefield accelerator. *Physical Review Special Topics-Accelerators and Beams* **18,** 121302 (2015) (cit. on pp. 4, 6, 44, 84, 90, 98).

26. Zarini, O. *et al.* Multioctave High-Dynamic Range Optical Spectrometer for Single-Pulse, Longitudinal Characterization of Ultrashort Electron Bunches. *Physical Review Accelerators and Beams* **25,** 012801 (2022) (cit. on pp. 4, 90).

27. Kneip, S. *et al.* Characterization of Transverse Beam Emittance of Electrons from a Laser-Plasma Wakefield Accelerator in the Bubble Regime Using Betatron x-Ray Radiation. *Physical Review Special Topics - Accelerators and Beams* **15,** 021302. ISSN: 1098-4402 (2012) (cit. on pp. 4, 90).

28. Wenz, J. *et al.* Quantitative X-ray phase-contrast microtomography from a compact laser-driven betatron source. *Nature Communications* **6,** 7568 (2015) (cit. on pp. 4, 90).

29. Götzfried, J. *et al.* Physics of High-Charge Electron Beams in Laser-Plasma Wakefields. *Physical Review X* **10,** 041015 (2020) (cit. on pp. 4, 6, 23, 42–44, 47, 63, 70, 78, 93).

30. Gonsalves, A. J. *et al.* Petawatt Laser Guiding and Electron Beam Acceleration to 8 GeV in a Laser-Heated Capillary Discharge Waveguide. *Physical Review Letters* **122,** 084801 (2019) (cit. on p. 4).

31. Chen, P., Dawson, J. M., Huff, R. W. & Katsouleas, T. Acceleration of Electrons by the Interaction of a Bunched Electron Beam with a Plasma. *Physical Review Letters* **54,** 693–696. ISSN: 0031-9007 (1985) (cit. on p. 4).

32. Rosenzweig, J. B. *et al.* Experimental Observation of Plasma Wake-Field Acceleration. *Physical Review Letters* **61,** 98–101. ISSN: 0031-9007 (1988) (cit. on p. 4).

33. Blumenfeld, I. *et al.* Energy doubling of 42 GeV electrons in a metre-scale plasma wakefield accelerator. *Nature* **445,** 741–744 (2007) (cit. on pp. 4, 19).

34. Litos, M. *et al.* High-efficiency acceleration of an electron beam in a plasma wakefield accelerator. *Nature* **515,** 92–95 (2014) (cit. on pp. 4, 53, 54).

35. Corde, S. *et al.* Multi-Gigaelectronvolt Acceleration of Positrons in a Self-Loaded Plasma Wakefield. *Nature* **524,** 442–445. ISSN: 1476-4687 (2015) (cit. on p. 4).

36. D'Arcy, R. *et al.* FLASHForward: Plasma Wakefield Accelerator Science for High-Average-Power Applications. *Philosophical Transactions of the Royal Society A: Mathematical, Physical and Engineering Sciences* **377,** 20180392 (2019) (cit. on pp. 4, 91).

37. Adli, E. *et al.* Acceleration of electrons in the plasma wakefield of a proton bunch. *Nature* **561,** 363–367 (7723 2018) (cit. on p. 4).

38. Maier, A. R. *et al.* Decoding Sources of Energy Variability in a Laser-Plasma Accelerator. *Physical Review X* **10,** 031039 (2020) (cit. on pp. 5, 20).

39. Corde, S. *et al.* Mapping the X-Ray Emission Region in a Laser-Plasma Accelerator. *Physical Review Letters* **107,** 215004. ISSN: 0031-9007, 1079-7114 (2011) (cit. on p. 6).

40. Chou, S. *et al.* Collective Deceleration of Laser-Driven Electron Bunches. *Physical Review Letters* **117,** 144801 (2016) (cit. on pp. 6, 47, 49, 93).

41. Couperus, J. P. *et al.* Demonstration of a beam loaded nanocoulomb-class laser wakefield accelerator. *Nature Communications* **8,** 1–7 (1 2017) (cit. on p. 6).

42. Gilljohann, M. F. *et al.* Direct Observation of Plasma Waves and Dynamics Induced by Laser-Accelerated Electron Beams. *Phys. Rev. X* **9,** 011046 (1 2019) (cit. on pp. 7, 17, 47, 78, 82, 93).

43. Kurz, T. *et al.* Demonstration of a compact plasma accelerator powered by laser-accelerated electron beams. *Nature Communications* **12,** 2895 (2021) (cit. on pp. 7, 17, 47, 49, 54, 82, 93).

44. Couperus Cabada ğ, J. P. *et al.* Gas-dynamic density downramp injection in a beam-driven plasma wakefield accelerator. *Phys. Rev. Research* **3,** L042005 (4 2021) (cit. on pp. 7, 47, 50, 61).

45. Hidding, B. *et al.* Ultracold Electron Bunch Generation via Plasma Photocathode Emission and Acceleration in a Beam-Driven Plasma Blowout. *Physical Review Letters* **108,** 035001 (2012) (cit. on pp. 7, 77, 92, 98).

46. Martinez de la Ossa, A., Grebenyuk, J., Mehrling, T., Schaper, L. & Osterhoff, J. High-Quality Electron Beams from Beam-Driven Plasma Accelerators by Wakefield-Induced Ionization Injection. *Phys. Rev. Lett.* **111,** 245003 (24 2013) (cit. on p. 7).

47. Martinez de la Ossa, A., Mehrling, T. J., Schaper, L., Streeter, M. J. V. & Osterhoff, J. Wakefield-induced ionization injection in beam-driven plasma accelerators. *Physics of Plasmas* **22,** 093107 (2015) (cit. on pp. 7, 50, 92).

48. Hidding, B. *et al.* Monoenergetic Energy Doubling in a Hybrid Laser-Plasma Wakefield Accelerator. *Physical Review Letters* **104,** 195002 (2010) (cit. on pp. 7, 95).

49. Hidding, B. *et al.* Progress in Hybrid Plasma Wakefield Acceleration. *Photonics* **10,** 99. ISSN: 2304-6732 (2023) (cit. on p. 7).

50. Gibbon, P. *Short Pulse Laser Interactions with Matter: An Introduction* ISBN: 978-1860941351 (PUBLISHED BY IMPERIAL COLLEGE PRESS AND DISTRIBUTED BY WORLD SCIENTIFIC PUBLISHING CO., 2005) (cit. on pp. 9, 14).

51. Born, M. *et al. Principles of Optics: Electromagnetic Theory of Propagation, Interference and Diffraction of Light* 7th ed. ISBN: 9781139644181 (Cambridge University Press, 1999) (cit. on p. 10).

52. Jackson, J. D. *Classical Electrodynamics* 3rd ed. ISBN: 978-0-471-30932-1 (Wiley, New York, 1999) (cit. on pp. 10, 11).

53. Kruer, W. L. *The Physics of Laser Plasma Interactions* ISBN: 978-0-8133-4083-8 (Boulder, Colo. [u.a.] Westview, 2003) (cit. on p. 11).

54. Sarachik, E. S. & Schappert, G. T. Classical Theory of the Scattering of Intense Laser Radiation by Free Electrons. *Physical Review D* **1,** 2738–2753. ISSN: 0556-2821 (1970) (cit. on p. 12).

55. Sprangle, P., Esarey, E. & Ting, A. Nonlinear Theory of Intense Laser-Plasma Interactions. *Physical Review Letters* **64,** 2011–2014. ISSN: 0031-9007 (1990) (cit. on p. 14).

56. Esarey, E., Sprangle, P., Krall, J. & Ting, A. Overview of Plasma-Based Accelerator Concepts. *IEEE Transactions on Plasma Science* **24,** 252–288. ISSN: 00933813 (1996) (cit. on p. 14).

57. Rosenzweig, J. B. Nonlinear Plasma Dynamics in the Plasma Wake-Field Accelerator. *Physical Review Letters* **58,** 555–558. ISSN: 0031-9007 (1987) (cit. on p. 14).

58. Esarey, E., Schroeder, C. B. & Leemans, W. P. Physics of Laser-Driven Plasma-Based Electron Accelerators. *Reviews of Modern Physics* **81,** 1229–1285. ISSN: 0034-6861, 1539-0756 (2009) (cit. on p. 14).

59. Dawson, J. M. Nonlinear Electron Oscillations in a Cold Plasma. *Physical Review* **113,** 383–387. ISSN: 0031-899X (1959) (cit. on p. 15).

60. Mori, W. B. & Katsouleas, T. Wavebreaking of Longitudinal Plasma Oscillations. *Physica Scripta* **T30,** 127–133. ISSN: 0031-8949, 1402-4896 (1990) (cit. on p. 15).

61. Lu, W. *et al.* A Nonlinear Theory for Multidimensional Relativistic Plasma Wave Wakefields. *Physics of Plasmas* **13,** 056709. ISSN: 1070-664X, 1089-7674 (2006) (cit. on p. 16).

62. Lu, W. *et al.* Generating Multi-GeV Electron Bunches Using Single Stage Laser Wakefield Acceleration in a 3D Nonlinear Regime. *Physical Review Special Topics - Accelerators and Beams* **10,** 061301 (2007) (cit. on pp. 16, 19).

63. Pukhov, A. & Meyer-ter-Vehn, J. Laser Wake Field Acceleration: The Highly Non-Linear Broken-Wave Regime. *Applied Physics B* **74,** 355–361. ISSN: 1432-0649 (2002) (cit. on p. 16).

64. Gordienko, S. & Pukhov, A. Scalings for Ultrarelativistic Laser Plasmas and Quasimonoenergetic Electrons. *Physics of Plasmas* **12,** 043109. ISSN: 1070-664X, 1089-7674 (2005) (cit. on p. 16).

65. Schöbel, S. *et al.* Effect of Driver Charge on Wakefield Characteristics in a Plasma Accelerator Probed by Femtosecond Shadowgraphy. *New Journal of Physics* **24,** 083034. ISSN: 1367-2630 (2022) (cit. on pp. 17, 49, 50, 82).

66. Rosenzweig, J. B., Breizman, B., Katsouleas, T. & Su, J. J. Acceleration and Focusing of Electrons in Two-Dimensional Nonlinear Plasma Wake Fields. *Physical Review A* **44,** R6189–R6192. ISSN: 1050-2947, 1094-1622 (1991) (cit. on pp. 19, 75).

67. Berger, C. *et al.* Active Nonperturbative Stabilization of the Laser-Plasma-Accelerated Electron Beam Source. *Physical Review Accelerators and Beams* **26,** 032801 (2023) (cit. on p. 20).

68. Foerster, F. M. *et al.* Stable and High-Quality Electron Beams from Staged Laser and Plasma Wakefield Accelerators. *Physical Review X* **12,** 041016 (2022) (cit. on pp. 20, 54, 65, 67, 73, 84, 87, 126).

69. Martinez de la Ossa, A. *et al.* Optimizing density down-ramp injection for beam-driven plasma wakefield accelerators. *Phys. Rev. Accel. Beams* **20,** 091301 (9 2017) (cit. on pp. 22, 25, 62, 89).

70. Lotov, K. V. Efficient operating mode of the plasma wakefield accelerator. *Physics of Plasmas* **12,** 053105 (2005) (cit. on p. 22).

71. Tzoufras, M. *et al.* Beam Loading in the Nonlinear Regime of Plasma-Based Acceleration. *Physical Review Letters* **101,** 145002. ISSN: 0031-9007, 1079-7114 (2008) (cit. on p. 23).

72. Tzoufras, M. *et al.* Beam Loading by Electrons in Nonlinear Plasma Wakes. *Physics of Plasmas* **16,** 056705. ISSN: 1070-664X, 1089-7674 (2009) (cit. on p. 23).

73. Kirchen, M. *et al.* Optimal Beam Loading in a Laser-Plasma Accelerator. *Physical Review Letters* **126,** 174801 (2021) (cit. on p. 23).

74. Lindstrøm, C. A. *et al.* Energy-Spread Preservation and High Efficiency in a Plasma-Wakefield Accelerator. *Phys. Rev. Lett.* **126,** 014801 (1 2021) (cit. on pp. 23, 53, 54, 91).

75. Swanson, K. K. *et al.* Control of tunable, monoenergetic laser-plasma-accelerated electron beams using a shock-induced density downramp injector. *Physical Review Accelerators and Beams* **20,** 051301 (2017) (cit. on p. 25).

76. Shalloo, R. J. *et al.* Hydrodynamic optical-field-ionized plasma channels. *Physical Review E* **97,** 053203 (5 2018) (cit. on pp. 25, 26).

77. Durfee, C. G. & Milchberg, H. M. Light Pipe for High Intensity Laser Pulses. *Physical Review Letters* **71,** 2409–2412. ISSN: 0031-9007 (1993) (cit. on p. 26).

78. Picksley, A. *et al.* Guiding of High-Intensity Laser Pulses in 100-Mm-Long Hydrodynamic Optical-Field-Ionized Plasma Channels. *Physical Review Accelerators and Beams* **23,** 081303. ISSN: 2469-9888 (2020) (cit. on p. 26).

79. Picksley, A. *et al.* Meter-Scale Conditioned Hydrodynamic Optical-Field-Ionized Plasma Channels. *Physical Review E* **102,** 053201 (2020) (cit. on p. 26).

80. Goffin, A. *et al.* Optical Guiding in 50-Meter-Scale Air Waveguides. *Physical Review X* **13,** 011006 (2023) (cit. on p. 26).

81. Miao, B., Feder, L., Shrock, J. E., Goffin, A. & Milchberg, H. M. Optical Guiding in Meter-Scale Plasma Waveguides. *Physical Review Letters* **125,** 074801 (2020) (cit. on p. 26).

82. Fourmaux, S. *et al.* Quasi-monoenergetic electron beams production in a sharp density transition. *Applied Physics Letters* **101,** 111106 (2012) (cit. on p. 26).

83. *FBPIC documentation* `https://fbpic.github.io`. Accessed: 2023-07-30 (cit. on p. 27).

84. Lehe, R., Kirchen, M., Andriyash, I. A., Godfrey, B. B. & Vay, J.-L. A spectral, quasi-cylindrical and dispersion-free Particle-In-Cell algorithm. *Computer Physics Communications* **203,** 66–82 (2016) (cit. on p. 27).

85. Gilljohann, M. *Towards hybrid wakefield acceleration* PhD thesis (Ludwig-Maximilians-Universität München, 2022) (cit. on pp. 28–31).

86. Doyle, L. *Implementation of an Adaptive Optics System for Focus Optimization at the Centre for Advanced Laser Applications* MA thesis (Ludwig-Maximilians-Universität München, 2019) (cit. on pp. 32, 35).

87. Popp, A. *et al.* All-Optical Steering of Laser-Wakefield-Accelerated Electron Beams. *Physical Review Letters* **105,** 215001. ISSN: 0031-9007, 1079-7114 (2010) (cit. on pp. 34, 82).

88. Weisse, N. *et al.* Measuring Spatio-Temporal Couplings Using Modal Spatio-Spectral Wavefront Retrieval. *Optics Express* **31,** 19733. ISSN: 1094-4087 (2023) (cit. on p. 34).

89. Thaury, C. *et al.* Shock assisted ionization injection in laser-plasma accelerators. *Scientific Reports* **5,** 16310 EP –- (2015) (cit. on p. 36).

90. Wittig, G. *et al.* Optical Plasma Torch Electron Bunch Generation in Plasma Wakefield Accelerators. *Physical Review Special Topics - Accelerators and Beams* **18,** 081304 (2015) (cit. on p. 37).

91. Knetsch, A. *et al.* Stable witness-beam formation in a beam-driven plasma cathode. *Phys. Rev. Accel. Beams* **24,** 101302 (10 2021) (cit. on pp. 37, 54, 77, 94).

92. Ullmann, D. *et al.* All-optical density downramp injection in electron-driven plasma wakefield accelerators. *Phys. Rev. Research* **3,** 043163 (2021) (cit. on pp. 37, 54, 77, 94).

93. Raj, G. *et al.* Probing ultrafast magnetic-field generation by current filamentation instability in femtosecond relativistic laser-matter interactions. *Phys. Rev. Research* **2,** 023123 (2 2020) (cit. on pp. 38, 73).

94. Kurz, T. *et al.* Calibration and cross-laboratory implementation of scintillating screens for electron bunch charge determination. *Review of Scientific Instruments* **89,** 093303 (2018) (cit. on pp. 39, 107, 111).

95. Buck, A. *et al.* Absolute Charge Calibration of Scintillating Screens for Relativistic Electron Detection. *Review of Scientific Instruments* **81,** 033301. ISSN: 0034-6748, 1089-7623 (2010) (cit. on pp. 39, 107).

96. Kurz, T. *Calibration of scintillation screens for bunch charge determination in laser wakefield acceleration* MA thesis (Ludwig-Maximilians-Universität München, 2016) (cit. on pp. 39, 108).

97. Ding, H. *LWFA diagnostics development for ATLAS-300 and nonlinear plasma wavelength scalings* PhD thesis (Ludwig-Maximilians-Universität München, 2022) (cit. on p. 40).

98. Pae, K. H., Choi, I. W. & Lee, J. Self-Mode-Transition from Laser Wakefield Accelerator to Plasma Wakefield Accelerator of Laser-Driven Plasma-Based Electron Acceleration. *Physics of Plasmas* **17,** 123104. ISSN: 1070-664X, 1089-7674 (2010) (cit. on p. 44).

99. Masson-Laborde, P. E. *et al.* Giga-Electronvolt Electrons Due to a Transition from Laser Wakefield Acceleration to Plasma Wakefield Acceleration. *Physics of Plasmas* **21,** 123113. ISSN: 1070-664X, 1089-7674 (2014) (cit. on p. 44).

100. Litos, M. *et al.* 9 GeV energy gain in a beam-driven plasma wakefield accelerator. *Plasma Physics and Controlled Fusion* **58,** 034017 (2016) (cit. on p. 54).

101. Pompili, R. *et al.* Energy spread minimization in a beam-driven plasma wakefield accelerator. *Nature Physics,* 1–5. ISSN: 1745-2481 (2021) (cit. on p. 54).

102. Sävert, A. *Few-cycle microscopy of a laser wakefield accelerator* PhD thesis (Friedrich-Schiller-Universität Jena, Jena, 2016) (cit. on p. 56).

103. Panigrahi, P. K. & Muralidhar, K. *Schlieren and Shadowgraph Methods in Heat and Mass Transfer* ISBN: 978-1461445340 (Springer New York, New York, NY, 2012) (cit. on p. 56).

104. Hue, C. S., Wan, Y., Levine, E. Y. & Malka, V. Control of Electron Beam Current, Charge, and Energy Spread Using Density Downramp Injection in Laser Wakefield Accelerators. *Matter and Radiation at Extremes* **8,** 024401. ISSN: 2468-2047, 2468-080X (2023) (cit. on pp. 62, 97).

105. Xu, X. L. *et al.* High quality electron bunch generation using a longitudinal density-tailored plasma-based accelerator in the three-dimensional blowout regime. *Physical Review Accelerators and Beams* **20,** 111303 (2017) (cit. on pp. 62, 89).

106. Weibel, E. S. Spontaneously Growing Transverse Waves in a Plasma Due to an Anisotropic Velocity Distribution. *Physical Review Letters* **2,** 83–84. ISSN: 0031-9007 (1959) (cit. on p. 73).

107. Doss, C. E. *et al.* Laser-Ionized, Beam-Driven, Underdense, Passive Thin Plasma Lens. *Physical Review Accelerators and Beams* **22,** 111001. ISSN: 2469-9888 (2019) (cit. on p. 75).

108. Ke, L. T. *et al.* Near-GeV Electron Beams at a Few Per-Mille Level from a Laser Wakefield Accelerator via Density-Tailored Plasma. *Physical Review Letters* **126,** 214801 (2021) (cit. on pp. 81, 90).

109. Thévenet, M. *et al.* Pulse Front Tilt Steering in Laser Plasma Accelerators. *Physical Review Accelerators and Beams* **22,** 071301. ISSN: 2469-9888 (2019) (cit. on p. 82).

110. Huijts, J. *et al.* Waveform Control of Relativistic Electron Dynamics in Laser-Plasma Acceleration. *Physical Review X* **12,** 011036 (2022) (cit. on p. 82).

111. Zhang, C. *et al.* Effect of fluctuations in the down ramp plasma source profile on the emittance and current profile of the self-injected beam in a plasma wakefield accelerator. *Phys. Rev. Accel. Beams* **22,** 111301 (11 2019) (cit. on p. 82).

112. Ferri, J. & Davoine, X. Enhancement of Betatron x Rays through Asymmetric Laser Wakefield Generated in Transverse Density Gradients. *Physical Review Accelerators and Beams* **21,** 091302. ISSN: 2469-9888 (2018) (cit. on p. 82).

113. Weingartner, R. *et al.* Ultralow emittance electron beams from a laser-wakefield accelerator. *Physical Review Special Topics-Accelerators and Beams* **15,** 111302 (2012) (cit. on pp. 84, 90, 92, 98).

114. Mehrling, T., Grebenyuk, J., Tsung, F. S., Floettmann, K. & Osterhoff, J. Transverse emittance growth in staged laser-wakefield acceleration. *Physical Review Special Topics-Accelerators and Beams* **15,** 111303 (2012) (cit. on pp. 87, 90, 99).

115. Floettmann, K. Adiabatic matching section for plasma accelerated beams. *Phys. Rev. ST Accel. Beams* **17,** 054402 (2014) (cit. on pp. 87, 90).

116. Ariniello, R., Doss, C. E., Hunt-Stone, K., Cary, J. R. & Litos, M. D. Transverse beam dynamics in a plasma density ramp. *Physical Review Accelerators and Beams* **22,** 041304 (2019) (cit. on pp. 87, 90).

117. Lindstrøm, C. A. *et al.* Emittance Preservation in a Plasma-Wakefield Accelerator. *Nature Communications* **15,** 6097. ISSN: 2041-1723 (2024) (cit. on p. 91).

118. Peña, F. *et al.* Energy Depletion and Re-Acceleration of Driver Electrons in a Plasma-Wakefield Accelerator. *Physical Review Research* **6,** 043090 (2024) (cit. on p. 91).

119. Migliorati, M. *et al.* Intrinsic normalized emittance growth in laser-driven electron accelerators. *Physical Review Special Topics-Accelerators and Beams* **16,** 011302 (2013) (cit. on pp. 92, 99).

120. Su, Q. *et al.* Optimization of Transformer Ratio and Beam Loading in a Plasma Wakefield Accelerator with a Structure-Exploiting Algorithm. *Physics of Plasmas* **30,** 053108. ISSN: 1070-664X, 1089-7674 (2023) (cit. on p. 97).

121. Khrennikov, K. *et al.* Tunable All-Optical Quasimonochromatic Thomson X-Ray Source in the Nonlinear Regime. *Physical Review Letters* **114,** 195003 (2015) (cit. on p. 99).

122. Wang, W. *et al.* Free-electron lasing at 27 nanometres based on a laser wakefield accelerator. *Nature* **595,** 516–520 (7868 2021) (cit. on p. 99).

123. Labat, M. *et al.* Seeded Free-Electron Laser Driven by a Compact Laser Plasma Accelerator. *Nature Photonics,* 1–7. ISSN: 1749-4893 (2022) (cit. on p. 99).

124. Lehe, R. *Improvement of the quality of laser-wakefield accelerators* PhD Thesis, Ecole Polytechnique, Laboratoire d'Optique Appliquée. Laboratoire d'Optique Appliquée, 2014 (cit. on p. 99).

125. Couprie, M. E. Panorama of new generation of accelerator based short wavelength coherent light sources. *Nuclear Instruments and Methods in Physics Research Section B: Beam Interactions with Materials and Atoms* **364 IS -,** 4–15 (2015) (cit. on p. 99).

126. André, T. *et al.* Control of laser plasma accelerated electrons for light sources. *Nature Communications* **9,** 1334 (1 2018) (cit. on p. 99).

127. Maier, A. R. *et al.* Demonstration Scheme for a Laser-Plasma-Driven Free-Electron Laser. *Physical Review X* **2,** 031019 (2012) (cit. on p. 99).

128. Lindstrøm, C. A. Staging of plasma-wakefield accelerators. *Physical Review Accelerators and Beams* **24,** 014801 (2021) (cit. on p. 99).

129. Steinke, S. *et al.* Multistage Coupling of Independent Laser-Plasma Accelerators. *Nature* **530,** 190–193. ISSN: 0028-0836, 1476-4687 (2016) (cit. on p. 99).

130. Kirchen, M. *et al.* Stable discrete representation of relativistically drifting plasmas. *Physics of Plasmas* **23,** 100704 (2016) (cit. on p. 100).

131. Wu, Y. C., Zhu, B., Dong, K. G., Yan, Y. H. & Gu, Y. Q. Note: Absolute Calibration of Two DRZ Phosphor Screens Using Ultrashort Electron Bunch. *Review of Scientific Instruments* **83,** 026101. ISSN: 0034-6748, 1089-7623 (2012) (cit. on p. 111).

132. Giakoumakis, G. E. & Miliotis, D. M. Light Angular Distribution of Fluorescent Screens Excited by X-Rays. *Physics in Medicine and Biology* **30,** 21–29. ISSN: 0031-9155, 1361-6560 (1985) (cit. on p. 111).

133. Hüther, M. *Design and Characterisation of Supersonic Nozzles for Shock Front Electron Injection in Laser Wakefield Acceleration* MA thesis (Ludwig-Maximilians-Universität München, 2015) (cit. on p. 119).

Danksagungen

Zu Beginn möchte ich vorwegschicken, dass mein Gedächtnis leider nicht ausreicht, um all den wunderbaren Weggefährten der letzten Jahre den gebührenden Dank auszusprechen. Diese Liste wird daher niemals vollständig sein. Falls du deinen Namen hier also nicht findest oder wichtige Leistungen nicht erwähnt werden, bitte ich um Nachsicht.

Mein besonderer Dank gilt Professor **Stefan Karsch**. Seit nunmehr acht Jahren stehe ich bei dir in verschiedensten Positionen in Lohn und Brot und durfte das Handwerk des Experimentalphysikers erlernen. Vielen Dank für die Betreuung dieser Arbeit und, vielleicht noch wichtiger, für das Zur-Verfügung-Stellen von ATLAS – deinem sehr großen und teuren Spielzeug, das die Ergebnisse dieser Arbeiten ermöglicht hat und an dem ich in den letzten Jahren große Freiheiten genießen durfte.

Ein großes Dankeschön geht auch an die weiteren Mitglieder der für mich zuständigen Promotionskommission, insbesondere an Professor **Ulrich Schramm**, der sich als Zweitgutachter zur Verfügung gestellt hat und mit dem (und seiner ganzen Gruppe) wir seit Jahren super in der Hybrid-Kollaboration zusammenarbeiten.

Allen (teilweise ehemaligen) Kollegen von ETTF, ATLAS und PFS möchte ich herzlich für die Zusammenarbeit und Unterstützung danken:

Besonders danke ich Dr. **Andreas Döpp** für unsere hervorragenden Gespräche über physikalische und unphysikalische Themen und insbesondere für deine wertvolle Orientierungshilfe beim Verfassen unseres gemeinsamen Papers.

Gregor Schilling danke ich ganz besonders für die Gesellschaft in unzähligen Stunden am Laser, dafür dass du mit mir zusammen die Anschaffung der Siebträgermaschine voran getrieben hast und für deine vielen Fahrradtipps, die du mir zukommen lassen hast. Von den inspirierenden Gesprächen mit Gregor motiviert entstand mein Dienstfahrrad, dem ich für die unzählige Transporte zu jeder Tages- und Nachtzeit nach Garching und zurück nach Hause danke.

Ein großer Dank gebührt meinen Kollegen, deren Gesellschaft und Hilfe von unschätzbarem Wert waren: **Florian Haberstroh**, der nicht nur sehr oft bei den nächtlichen Fahrradheimfahrten dabei war, sondern auch mit seiner unermüdlichen Arbeit und seinem Enthusiasmus am Probesetup und weit darüber hinaus einen großen Beitrag auch zu meiner Arbeit geleistet hat. **Katinka von Grafenstein**, die andere hauptamtliche Elektronenbeschleunigerin in ETTF, hat durch ihre Expertise, ihr Engagement und ihr Auge dafür, dass wir immer genug Wasserstoff in der Flasche haben, wesentlich zum Gelingen der LWFA-Experimente beigetragen. Ebenso möchte ich den vielen weiteren Kollegen danken, mit denen ich gerne die Zeit verbracht habe und die beim Betreiben der CALA-Infrastruktur unverzichtbar waren und sind: **Faran Irshad**, **Enes Travac**, **Nils Weiße**, **Andreas Münzer**, Dr. **Mathias Krüger** und Dr. **Jinpu Lin** sowie den externen bzw. temporären Kollegen **David Campbell** und Dr. **Albert Schletter**. Großer Dank gilt auch meinem geschätzten Zimmernachbarn Dr. **Johannes Zirkelbach**, der im letzten Jahr zur Gruppe stieß und für den ich erstmal aufräumen musste, nachdem ich unser Büro während der langen Corona-Jahre habe

verwahrlosen lassen.

Dank gilt auch den ehemaligen Gruppenmitgliedern Dr. **Max Gilljohann**, Dr. **Johannes Götzfried**, Dr. **Hao Ding** und **Sabine Schindler**, die mir während unseres kurzen zeitlichen Überlapps nicht nur wertvolle Tipps für das Leben als Elektronenbeschleuniger gegeben haben, sondern deren Vorarbeiten im Bereich der High-Charge LWFA und Hybrid L-PWFA direkt in diese Arbeit eingeflossen sind.

Ein besonderer Dank gilt auch der **Hybrid-Kollaboration** und allen Kollegen aus Dresden, Paris, Hamburg, Strathclyde und Düsseldorf. Die Zusammenarbeit und der Austausch von Wissen und Ideen innerhalb dieser Gruppe haben maßgeblich zum Erfolg dieses Projekts beigetragen.

Den Kollegen von **LION**, **HF**, u.s.w., besonders **Lenny Doyle**, danke ich für seine unschätzbare Hilfe bei allen Fragen und Problemen zu Tango, Wellenfrontsensoren, der Beamline und vielem mehr. Allen **technischen und administrativen Mitarbeitern von CALA** möchte ich ebenfalls meinen tief empfundenen Dank aussprechen. Ein großer Dank geht auch an die **mechanische Werkstatt Garching**, die viele meiner Aufbauten realisiert hat, obwohl ich oft, ganz Physiker, die Normen und Richtlinien guten Konstruierens sträflich vernachlässigt habe.

Mein Dank gilt auch der **Max Planck School of Photonics** (MPSP) für die finanzielle Förderung und die vielen inspirierenden Frühlings- und Herbstschulen mit interessantem Programm, guten Gesprächen und leckerem Bier. Auch der **Studienstiftung des Deutschen Volkes** möchte ich für ihre Unterstützung danken, ebenso den diversen Geldgebern und Förderprogrammen für Studierende, über die ich eine große Zahl an Konferenzen und Schulungen besuchen konnte.

Ian Butcher, dir danke ich herzlich für das Korrekturlesen meiner Arbeit. Erst durch deine Unterstützung hat mein Englisch, eine Sprache, die mir noch immer nicht allzu nahe steht, ein Niveau erreicht, das die allgemeine Lesbarkeit der Arbeit ermöglicht.

Meiner **Familie** möchte ich meinen tiefsten Dank aussprechen, insbesondere dir, **Hannah**, für alles, und im Zusammenhang dieser Arbeit insbesondere die unendliche Geduld und das Korrekturlesen, und dir, **Enno**, das du mir das Elterngeld organisiert hast, mich hinreichend viel hast schlafen lassen und im Voraus dafür, dass du diese Arbeit in wenigen Jahren begeistert lesen wirst.